Aalto-yliopisto
Aalto-universitetet
Aalto University

Rapport 2025-1
Master´s thesis Deposit thickness
(water side deposits)

Master's Programme in School of Chemical Engineering

Predictive model for wall tube corrosion in kraft recovery boilers: Influence of deposits on the cladding material's performance

Pekka Pirkola

Master's thesis
2025

Aalto-yliopisto
Aalto-universitetet
Aalto University

Author Pekka Pirkola

Title of thesis Predictive model for wall tube corrosion in kraft recovery boilers: Influence of deposits on the cladding material's performance

Programme Chemical, Biochemical and Materials Engineering

Major Sustainable Metals Processing

Thesis supervisor Prof. Daniel Lindberg

Thesis advisor(s) D.Sc. Jari Aromaa and Ph.Lic. Timo Karjunen

Collaborative partner Finnish and Swedish Recovery Boiler Committee

Date 18.07.2025 **Number of pages** 107 **Language** English

Abstract

The kraft recovery boiler (KRB) is a central unit in kraft pulp mills, responsible for generating energy, recovering cooking chemicals, and minimizing environmental emissions. However, the lower furnace operates under extreme conditions, high heat flux, hydrogen sulfide, alkali-rich gases, and molten smelt, which subject water/steam wall tubes to intense corrosion. To mitigate this, composite tubes made of carbon steel with corrosion-resistant claddings such as AISI 304 or Sanicro 38 are commonly used. Nonetheless, internal deposit buildup from poor water quality significantly raises tube temperatures and accelerates corrosion, posing safety and maintenance challenges.

This thesis presents a physics-based calculation model designed to estimate cladding surface temperatures and corrosion rates (CR) as a function of internal deposit thickness, material properties, and boiler operating conditions. The model is geometry-independent and incorporates multilayer heat conduction, temperature-dependent thermal properties, and empirically derived CR functions for both AISI 304 and Sanicro 38 under sulfidation-prone KRB environments.

Results indicate that even thin layers (10–20 μm) of low-conductivity internal deposits can substantially increase cladding temperature and CR, especially under high steam pressure and floor loading. Conversely, magnetite-rich deposits with higher thermal conductivity allow for greater deposit thickness without surpassing critical corrosion limits. Model accuracy is highest within the bottom 20% of the furnace, where sulfidation is most severe and validation data are available.

The model supports mill operators and boiler designers in material selection, risk assessment, and maintenance scheduling. Recommendations for future work include integrating dynamic deposit growth based on water chemistry, refining heat flux distributions across KRBs, and expanding site-specific validation of corrosion behaviour. Overall, the model offers a practical tool for improving predictive maintenance and extending the operational lifespan of KRB components.

Keywords Kraft recovery boiler, corrosion, sulfidation, cladding, AISI 304, Sanicro 38, heat flux, black liquor, calculation model

Aalto-yliopisto
Aalto-universitetet
Aalto University

Tekijä Pekka Pirkola

Työn nimi Ennustava laskentamalli seinäputkien korroosiolle soodakattiloissa: Kerrostumien vaikutukset pinnoitteiden kestävyyteen

Koulutusohjelma Kemian-, biokemian- ja materiaalitekniikka

Pääaine Metallien prosessi- ja kierrätystekniikka

Vastuuopettaja/valvoja Prof. Daniel Lindberg

Työn ohjaaja(t) TkT. Jari Aromaa and Ph.Lic. Timo Karjunen

Yhteistyötaho Suomen ja Ruotsin Soodakattilayhdistys

Päivämäärä 18.07.2025 **Sivumäärä** 107 **Kieli** Englanti

Tiivistelmä

Soodakattila on keskeinen yksikkö nykyaikaisissa sellutehtaissa. Se tuottaa energiaa, palauttaa keittokemikaalit prosessikiertoon ja vähentää ympäristöpäästöjä. Kattilan tulipesän alaosa toimii äärimmäisissä olosuhteissa sillä korkeat lämpövuot, rikkivetypitoisuudet, emäksiset kaasut ja sula aiheuttavat voimakasta korroosiota vesihöyryputkien pinnoilla. Korroosion hillitsemiseksi käytetään komposiittiputkia, joissa on hiiliteräsrunko ja korroosionkestävä pinnoite, kuten AISI 304 tai Sanicro 38. Huonolaatuinen syöttövesi voi kuitenkin muodostaa sisäpuolisia kerrostumia, jotka nostavat putkien pintalämpötilaa ja kiihdyttävät korroosiota, mikä aiheuttaa kunnossapito- ja turvallisuusriskejä.

Tässä työssä kehitettiin laskennallinen, fysiikkaan perustuva malli, jonka avulla voidaan arvioida kattilaputkien pinnoitteen pintalämpötila ja korroosionopeus sisäpuolisten kerrostumien paksuuden, materiaalien ominaisuuksien ja käyttöolosuhteiden perusteella. Malli ei ota kantaa kattilan kokoon, ja siinä on otettu huomioon monikerroksinen lämmönsiirto, lämpötilariippuvaiset materiaaliparametrit sekä AISI 304- ja Sanicro 38 -pinnoitteiden empiirisesti johdetut korroosiofunktiot sulfidipitoisessa ympäristössä.

Tulokset osoittavat, että jopa ohuet (10–20 µm) kerrostumat, joilla on alhainen lämmönjohtavuus, voivat merkittävästi nostaa putkien pintalämpötilaa ja korroosionopeuksia, erityisesti suurilla höyrypaineilla ja pohjakuormituksilla. Sen sijaan magnetiittia sisältävät kerrostumat, joilla on korkeampi lämmönjohtavuus, voivat olla paksumpia ilman, että korroosioraja ylittyy. Mallin tarkkuus on suurin tulipesän alaosassa (noin 0–20 % korkeudesta), jossa sulfidointi on voimakkainta ja validointidata kattavinta.

Laskentamalli tarjoaa käytännön työkalun tehtaan käyttöhenkilöstölle ja kattilasuunnittelijoille materiaalivalintoihin, riskien arviointiin ja kunnossapidon suunnitteluun. Jatkokehityksessä tulisi integroida kerrostumien dynaaminen kasvu veden laadun perusteella, tarkentaa lämpövuon jakautumaa eri kattilatyypeissä sekä laajentaa korroosion empiiristä validointia eri kattiloissa. Malli tukee ennakoivaa kunnossapitoa ja auttaa pidentämään kattilaputkien käyttöikää.

Avainsanat Soodakattila, korroosio, sulfidoituminen, pinnoite, AISI 304, Sanicro 38, lämpövuo, mustalipeä, laskentamalli

Table of contents

Preface

This master's thesis was conducted in collaboration with the Finnish and Swedish Recovery Boiler Committees and Aalto University School of Chemical Engineering, from late 2024 to early summer 2025.

I would like to sincerely thank the Finnish and Swedish Recovery Boiler Committees for offering this fascinating thesis topic and for their invaluable support and materials, which were essential to the success of this research. I also extend my gratitude to the Aalto University School of Chemical Engineering for providing the academic environment, resources, and facilities necessary for both the research and the writing of this thesis.

Special thanks to Metsä Group for hosting me at your mill and sharing practical, firsthand knowledge of kraft recovery boiler operations. I also wish to thank Tampere Valmet Technologies Oy for providing insightful feedback and technical materials that helped strengthen the foundation of this work.

A heartfelt thank you to Ph.Lic. Timo Karjunen for your expert guidance in building the calculation model and for acting as an important link between me, boiler operators, and KRB manufacturers. Your contribution was invaluable. I am also deeply grateful to docent Jari Aromaa and Prof. Daniel Lindberg for their supervision, whose feedback and insight elevated the quality of this thesis to a higher level.

To my mother, father, and sister - thank you for your unwavering support and belief in me throughout this long academic journey. To all my friends, thank you for making this experience memorable and for standing by me during both significant and difficult times.

Finally, my deepest gratitude goes to Anni. Your constant support, encouragement, and presence have been my foundation through the most challenging years. Without you, I would not have completed even my bachelor's degree - thank you for everything.

Otaniemi, July 18, 2025

Pekka Pirkola

Symbols and abbreviations

Symbols

A_f	Floor area
A_{ti}	Tube inside area
CR	Corrosion rate
c_w	Specific heat capacity of water/steam mixture
D_{ti}	Tube inside diameter
D_{to}	Tube outside diameter
g_d	KRB specific deposits growth rate
h	Heat transfer coefficient
HHRR	Floor loading / hearth heat release rate
HHV	Higher heating value
k_{304}	Temperature dependent AISI 304 thermal conductivity
k_{38}	Temperature dependent Sanicro 38 thermal conductivity
k_{cl}	Temperature dependent cladding thermal conductivity for either AISI 304 or Sanicro 38
k_{cs}	Temperature dependent carbon steel thermal conductivity
k_d	Thermal conductivity of internal deposit/magnetite
k_l	Heat flux multiplier
k_s	Thermal conductivity of smelt
k_w	Thermal conductivity of water/steam mixture
l%	Height observed in furnace
l_d	Furnace depth
l_h	Furnace height from primary air port to nose arch upper edge
l_m	Measurement point height from primary air port
l_w	Furnace width
$\dot{m}$DS	DS firing rate
$\dot{m}_l$	Mass flow of saturated 100% liquid water
Nu	Nusselt number
P	Steam drum pressure
Pr	Prandtl number
q	Heat flux
q_a	Average heat flux
q_l	Heat flux in observed location
q_m	Maximum heat flux
Q_{net}	Net heat input
Q_{tot}	Total heat input
Re	Reynolds number
T_{cc}	Temperature of carbon steel-cladding interface
T_{cf}	Temperature of cladding surface facing furnace for either AISI 304 or Sanicro 38

T_{dc}	Temperature of deposit-carbon steel interface
T_s	Smelt melting temperature
T_w	Temperature of water/steam mixture
t_w	Time between chemical acid cleanings
T_{wd}	Temperature of deposit surface facing water
u_l	Steam drum saturated water velocity
u_w	Water/steam mixture velocity inside wall tube
v-%	Water/steam mixture vapor ratio
x_{cl}	Cladding thickness
x_{cs}	Carbon steel thickness
x_d	Average internal deposits thickness
x_s	Smelt max thickness for either AISI 304 or Sanicro 38
x_t	Total wall thickness
μ_w	Dynamic viscosity of water/steam mixture
ρ_l	Density of saturated 100% liquid water
ρ_w	Density of water/steam mixture

Abbreviations

CR	Corrosion rate
DS	Dry solids
EPRS	Effective projected surface area
ESP	Electrostatic precipitators
FAC	Flow assisted corrosion
HHV	Higher heating value
KRB	Kraft recovery boiler
LHV	Lower heating value
NCG	Non-condensable gases
NDT	Non-destructive testing
NO_x	Nitrogen oxides
SCC	Stress corrosion cracking
TRS	Total-reduced-sulfur
VOC	Volatile organic compound

1 Introduction

The kraft recovery boiler (KRB) is the cornerstone of modern kraft pulp mills, because it performs three indispensable duties simultaneously as (i) converting the organic fraction of black liquor into high pressure steam for power and process heat, and (ii) regenerating cooking chemicals, thereby closing the alkali sulfur loop, and (iii) reducing pollution by converting wastes into less harmful forms. Any unplanned outage of the KRB halts liquor circulation, interrupts fiber-line operation, and can impose substantial economic losses on the mill.

Combustion of the dissolved organics in concentrated black liquor releases heat that is transferred through heat transfer surfaces, such as water-cooled wall tubes, to the water/steam circulation and ultimately turbines. The furnace environment is exceptionally aggressive as it contains hydrogen sulfide and alkali-rich flue gases, molten smelt, and high heat fluxes, which results in a complex combination of corrosion, thermal fatigue, and cracking, which might lead to tube failure. Tube failure can lead to water entering the furnace and coming in contact with molten smelt, triggering a smelt-water explosion that can cause extensive equipment damage or even complete boiler loss.

High-risk areas, such as lower furnace walls and floor, are built from compound tubes consisting of a carbon steel layer covered with a corrosion resistant nickel-chrome cladding. Carbon steel provides mechanical strength and efficient heat conduction, whereas the cladding protects the tube against alkali and sulfur attacks. Austenitic stainless steels such as AISI 304 and AISI 304L are widely used corrosion resistant cladding alloys, yet field experience shows corrosion and cracking in KRB environment. Sanicro 38 offers superior corrosion resistance, but its higher cost discourages furnace-wide deployment.

Under normal conditions, clean internal surfaces ensure high heat flux and maintain tube metal temperatures within safe limits. Poor water quality causes deposit layers to form inside boiler tubes, especially in heat transfer surfaces such as wall tubes. Because these internal deposits possess significantly lower thermal conductivity than that of the underlying composite tube, they act as insulating barriers, raising tube metal temperatures, and significantly accelerate tube corrosion. Even deposit thicknesses of 10-20 μm can elevate cladding temperature enough to double the corrosion rate (CR) in critical zones.

Non-destructive testing (NDT) and tube sampling is used to detect both tube layers and internal deposits thickness changes, but information gained through current NDT and tube sampling is limited. Internal deposits can be

measured ultrasonically across the range of 0–300 µm with an accuracy of ±25 µm. This is sufficient in typical KRBs, since internal deposit thicknesses that affect cladding performance are usually around 100–150 µm. In very high-pressure units, tolerance for internal deposits is significantly lower around tens of µm, which limits NDT reliability. Tube sampling has its limit as the number of tube samples is usually small and taken from non-critical locations.

Internal deposits are removed with chemical acid cleaning based on NDT and tube sampling data, or more conservatively standardized cleaning cycles regardless of boiler tube conditions. Cleaning based on test data is unreliable as it is usually highly inaccurate. Time standardized cleaning cycles are problematic as thick internal deposits might be formed locally between cycles, causing internal and external corrosion, or on the other hand, lead to unnecessary expenses and mill outages when unnecessary acid cleanings are deployed.

This thesis undertaken in collaboration with the Finnish and Swedish Kraft Recovery Boiler Committees and Aalto University School of Chemical Engineering develops a generalized calculation model that links together internal deposits thickness, cladding surface temperature and cladding corrosion rates (CR) for both austenitic stainless steel AISI 304 and Sanicro 38 to predict internal deposits relation to CR of cladding materials. The model is formulated so that it can be applied to modern kraft recovery boilers regardless of furnace geometry, heat input, or operating pressure, thereby providing mill engineers a predictive tool for material selection, inspection planning, and internal deposit control strategy.

This thesis consists of seven chapters. Chapter 2 focuses on fundamentals of kraft recovery boiler operation and sulfur and sodium circulation. Chapter 3 is a literature overview which explains furnace structure, black liquor combustion and smelt formation mechanisms, air systems and reaction zones, heat distribution and local heat flux, water/steam circulation, tube structure and properties and corrosion types, deposits formation and cleaning. Chapter 4 explains the mechanics and arguments behind the calculation model. Chapter 5 presents the calculation model results, discussion and sensitivity analysis. Chapter 6 is the conclusions and Chapter 7 is a summary of the thesis. Appendix 1 contains chemical formulas and names of the relevant chemical compounds.

2 Fundamentals of kraft recovery boiler

The kraft-recovery boiler (KRB) fulfils three linked objectives as it generates the steam that drives mill power and process heating, it closes the sodium-sulfur chemical loop that is the basis of kraft pulping, and limits pollution by internal recycling (Vakkilainen, 2005). Figure 1 shows overview of kraft pulp mill and KRB location within unit processes.

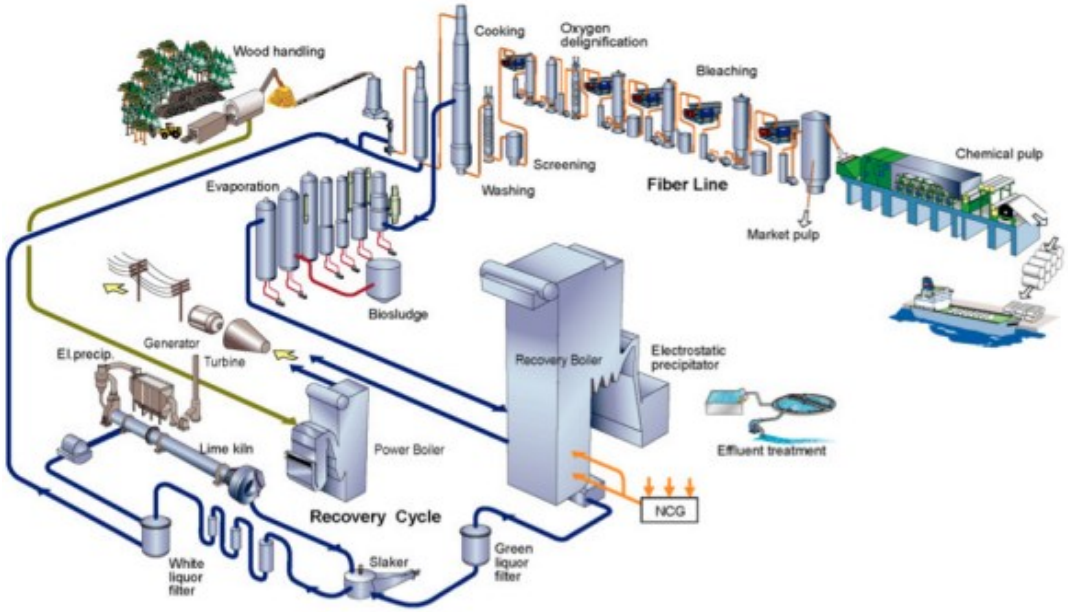

Figure 1. Overview of a conventional kraft pulp mill (Pettersson et al., 2012).

The boiler converts the Energy of concentrated black liquor into high-pressure, high-temperature steam (Vakkilainen, 2005). Energy from combustion is transferred to a water-steam mixture through heat transfer surfaces like those of the economizer, wall tubes, boiler bank and superheaters. Superheated steam is expanded through back-pressure steam turbines to supply electricity and to satisfy the heating requirements in the pulping process, such as in the digestion, evaporation, and drying stages (Pettersson et al., 2012).

Simultaneously, the KRB completes the liquor-recovery circle. In the furnace, sprayed black liquor droplets combust and the remaining organic carbon and inorganic sodium sulfide (Na_2S), sodium sulfate (Na_2SO_4) and sodium carbonate (Na_2CO_3) lands top of a char bed. During combustion, Na_2S might oxidize to Na_2SO_4 (Equation 1). (Hupa and Frederick, n.d.)

$$Na_2S + 2O_2 \rightarrow Na_2SO_4 \quad (1)$$

In the char bed, carbon reduces Na_2SO_4 to Na_2S (Equations 2 and 3), producing a molten smelt of Na_2CO_3 and Na_2S. Figure 2 shows kraft mill unit operations. (Vakkilainen, 2005)

$$Na_2SO_4 + 2C \rightarrow Na_2S + 2CO_2 \quad (2)$$

$$Na_2SO_4 + 4C \rightarrow Na_2S + 4CO \quad (3)$$

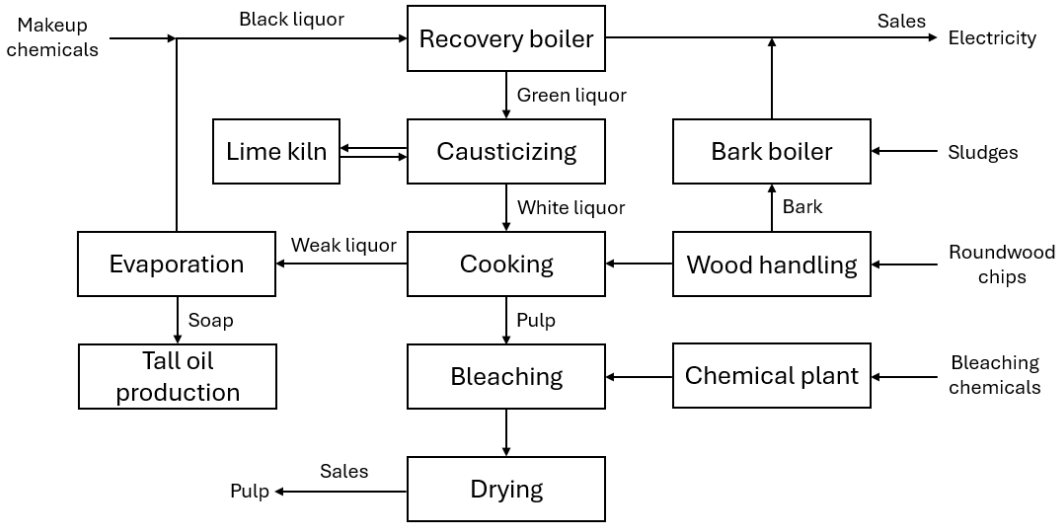

Figure 2. Kraft mill unit operations (adapted from Vakkilainen, 2005).

The smelt flows through water-cooled spouts to the dissolving tank, where it is mixed with water and sometimes weak white liquor to form green liquor. Green liquor is sent to the causticizing plant, where slaked lime ($Ca(OH)_2$) converts Na_2CO_3 into sodium hydroxide (NaOH) (Equation 4), forming white liquor for the next cooking cycle. (Vakkilainen, 2005)

$$Na_2CO_3 + Ca(OH)_2 \rightarrow 2NaOH + CaCO_3 \quad (4)$$

Remaining lime mud ($CaCO_3$) is reburned in the lime kiln to regenerate quicklime (CaO) (Equation 5), and is mixed with water (Equation 6), to form $Ca(OH)_2$ closing the lime loop. (Vakkilainen, 2005)

$$CaCO_3 \rightarrow CaO + CO_2 \quad (5)$$

$$CaO + H_2O \rightarrow Ca(OH)_2 \quad (6)$$

White liquor (Na_2S + NaOH) is used in cooking to remove lignin from wood chips. Pulp and weak black liquor are separated through washing, and the weak black liquor contains inorganics such as Na_2S, NaOH, Na_2CO_3 and

Na_2SO_4 and organics such as lignin, hemicellulose and fatty, resinous and aliphatic acids. (Pettersson et al., 2012)

Precursors such as fatty and resinous acids are extracted from weak black liquor to produce tall oil (Pettersson et al., 2012). Weak black liquor is evaporated from 15% dry solids (DS) (Cardoso et al., 2009) to 65-85% DS (Vakkilainen, 2005) using multistage evaporators, forming black liquor. Makeup chemicals are added to compensate chemical losses and maintain chemical balance (Vakkilainen, 2005). Black liquor is sprayed into the KRB furnace, closing the sodium and sulfur loop. Figure 3 shows sodium and sulfur loop.

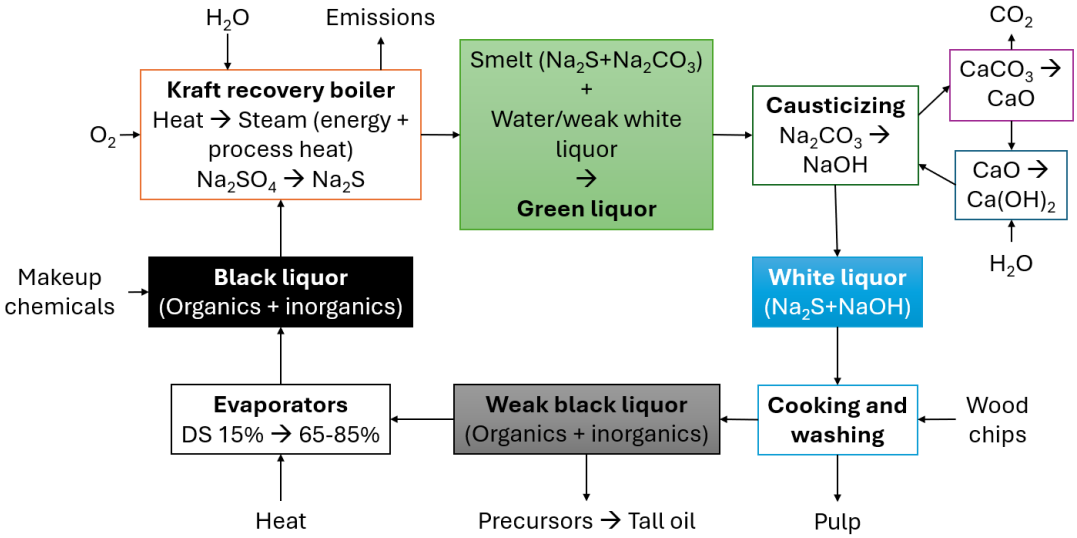

Figure 3. Sodium and sulfur loop.

Pollution control is enforced in several recovery-loop steps. Electrostatic precipitators (ESP) can capture more than 99% of alkali fumes that consist of sodium, sulfur, potassium, chlorine, and carbon (Lind et al., 2006). Sodium and sulfur are returned to the recovery loop, and harmful potassium and chlorine are removed from the loop, purifying the content of black liquor (Vakkilainen, 2005). Some wood types, especially hardwood, produce harmful nitrous oxides (NO_x) during combustion. They are controlled by optimizing air feed and reactions and occasionally feeding ammonia (NH_3) to the top of furnace (Equation 7) (Vakkilainen, 2005).

$$2NH_3 + 2NO + \frac{1}{2}O_2 \rightarrow N_2 + 3H_2O \quad (7)$$

Highly odorous non-condensable gases (NCG) rich in total-reduced-sulfur (TRS) compounds are collected from digesters, evaporators, and liquid storage tanks and burned either in the KRB furnace or the lime kiln to reduce harmful emissions and produce energy (Lin and Eng, 2007). TRS compounds

will oxidize in a modern KRB furnace to sulfur dioxide (SO_2) (Vakkilainen, 2005). Buildup of non-process elements such as dregs are prevented by removing them from green liquor during causticizing (Vakkilainen, 2005). During evaporation volatile materials such as sulfur compounds and methanol (CH_3OH) are separated and disposed of in an environmentally sound way (Clay, 2008).

There are benefits to extracting tall oil from weak black liquor. It can be used as fuel or further processed into other products (Pettersson et al., 2012). Soap in black liquor causes fouling of the evaporators (Puustinen, 2015). Soap causes foaming in evaporators and unstable combustion in the furnace (Suhr et al., 2015). Soap in black liquor takes space from the wanted organic and inorganic parts, wasting energy.

The KRB integrates thermal, chemical, and environmental processes into a single unit. It is a highly optimized and multifunctional system that plays a critical role in the sustainability and self-sufficiency of modern pulp mills.

3 Furnace configuration and process streams

The central unit in a KRB is the furnace, where black liquor is combusted and reduced under tightly controlled thermal and chemical conditions. The furnace integrates several critical subsystems: combustion air distribution, chemical reaction zones, smelt recovery and handling, wall and floor heat exchange structures and water/steam circulation. Each of these are linked and optimized to maximize heat transfer, efficient chemical recovery, and minimal emissions. Figure 4 shows schematic figure of an average KRB.

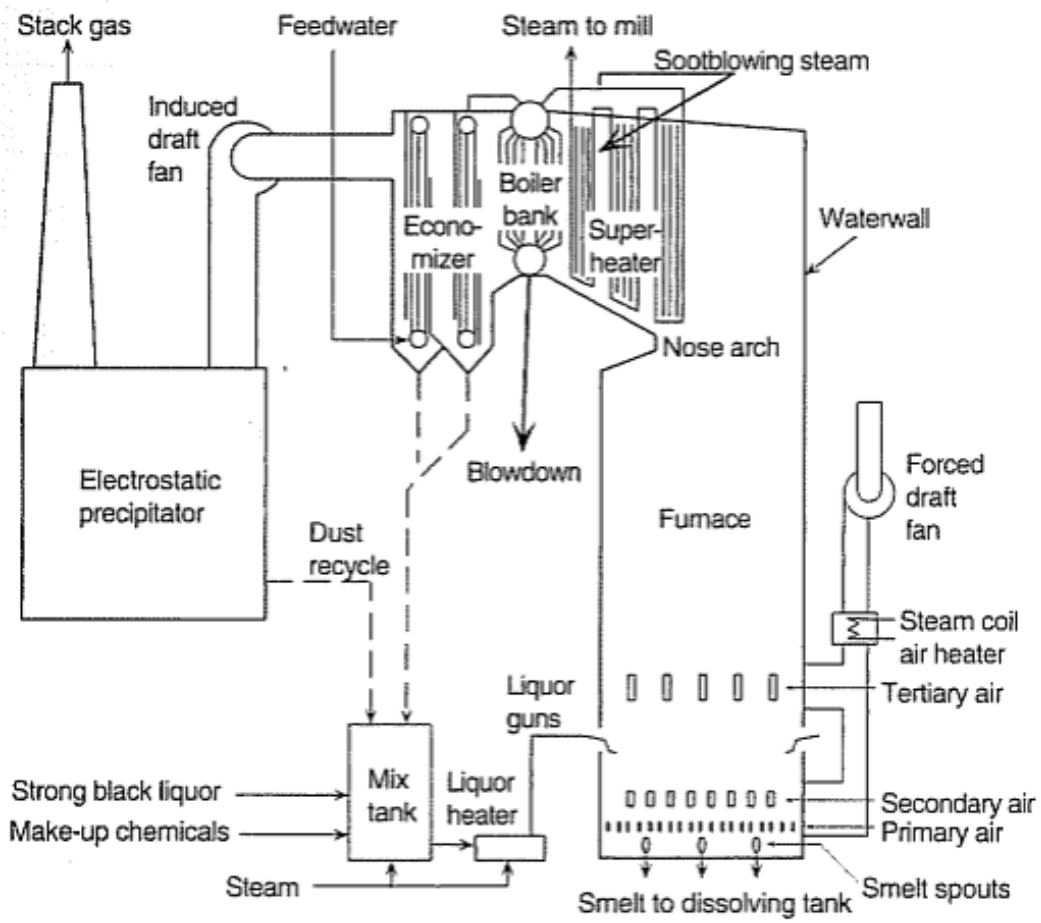

Figure 4. Schematic figure of a KRB (Lundborg, 2005).

In simplified terms, the KRB consists of a furnace zone where the organic fraction of black liquor is burned to release energy, while the inorganic fraction settles to the bottom and contributes to smelt formation. Combustion air, injected at multiple heights through air ports, controls the environment within the furnace, affecting drying, devolatilization, burning and reduction. Membrane wall tubes line the furnace envelope to confine gases and serve as evaporative heat transfer surface. The water circulating inside these tubes

gradually converts to steam, forming the thermal energy basis of the kraft mill. (Vakkilainen, 2005)

This chapter describes the configuration and functional role of each major subsystem involved in furnace operation and material flow. Section 3.1 introduces the properties of black liquor, how it is atomized into droplets, and the four distinct stages of droplet combustion and smelt formation. Section 3.2 focuses on the combustion air systems and how staged air injection establishes wanted reaction zones and reactions. Section 3.3 describes heat production and distribution within the furnace. Section 3.4 presents an overview of the water circulation system. Section 3.5 presents furnace and tube structures and properties of carbon steel and claddings such as austenitic stainless steel AISI 304 and Sanicro 38. Section 3.6 focuses on boiler corrosion types, fouling and deposits properties, formation and removal.

3.1 Black liquor, combustion and smelt

Black liquor can be divided into three fractions which are (i) the organic portion that combusts and forms the char, (ii) the reactive inorganic portion that reacts with char bed to form smelt and (iii) the inactive inorganic portion that passes through combustion system unchanged (Vakkilainen, 2005). Black liquor is typically about two-thirds organic material and one-third inorganic material (Clay, 2008). Table 1 shows average organic and inorganic material weight percentages in black liquor.

Table 1. Average organic and inorganic material weight percentages in black liquor.

	Type	Amount (w-%)	
Organic material	Hydroxy acid	29-45	25-35
	Alkali lignin	25-35	30-45
	Extractives	~5	3-5
	Acetic acid	3-5	5
	Formic acid	~3	3
	Methanol	~1	1
Inorganic material	Sulfur	~6-34	3-5
	Sodium		15-20
Reference		(Bajpai, 2017)	(International, n.d.)

Controlling the DS content in black liquor is important in order to achieve stable and effective combustion and reduction. High DS content improves energy economy and environmental outcomes by lowering SO_2 and hydrogen

sulfide (H_2S) emissions, smoothing combustion, and reducing carryover in the furnace, but also causes plugging, which restricts using high DS of 80-90% (Llamas et al., 2007). Steam generation increases with higher DS content. An increase from 65% to 80%, causes the main steam flow to increase around 7%, as the steam generation increase more than 2% per each 5% of DS content increase (Vakkilainen, 2005). Increasing water volume of black liquor reduces its energy release, as water evaporation during combustion consumes energy. If black liquor DS content is below 20%, the lower heating value (LHV) of black liquor is negative, which means that all heat from combustion is spent on evaporating the water it contains (Vakkilainen, 2005).

Higher heating value (HHV) is the total amount of heat released when fuel combusts. LHV does not include the heat spent in transforming the water into steam and it assumes that the produced water remains as a vapor and the heat of the vapor is not recovered. (Gillenwater et al., 2005)

The difference between a fuel's HHV and its LHV is how each treats the water generated during combustion. HHV is determined by cooling the combustion products back to the reference temperature and condensing the steam to liquid, so it includes the latent heat released during that condensation. LHV, on the other hand, assumes the water remains as vapor so the latent heat needed to keep it in the gaseous phase is therefore excluded, resulting in a smaller net energy value. (Khaleel et al., 2022) Table 2 shows typical HHV and LHV values in different DS percentages.

Table 2. Typical HHV and LHV in different DS values.

DS	HHV	LHV	Reference
	(MJ/kgDS)		
80%	14.50	12.29	(IEA, 2007)
70%	13.95	12.09	(Adams, 1997)
80%	13.00		(Vakkilainen, 2000 from Vakkilainen, 2005)
72%	13.90		
64%	15.00		

HHV depends on black liquor properties such as wood type, lignin concentration and sulfidity. Typical HHV values of black liquor are around 13-15 (MJ/kgDS). Increase in HHV causes higher air demand for combustion. (Vakkilainen, 2005)

Black liquor consists of carbon, hydrogen, nitrogen, sulfur, oxygen, sodium, potassium and chlorine. The composition of the black liquor depends on the wood species, cooking method and the pulping process (Vakkilainen, 2005).

Typical wood species used in pulp production is hardwood and softwood. Hardwood species are for example aspen and birch, and softwood species are pines and spruces (IEA, 2007). Black liquors containing hardwood and softwood have different chemical and physical properties (Table 3).

Table 3. Element weight percentages of black liquors.

Wood specie	C	O	H	Na	S	K	Cl	N	Si	Reference
	35.00	35.70	3.30	19.70	4.00	1.60	0.07			(Clay, 2008)
	35.00	35.70	3.30	19.70	4.00	1.60	0.60	0.10		(Adams, 1997)
	35.70	35.80	3.70	19.00	4.40	1.10	0.30	<0.10	0.00	(IEA, 2007)
	36.40	35.40	3.75	18.00	5.40	0.75	0.20	0.10	0.00	(Vakkilainen, 2000 from Vakkilainen, 2005)
	34.00	36.70	3.50	18.40	5.90	1.00	0.40	0.10	0.00	
	31.60	36.50	3.40	19.80	6.00	1.80	0.80	0.10	0.00	
Hard-wood	30.80	33.69	3.60	21.80	3.70	1.80	4.50	0.01	0.10	(Cardoso et al., 2009)
	35.20	30.50	3.70	21.20	3.00	2.10	4.30	0.00	0.00	
	29.60	38.90	3.60	18.70	4.40	2.20	2.60	0.00	0.00	
	34.80	34.56	3.40	18.30	3.60	2.10	3.20	0.04	0.00	
	33.20	34.52	3.30	20.80	5.20	2.60	0.30	0.08	0.00	
	37.30	34.91	3.60	17.30	3.40	1.80	1.60	0.09	0.00	
Soft-wood	33.9-35.8	31.03-38.94	3.3-3.6	17.2-19.8	4.6-5.7	1.4-2.2	0.3-0.9	0.06-0.07	0.3-0.9	
	34-39	33-38	3-5	17-25	3-7	0.1-2	0.2-2	0.05-0.2	0	(Bajpai, 2017)

Hardwood usually has lower HHV compared to softwood as hardwood has lower lignin weight percentage. Black liquor made of softwood swells more than hardwood, which results in a faster combustion process as there is more surface area for reactions. Hardwood based black liquor droplet size is larger than softwood due to the higher viscosity of hardwoods. Firing pressure needs to be lowered, or temperature of softwood black liquor needs to be lowered 5-7 ^{o}C to achieve same droplet size as hardwood. Because softwood liquor swells more but atomizes into finer droplets, each particle experiences greater aerodynamic drag and loses momentum sooner, so the spray does not launch as far within the furnace. At higher firing temperatures, significantly more of the coarser hardwood liquor droplets travel farther than intended and end up the furnace walls compared to softwood. Hardwood black liquors usually contain more nitrogen, so they produce more NO_x. (Vakkilainen, 2005)

It is important to keep black liquor viscosity low to achieve better fluid movement and sufficient atomization. Viscosity of black liquor can be lowered by increasing water volume or increasing its temperature (Vakkilainen, 2005).

Additives can also be added to reduce black liquor viscosity (Llamas et al., 2007). Balance of high DS and low viscosity needs to be carefully controlled as lower DS reduces heat energy produced, but lowers viscosity, allowing accelerated black liquor flow to liquor gun (Vakkilainen, 2005). Higher DS increases heat energy produced, but lower viscosity causes risks of tube plugging, and therefore requires external heating to maintain operatable black liquor viscosity, which on the other hand requires energy. Figure 5 shows structure of KRB furnace lower levels.

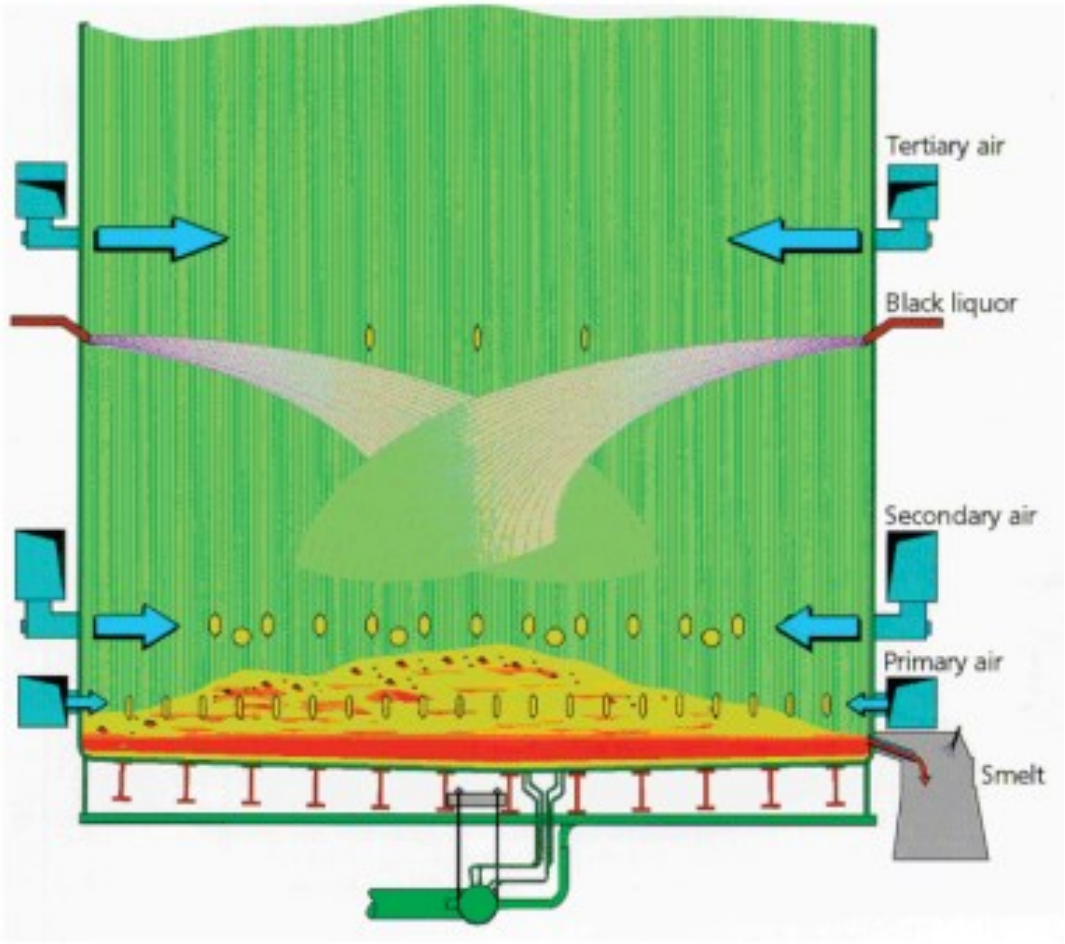

Figure 5. KRB furnace lower part (Vakkilainen, 2005).

The aim of black liquor firing is maintaining a stable and secure operation while having a reasonably low fouling rate and emissions release. Black liquor is sprayed into the furnace through several liquor guns, and black liquor spraying is controlled with pressure, viscosity, and nozzle type. Temperature increase reduces the droplet size. Black liquor is not finely atomized but sprayed as coarse droplets, as the average droplet diameter is 2-3 mm. The target is to avoid complete combustion until the droplet lands to the char bed, so that the inorganic part won't oxidize to form harmful gases such as SO_2

(Equation 8), and to maintain supply of carbon to the reducing char bed. (Vakkilainen, 2005) Figure 6 shows nozzle structure of the black liquor gun.

$$2H_2S + 3O_2 \rightarrow 2SO_2 + 2H_2O \quad (8)$$

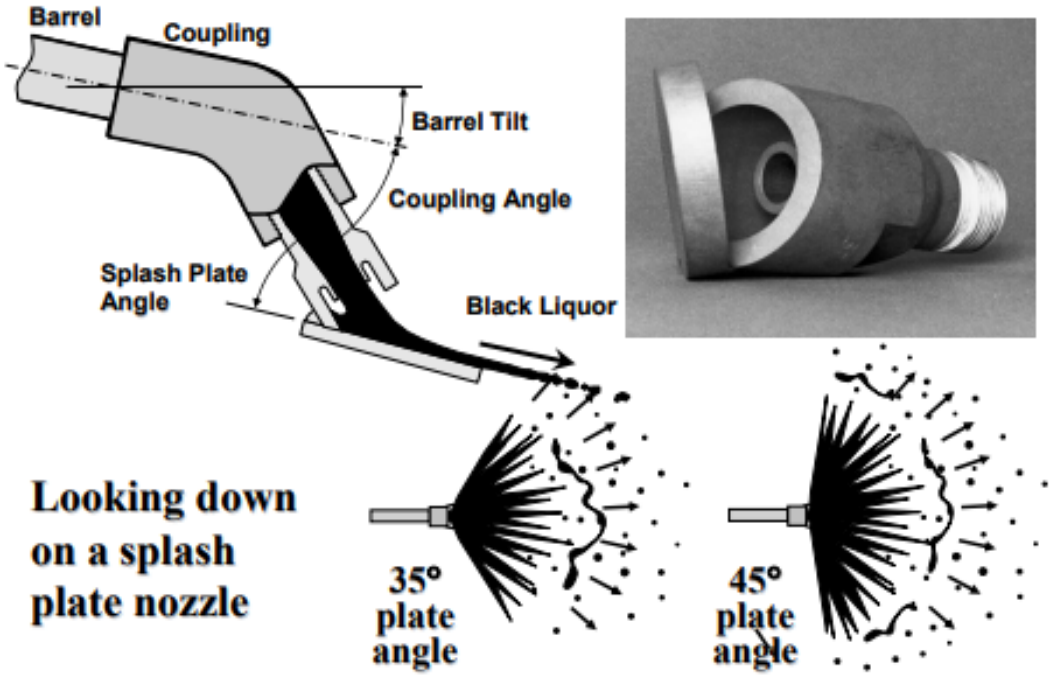

Figure 6. Black liquor gun nozzle structure (Wessel, 2008).

Combustion of black liquor consists of four stages called drying, devolatilization, char burning, and reduction (Figure 7). In the drying stage, water evaporates from black liquor droplets, which consumes energy. The drying stage starts immediately upon furnace entry and takes 1-2 seconds. During this time, the droplet temperature rises rapidly to 150 °C and then slowly to 300 °C as water is evaporated from the droplet. Droplet swells typically by a factor of 1.5 in diameter. At the end of drying, the droplet appears extremely viscous, plastic, or as a solid particle. (Hupa and Frederick, n.d.)

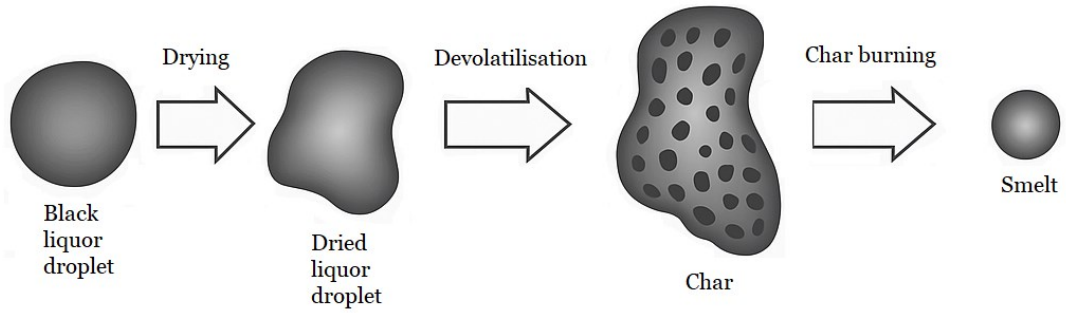

Figure 7. Black liquor combustion phases (adapted from Vakkilainen, 2005).

Devolatilization involves pyrolysis of the liquor's organic matter and release and burning of volatiles (Hupa and Frederick, n.d.). As temperature rises, reactions with the lowest activation energies start taking place, such as release of methane (CH_4), carbon dioxide (CO_2), hydrogen (H_2), and hydrogen sulfide (H_2S) (Vakkilainen, 2005). Devolatilization typically lasts 0.5-2 seconds, and during that phase, temperature rises rapidly to 800 °C (Hupa and Frederick, n.d.). During devolatilization, the droplet swells three times its initial diameter (Hupa and Frederick, n.d.). In order for swelling to happen, the droplet must have a plastic surface, and gas needs to be generated inside the droplet (Vakkilainen, 2005). Smaller droplet size and lower temperature environment cause the droplet to dry completely before devolatilization begins (Frederick and Hupa, 1993).

After volatiles have escaped, the porous droplet particle consists mostly of carbon and sodium salts. During char burning, its surface carbon reacts with oxygen and its size shrinks significantly as carbon is burned away. Char burning duration varies depending mainly on swelling and carbon content of the droplet and during that stage, droplet temperature rises to 1200 °C, which is 400 °C higher than the surrounding temperature. (Hupa and Frederick, n.d.)

Required oxygen for char combustion can come from oxygen (O_2) (Equation 9), elemental oxygen (Equation 10), Na_2SO_4 (Equations 2 and 3 from Chapter 2), water vapor (H_2O) (Equation 11) or CO_2 (Equation 12). Produced carbon monoxide (CO) combusts using O_2 (Equation 13) or H_2O (Equation 14). Produced H_2 combusts using O_2 (Equation 15). (Vakkilainen, 2005)

$$-C_{(s)} + O_2 \rightarrow CO_2 \tag{9}$$

$$-C_{(s)} + \frac{1}{2}O_2 \rightarrow CO \tag{10}$$

$$-C_{(s)} + H_2O \rightarrow CO + H_2 \tag{11}$$

$$-C_{(s)} + CO_2 \rightarrow 2CO \tag{12}$$

$$2CO + O_2 \rightarrow 2CO_2 \tag{13}$$

$$CO + H_2O \rightarrow CO_2 + H_2 \tag{14}$$

$$H_2 + \frac{1}{2}O_2 \rightarrow H_2O \tag{15}$$

In practice, char combustion and devolatilization overlap considerably (Vakkilainen, 2005). At the end of the char burning carbon is depleted and

particle collapses into a molten droplet, losing half of its original diameter (Hupa and Frederick, n.d.). The released inorganic part consists mostly of Na_2SO_4 and Na_2CO_3 as it comes in contact with the char bed. Na_2SO_4 reacts with carbon forming Na_2S (Equations 2 and 3 from Chapter 2) when reducing conditions, such as the required heat energy and an oxygen free atmosphere are met (Vakkilainen, 2005). If droplet burning stage ends before it reaches the char bed, or if there is too much oxygen present, Na_2S is oxidized to Na_2SO_4 (Equation 1 from Chapter 2), causing rise of droplet temperature, as the reaction is exothermic (Hupa and Frederick, n.d.). To prevent oxidation, char formation needs to be maintained through controlled combustion (Vakkilainen, 2005). Reduction efficiency increases as the char bed temperature increases and it is not uncommon to have reduction rates of 95-98% in well operating recovery boilers (Vakkilainen, 2005). Figure 8 shows diameter and temperature changes during combustion and Table 4 shows typical smelt composition depending on wood specie.

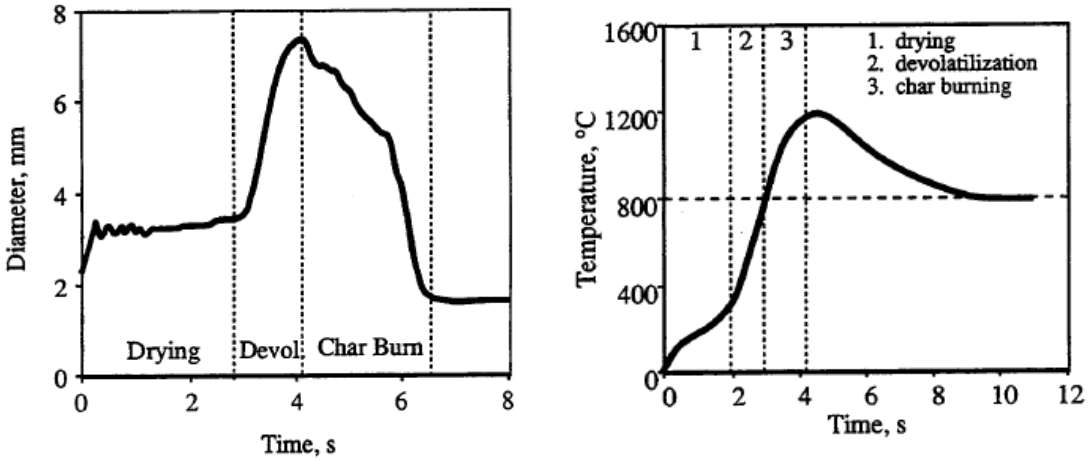

Figure 8. Diameter and temperature changes during combustion in 800 °C (Hupa and Frederick, n.d.).

Table 4. Smelt composition (adapted from Vakkilainen, 2005).

Content	Softwood	Hardwood
	(%)	
Na_2S	25-28	19-21
Na_2CO_3	66-68	72-75
Na_2SO_4	0.4-1.0	0.6-1.4
$Na_2S_2O_3$	0.3-0.4	0.2-0.4
Other	5-6	3-5

Formed smelt consists mostly of Na_2CO_3 and Na_2S and a small amount of unreacted Na_2SO_4 and inactive salts containing potassium and chlorine such as potassium carbonate (K_2CO_3), potassium sulfide (K_2S), potassium sulfate (K_2SO_4), potassium hydroxide (KOH), potassium chloride (KCl) and sodium chloride (NaCl) (Vakkilainen, 2005). The smelt temperature is around 800-1000 ^oC (Metso, 2019). Molten smelt is channelled through the smelt spouts into a dissolving tank where it is dissolved with water or weak white liquor to create green liquor and transported to the causticizing plant. Inactive inorganic portion consisting of potassium and chloride salts is removed from the loop to avoid their accumulation in the system, improve black liquor quality and combustion and increase furnace temperature (Hamaguchi and Vakkilainen, 2011).

3.2 Air systems, reaction zones and fumes

The main requirement for combustion air system is maximum mixing and proper air distribution. The combustion air system delivers oxygen to the KRB furnace in a carefully staged way that it (i) supplies oxygen for drying, devolatilization and char burning, (ii) creates a low-oxygen, high-carbon reducing zone in the char bed, so Na_2SO_4 is reduced to Na_2S (Equations 2 and 3 from Chapter 2), (iii) oxidizes CO, H_2, TRS and other combustibles in the upper furnace and (iv) control furnace temperature and mixing, minimising carryover and fouling. (Vakkilainen, 2005)

Combustion air system (Figure 9) normally consists of intake ventilation that gathers the lost heat from the top of the KRB building, inlet duct and silencer to provide stable inlet flow, venturi to measure air flow, air blower to provide air velocity, air heater to increase air temperature, distribution ducts to split heated air to air ducts and dampers to trim pressure and air flow. (Vakkilainen, 2005)

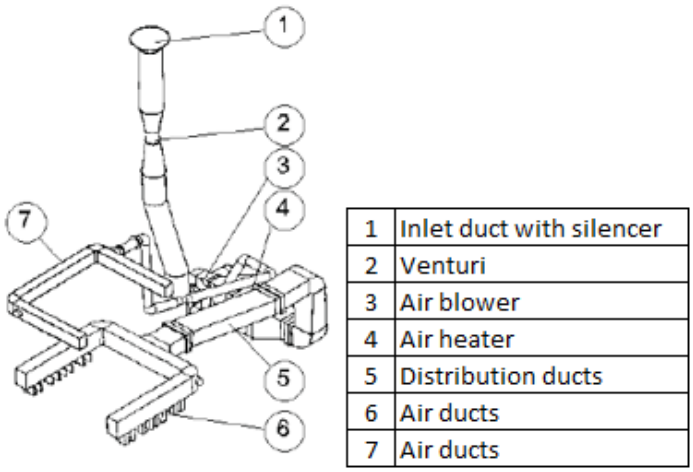

1	Inlet duct with silencer
2	Venturi
3	Air blower
4	Air heater
5	Distribution ducts
6	Air ducts
7	Air ducts

Figure 9. Combustion air system (Vakkilainen, 2005).

Air is channelled into the furnace from multiple different levels called primary, bottom secondary, top secondary, tertiary and in some cases the quaternary air ports. Primary air ports have a lesser effect on furnace combustion than other air ports, but they increase burning at the edges of the char bed and keep char bed away from the walls. Secondary air ports are usually at two different levels. The idea of secondary air ports arrangement is to get as high of a coverage of the horizontal cross-sectional area as possible. Secondary air ports maintain a specified temperature in the lower furnace to reduce emissions, increase reduction and maintain char bed optimal shape. Secondary air burns flowing gases rising from the char bed and radiates its heat back to the char bed. Secondary air ports also reduce plugging of upper section heat surfaces. Tertiary air ports burns the remaining combustibles rising from the lower furnace section reducing emissions. Quaternary air ports are located at the higher part of the furnace and they can reduce NO_x emissions. (Vakkilainen, 2005; Vakkilainen, 1996) Figure 10 shows furnace structure of the large KRB.

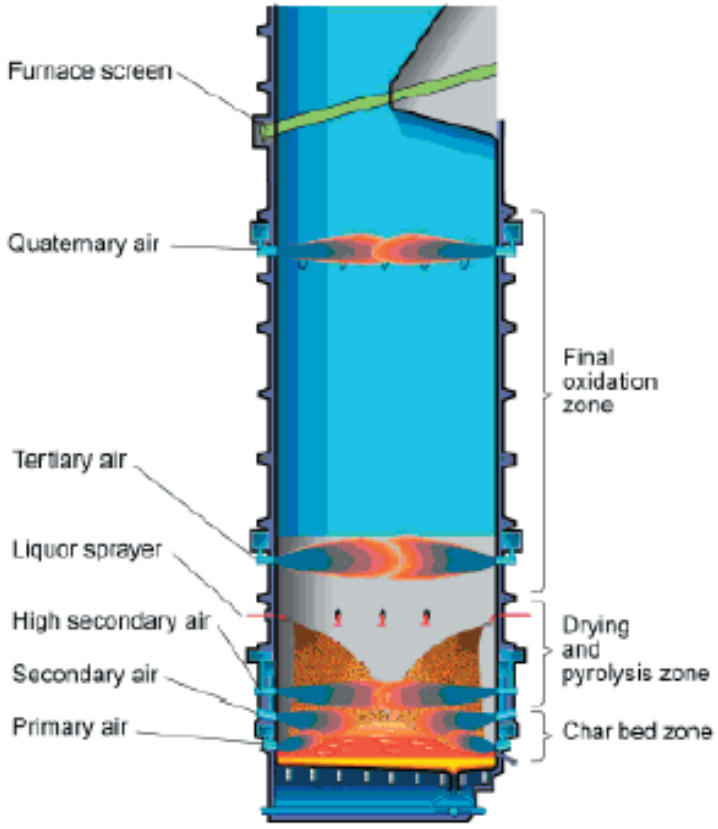

Figure 10. Large KRB furnace (Mäntyniemi and Haaga, 2001 from Vakkilainen, 2005).

Primary air ports are located approximately 1 meter from the furnace floor, secondary air ports are located approximately 1-4 meters from the furnace

floor and tertiary air ports are located approximately 4-14 meters from the furnace floor.

Air ports create three reaction zones called reducing zone, drying/devolatilization zone, and oxidizing zone (Figure 11). Reducing zone is below secondary air port, drying/devolatilization zone is between secondary air port, and black liquor guns. Oxidizing zone ranges from the black liquor guns to the upper furnace. (Vakkilainen, 2005)

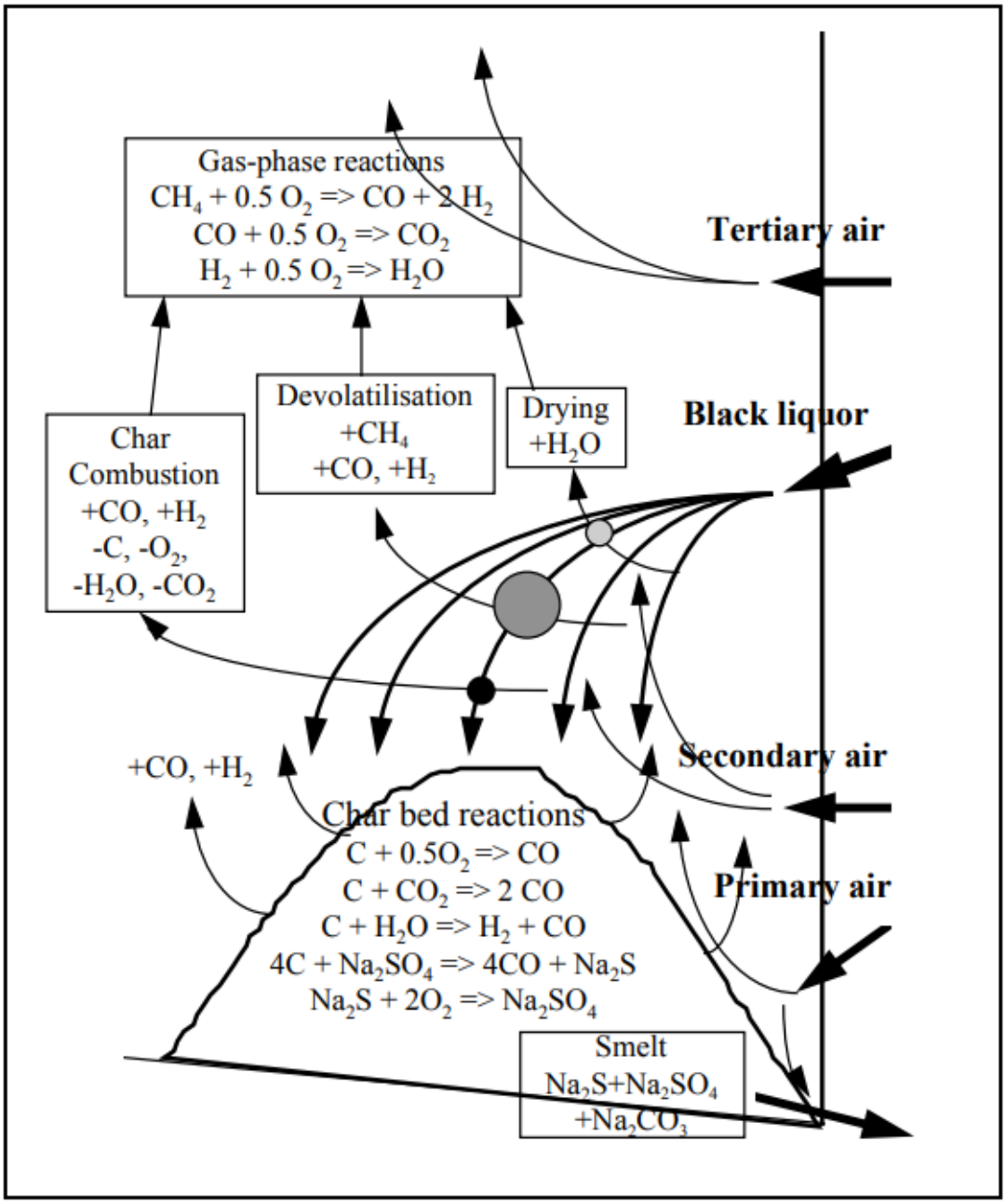

Figure 11. Black liquor combustion processes (Fakhrai, 2002).

Multiple different reactions occur in a KRB furnace. Some of these reactions are used for heat production and maintain a liquor reduction loop but some of them are harmful, as they cause losses of wanted chemicals such as sodium and sulfur, fouling, corrosion and emissions. The target for the reducing zone, is char bed reduction reactions (Equations 2 and 3 from Chapter 2) and heat producing combustion reactions (Equations 9-15). Combustion reactions (Equations 9-15) are also wanted in the drying/devolatilization zone as they produce heat. In oxidizing zone, reactions (Equations 13-15) are wanted, as they remove harmful emissions and produce heat. (Vakkilainen, 2005)

Reactions (1) and (8) occur when combustion ends before droplet lands on char bed. The droplet might get entrained in flue gases and get carried to the upper furnace where its contents oxidize, forming carryover dust containing Na_2SO_4 and Na_2CO_3 causing fouling and deposits. A completely combusted droplet is lighter and at higher risk of getting entrained in flue gases. (Vakkilainen, 2005)

H_2S is formed rapidly through decomposition reactions after gases are released from the droplet. Na_2S reaction with CO_2 and H_2O (Equation 16) converts the wanted Na_2S into an unwanted form Na_2CO_3 and increases TRS emissions and sulfidation. H_2S is considered the main pathway to the formation of sulfur emissions that must later be oxidised into SO_2 in the upper furnace (Equation 17). H_2S contents close to the wall in the lower furnace can be around twenty mole percent. Sulfidation caused by H_2S is the most common form of corrosion in the lower furnace. (Vakkilainen, 2005)

$$Na_2S + CO_2 + H_2O \rightarrow Na_2CO_3 + H_2S \quad (16)$$

$$2H_2S + 3O_2 \rightarrow 2SO_2 + 2H_2O \quad (17)$$

Na_2CO_3 can react with gases forming corrosive products (Equations 18 and 19). Na_2CO_3 can decompose (Equation 20), but as there is an abundance of H_2O present, it is highly likely that NaOH is formed (Equation 21). Na_2CO_3 can react with carbon, releasing volatile sodium (Equation 22). (Vakkilainen, 2005)

$$Na_2CO_3 + SO_2 + \frac{1}{2}O_2 \rightarrow Na_2SO_4 + CO_2 \quad (18)$$

$$Na_2CO_3 + H_2O \rightarrow 2NaOH + CO_2 \quad (19)$$

$$Na_2CO_3 \rightarrow Na_2O + CO_2 \quad (20)$$

$$Na_2O + H_2O \rightarrow 2NaOH \quad (21)$$

$$Na_2CO_3 + 2C \rightarrow 2Na_{(g)} + 3CO \quad (22)$$

Sodium can vaporize from smelt (Equation 23) and react with H_2O to form NaOH (Equation 24) (Vakkilainen, 2005).

$$Na_{(c)} \rightarrow Na_{(g)} \quad (23)$$

$$Na_{(g)} + H_2O \rightarrow NaOH + H \quad (24)$$

Chlorine in the black liquor is present almost exclusively as NaCl. When the liquor burns, this salt volatilises directly from the char (Equation 25), so most chlorine reaching the gas phase originates from NaCl evaporation. It is unclear whether it is released as pure Cl(g), Cl_2 or NaCl. It however reacts very fast to form hydrogen chloride (HCl) (Equations 26 and 27). (Vakkilainen, 2005)

$$NaCl_{(s,l)} \rightarrow NaCl_{(g)} \quad (25)$$

$$NaCl + NaHSO_4 \rightarrow HCl + Na_2SO_4 \quad (26)$$

$$NaCl + H_2O \rightarrow HCl + NaOH \quad (27)$$

NaOH can react with SO_2 (Equation 28), sulfur trioxide (SO_3) (Equation 29) or sodium bisulfate ($NaHSO_4$) (Equation 30) to form sodium bisulfate ($NaHSO_3$) or Na_2SO_4 (Vakkilainen, 2005).

$$NaOH + SO_2 \rightarrow NaHSO_3 \quad (28)$$

$$2NaOH + SO_3 \rightarrow Na_2SO_4 + H_2O \quad (29)$$

$$NaOH + NaHSO_4 \rightarrow Na_2SO_4 + H_2O \quad (30)$$

Na_2SO_4 can react with gases producing Na_2S (Equations 31 and 32). Na_2SO_4 can also decompose producing SO_2, O_2 and volatile sodium (Equation 33). Decomposing is more favorable at high temperatures and low oxygen concentrations. (Vakkilainen, 2005)

$$Na_2SO_4 + 4CO \rightarrow Na_2S + 4CO_2 \quad (31)$$

$$Na_2SO_4 + 4H_2 \rightarrow Na_2S + 4H_2O \quad (32)$$

$$Na_2SO_4 \rightarrow 2Na_{(g)} + SO_2 + O_2 \quad (33)$$

Sodium thiosulfate ($Na_2S_2O_3$) can react with CO_2 or CO to produce sodium compounds and TRS (Equations 34 and 35) (Vakkilainen, 2005).

$$Na_2S_2O_3 + CO_2 \rightarrow Na_2CO_3 + SO_2 + S \quad (34)$$

$$Na_2S_2O_3 + 3CO \rightarrow Na_2S + S + 3CO_2 \quad (35)$$

Flue gas system transports combusted material from the furnace safely to the atmosphere. Flue gases pass through heat transfer surfaces where some of the heat is recovered, and then it flows through flue gas ducts, dampers, a flue gas fan, ESP, a possible scrubber and stack. Collected fly ash is transferred from ESP to mix tank where it is mixed with about 50% DS liquor and pumped back to the evaporator to help it operate in high DS. (Vakkilainen, 2005)

Some of the gases end up as emissions. TRS species include H_2S, methyl mercaptan (CH_4S), dimethyl sulfide ($(CH_3)_2S$) and dimethyl disulfide (CH_3SSCH_3), and they are formed because of a cold char bed and poor mixing. Most of the TRS species will oxidize in a modern KRB furnace to SO_2 when sufficient temperature and mixing are involved. CO is produced because of incomplete combustion due to a lack of excess oxygen. Higher furnace temperature and longer residence time decrease CO emissions. NO_x emissions increase when black liquor DS is increased and when NCG and dissolved vent gases are combusted in the furnace. Volatile organic compound (VOC) emissions are low and mainly of low molecular weight. (Vakkilainen, 2005)

3.3 Heat transfer from furnace

KRBs have different energy production capacities. Boiler dimensions affect daily DS firing rate. Black liquor DS firing rate and composition affect combustion efficiency and fouling speed. Combustion and char bed stability affect heat production. The tube materials' corrosion resistance limits heat transfer surfaces' maximum temperatures. Heat transfer surface conditions, such as cleanliness, affect heat transfer efficiency and steam pressure. Steam pressure and temperature affect turbine performance. (Vakkilainen, 2005)

DS firing rate ($\dot{m}DS$) is how much black liquor is sprayed into the furnace related to time (kgDS/s). Total heat input (Q_{tot}) considers both HHV and DS firing rate and indicates how much energy is produced at combustion related to time (MW). Net heat input (Q_{net}) uses LHV and DS firing rate and indicates energy production while considering energy losses (MW). Floor loading or hearth heat release rate (HHRR) indicates how much heat energy is produced related to furnace floor area (MW/m^2). Effective projected surface area

(EPRS) is the total furnace wall area excluding floor area (m^2). (Vakkilainen, 2005)

The furnace must be tall enough to give the droplet the residence time needed to complete its combustion. Operating experience shows that about 4.5 seconds is required. Applying this rule, the minimum furnace height rises as black liquor DS is increased even if the applied HHRR is higher. In practice this means that two boilers of same specific loading, but widely different capacity would have an equal height. For nearly all KRBs the furnace height seems to be about three times the furnace width. If furnace wall heat flux is assumed to be constant, then for same HHRR the relative height should be constant. In practice, however, the larger the KRB, the lower is the relative height needed for complete combustion. This is because doubling the width quadruples the capacity, and if height is doubled as well then the furnace volume increases eight times. Larger boilers have consequently more time to finish combustion. Table 5 shows how black liquor DS content affect required minimum height of black liquor guns to achieve total combustion. (Vakkilainen, 2005)

Table 5. Furnace height required to ensure a 4.5 seconds residence time and total combustion in different DS (adapted from Vakkilainen, 2005).

DS	HHRR	Minimum height
(%)	(MW/m^2)	(m)
65	2.8	17
75	3.3	19
85	3.8	22
90	4	25

Heat flux (q) can be defined as the energy in transit owing to a temperature difference per unit cross-sectional area normal to the direction of the flux (W/m^2) (Childs, 1999). Heat flux is used to calculate how heat energy transfers through solid surfaces, liquid and vapor. Average heat flux (q_a) is typically around 60-100 kW/m^2 in a KRB (Vakkilainen, 2005). Heat flux output depends on height as its usually strongest at the lower parts of the furnace, where the char bed and combustion are active, and lowers when moving towards the top of the furnace. Internal research about heat flux vertical distribution was provided by Valmet (Figure 12) which shows that highest heat flux multipliers 160% are around 20-25% of furnace height from furnace floor to nose arch upper edge. Heat flux curve has a similarity to Figure 13, where temperature curve highest point is at 15 meters. However, furnace heat flux profiles differ from one boiler to another (Vakkilainen, 2005).

High furnace temperatures increase heat fluxes and corrosion caused by high cladding temperatures. High heat fluxes reduce or even remove the protective frozen char bed and smelt layers covering the tubes. (Vakkilainen, 2005)

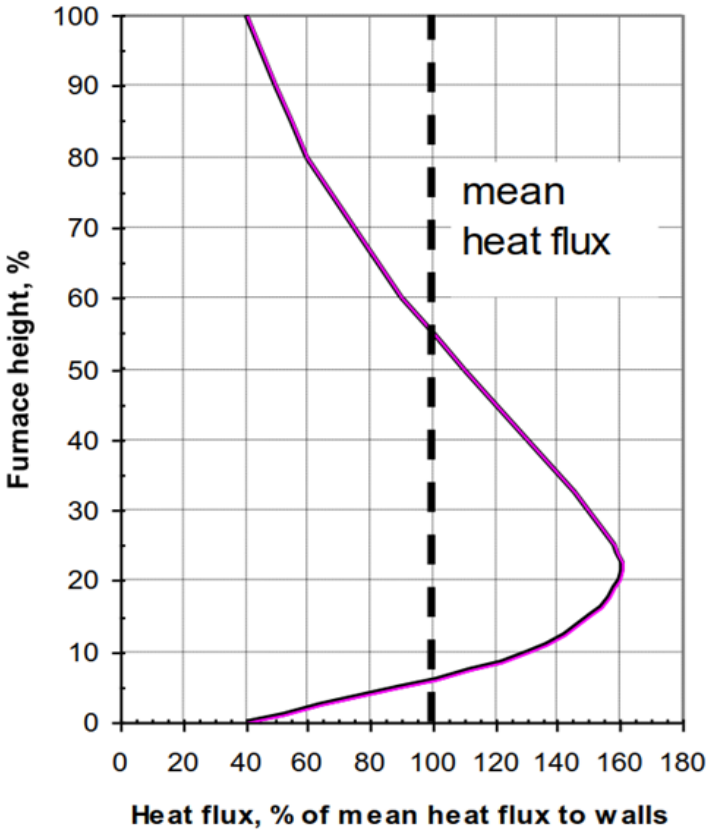

Figure 12. Heat flux distribution from furnace floor to nose arch upper edge (Tavares & Karjunen, 2020).

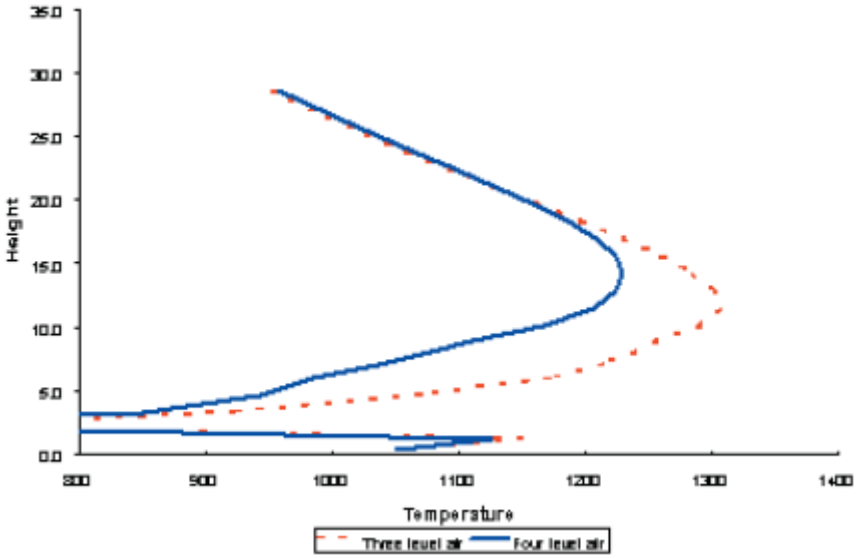

Figure 13. Furnace temperature related to height (Vakkilainen, 2005).

3.4 Water/steam circulation

Kraft recovery boilers generate energy by producing steam from heat energy. Water goes through multiple steps before it transforms into steam. Water circulation system (Figure 14) starts from the feedwater tank, where demineralized water is pumped. Feedwater tank capacity is around 15-45 minutes of feedwater usage, and it is situated at a height of 10-30 meters (Vakkilainen, 2005). Oxygen is removed from water mechanically in deaerator where water is sprayed into fine droplets, heated to the boiling point and stripped from gases with a small counter-current flow of steam (Bartholomew, n.d.).

Boiler feedwater pump transfers water through feedwater piping into economizer where it is preheated using flue gases to reduce flue gases end temperature and improve boiler heat efficiency. Typically, economizer inlet temperature is around 350-450 °C. Water is heated as close to saturation temperature as possible without boiling to prevent unstable water surges, which could harm boiler operation and even damage it. (Vakkilainen, 2005)

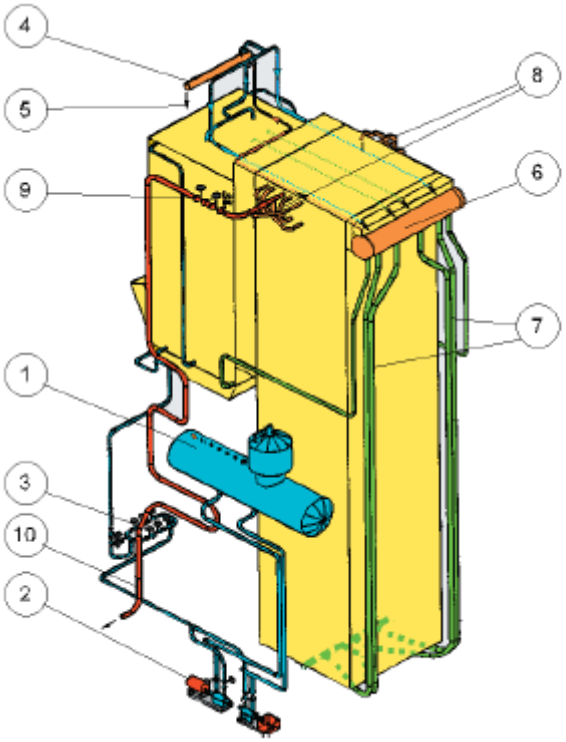

1	Feedwater tank
2	Boiler water pump
3	Feedwater piping
4	Sweet water condenser
5	Desuperheater
6	Steam drum
7	Downcomers
8	Superheaters
9	Main steam valves
10	Main steam line

Figure 14. Water circulation system (Vakkilainen, 2005).

Water travels to steam drum where steam is separated from the water using gravitation, screens and cyclone separators. All modern KRBs are single drum type because it allows bigger capacity, higher pressure and can be operated more safely and economically. Natural circulation (Figure 15) loops

start from downcomers where saturated water travels to downcomers, is divided evenly with headers and flows to riser tubes where furnace heat is applied. Water/steam mixture heats up and rises in the wall tubes, is merged in header and ends up in steam drum. Driving force of natural circulation is weight difference between saturated water in downcomers and water/steam mixture in furnace wall tubes. Higher pressure decreases driving force as density difference becomes smaller. Circulation is limited by friction losses in surfaces, downcomers, headers, and risers. Circulation can be improved by increasing the height difference and heat flux in the lower part of the furnace. (Vakkilainen, 2005)

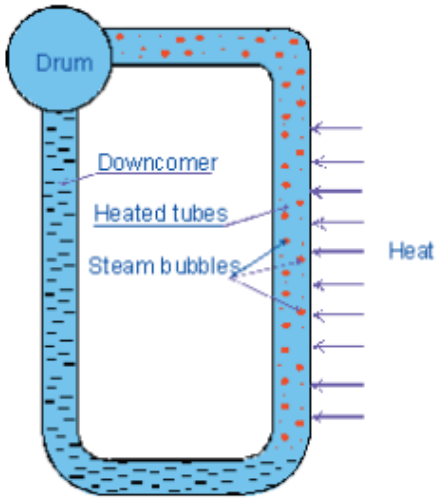

Figure 15. Principle of natural circulation (Vakkilainen, 2005).

Target of boiler design is to increase steam pressure as it increases energy production significantly. Steam drum pressures are usually between 60-120 bar and saturated water velocity is around 2 m/s. Tube material pressure and corrosion resistances and physical challenges of boiler water natural circulation limit the construction of boilers with higher pressure input.

In steam drum all steam should be separated from water because it causes problem in the downcomers. Steam is transferred to superheaters where it gets superheated by furnace heat radiation and convection energy. Superheated steam is channelled to turbines where high-pressure steam produce energy, medium-pressure steam is extracted from turbine to cooking, soot-blowing and high DS evaporation and low-pressure steam is used for process heating. (Vakkilainen, 2005)

Higher steam drum pressure increases turbine energy production performance. Increasing steam temperature that ends into a condensing turbine from 400 °C to 500 °C, increase power generation by 20% (Brossard et al., 2011).

3.5 Furnace enclosure and tube properties

KRB furnace surfaces consist of heat transfer surface tubes whose main purpose is to transfer heat from black liquor combustion to water/steam mixture inside the tube and to prevent gas escaping from the furnace. Furnace internal surfaces consist of floor tubes (Figure 16), wall tubes (Figure 17), nose arch and screen tubes. Char bed is formed on top of floor tubes, so it is important to protect them from high temperatures with cladding materials, effective water circulation and smelt deposits layer. (Vakkilainen, 2005)

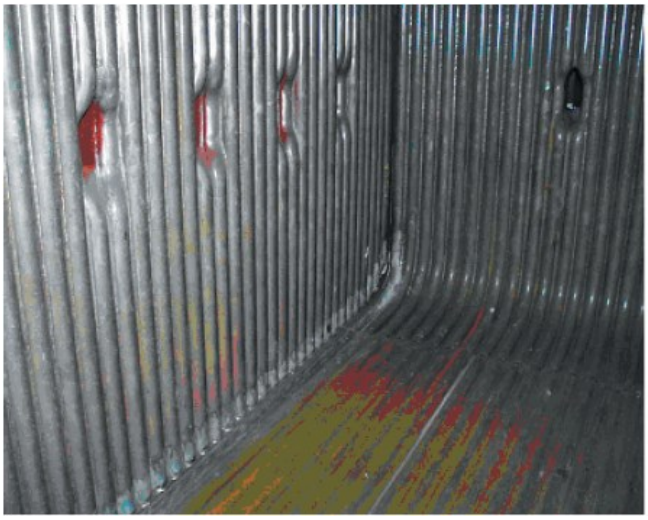

Figure 16. Furnace floor, wall tubes and primary air ports (Vakkilainen, 2005).

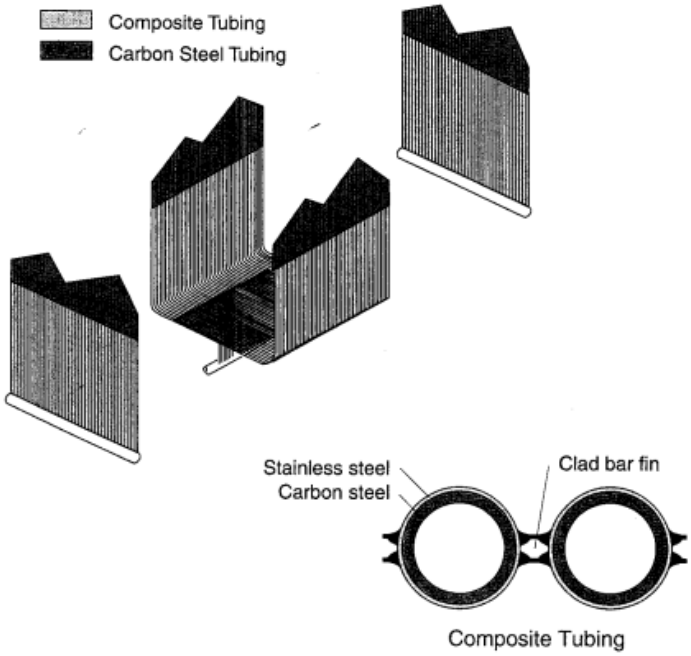

Figure 17. KRB tubes at furnace lower level (Adams, 1997).

Wall tubes (Figure 18) form protective vertical wall around furnace and provide high heat transfer surface area. They have a protective cladding layer at the lower levels of furnace and a uniform carbon steel structure from middle to upper furnace (Vakkilainen, 2005).

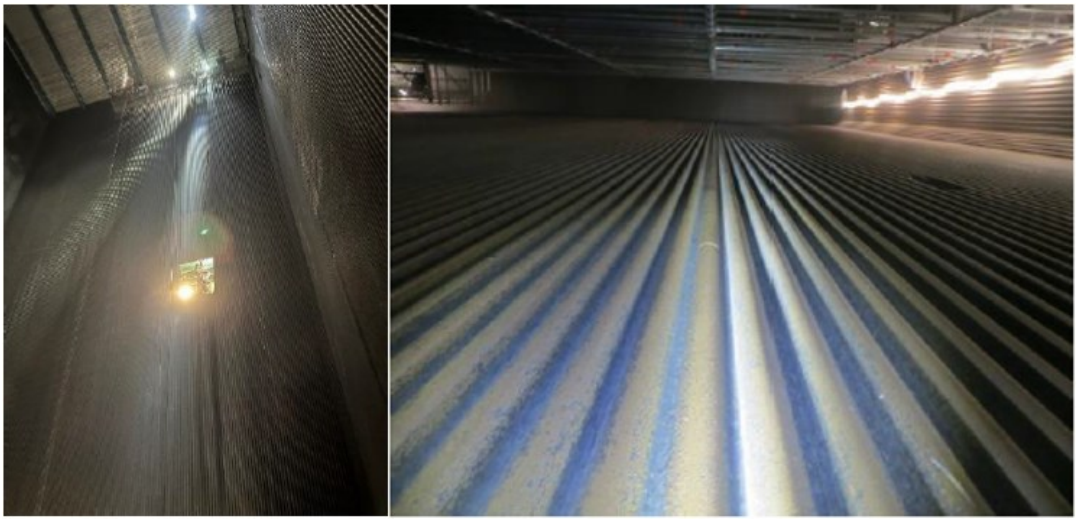

Figure 18. Wall tubes from inside the furnace (internal document from Nilsson, 2023).

Vertical wall tubes need to be bent around air ports (Figure 19), liquor guns (Figure 20), and other openings such as fossil fuel burners, entry doors, and inspection ports. These are formed by bending one or several wall tubes either directly to the side or on the outside of the furnace. (Adams, 1997)

Figure 19. Primary air ports (internal document from Nilsson, 2023).

Figure 20. Black liquor gun opening (internal report form Isberg, 2018).

Nose arch is located on the rear wall of the furnace, and it protects superheaters from direct furnace radiation and forces combustion gases to flow around the corner towards the boiler exit opening while producing uniform flow over the heat transfer surfaces. Screen tubes cool combustion gases before they get in contact with superheaters. (Adams, 1997)

Tubes are welded together tangentially or with a fin if membrane structure is used (Vakkilainen, 2005). In modern KRBs, the use of composite bars with smaller widths, has minimized corrosion of the membrane tubes and fins (Tran et al., 1988). Tube material is usually entirely carbon steel or consists of an inside layer made from carbon steel and an outside layer cladding made of austenitic stainless steel, such as AISI 304 or AISI 304L or higher alloy Sanicro 38 depending on tube location and corrosion resistance requirements. Figure 21 and 22 shows wall tube membrane structure.

Tube outside diameter is usually around 63.2-63.8 mm, tube inside diameter is around 48.18-50.74 mm and total wall thickness is around 6.53-7.51 mm. AISI 304L cladding thickness is around 1.25-2.25 mm and carbon steel thickness is around 4.88-6.26 mm and for Sanicro 38 cladding thickness is slightly higher 1.42-2.42 mm and carbon steel is slightly lower 4.71-6.09 mm. (Internal document from Andritz, n.d.)

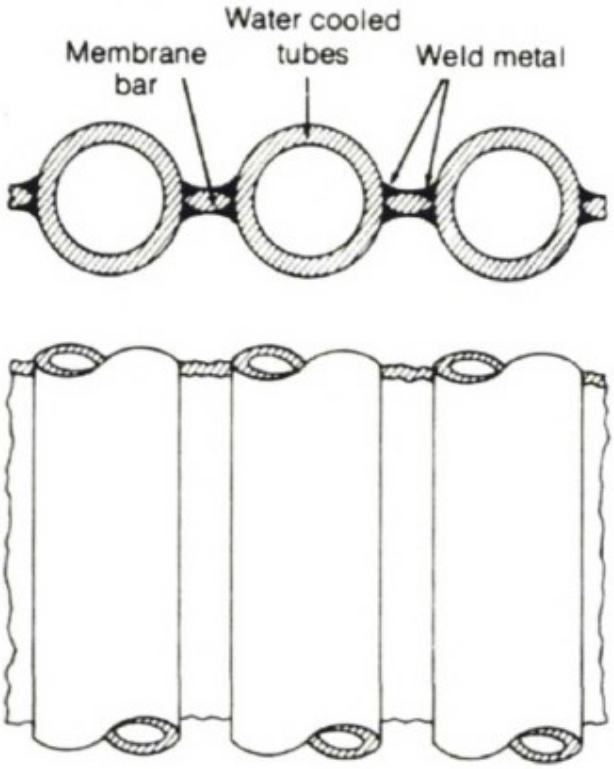

Figure 21. KRB wall tube membrane structure, which consists of tubes and fins welded together (Smook, 2002).

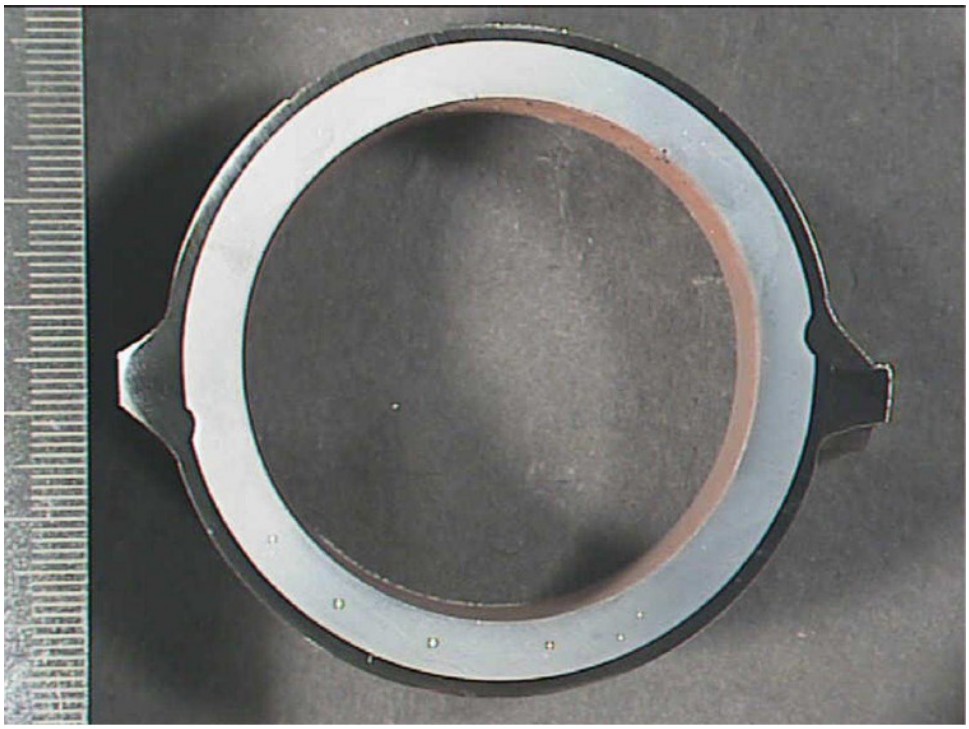

Figure 22. Cross-section sample of KRB wall tube (internal document from Karhula, 2022).

Low-cost carbon steels are used as the preferred construction material across industries and are considered a more economical option than the costly corrosion-resistant alloys (Dwivedi et al., 2017). Carbon steel offers high strength, especially against pressure, and good thermal conductivity. Carbon steel tubes can withstand high pressure up to 160 bar (Steel, n.d.). However, it is not a suitable material in lower furnace as such, as it corrodes rapidly in contact with molten smelt and sulfur-rich environment, especially in high temperatures (Vakkilainen, 2005). Carbon steels typically contain less than 1.5% carbon content along with the minute presence of Mn, Si, P and S (Dwivedi et al., 2017). Carbon steel density is 7.9 g/cm^3 (Alleima, n.d.-b). CO_2 corrosion and H_2S corrosion are the most common corrosion types for carbon steel in KRB (Dwivedi et al., 2017).

Austenitic stainless steel such as AISI 304 and AISI 304L became common cladding material in KRBs in the late 1970s (Vakkilainen, 2005). AISI 304 and AISI 304L stainless steels are variations of the 18 percent chromium and 8 percent nickel austenitic alloys, which have resistance to corrosion and oxidation, high strength and excellent formability (American, n.d.). Chromium in alloy provides resistance to oxidizing environments, organic acids and some cases reducing acids and nickel in alloy provides resistance to moderately reducing environments (American, n.d.). Austenitic stainless steels have relatively good resistance against organic acids at moderate temperatures, salt solutions such as sulfates, sulfides and sulfites and caustic solutions at moderate temperatures (Alleima, n.d.-a). AISI 304L is the most typical metal used to control sulfidation corrosion as it does not corrode at significant rate until 480 ^{o}C is reached. (Vakkilainen, 2005). Type AISI 304 and AISI 304L alloys are susceptible to stress corrosion cracking (SCC) in halides because of their relatively low nickel content (American, n.d.). AISI 304L contains around 18-20 weight-% of Cr, 8-12 weight-% of Ni with minute presence of Mn, Si, Mo, Cu, N, P, S and C and differs from AISI 304 that it has lower carbon content and lower corrosion rate (CR) (American, n.d.). Lower carbon primarily affects sensitization and intergranular corrosion as when the carbon content is low, welding does not lead to the formation of chromium carbides, which would otherwise precipitate at grain boundaries, impair passivation, and make the material more prone to corrosion. Austenitic stainless steel density is 7.9 g/cm^3 (Alleima, n.d.-a; American, n.d.).

The highly reducing environments and sulfuric acid environments are shown to be too aggressive for austenitic stainless steel materials. Exposure of the 18-8 austenitic stainless steels to temperatures of 427-816°C may cause precipitation of chromium carbides in grain boundaries and might cause intergranular corrosion when exposed to aggressive environments. (American, n.d.).

Normal carbon steel has about 10 times the CR in molten hydroxide than AISI 304L. AISI 304L and carbon steel have different thermal expansion behavior which causes stress and advances possible tube cracking when composite tubes are made of austenitic stainless steel and are subjected to thermal cycles. (Vakkilainen, 2005)

AISI 304L stainless steel can start cracking in 150-200 °C temperature when hydrated sodium sulfide ($Na_2S \cdot 9H_2O$) is present. Cracking of AISI 304L composite tubing has been documented in air ports, smelt spouts openings, as well as floor tubes. (Keiser et al., 2001)

CR depends on H_2S concentration, temperature, pressure, and permeability of the sulfide scale. Chromium in the steel helps to stabilize the scale and slow the diffusion process. At high pressure and temperature, when H_2S is present, corrosion attacks are more aggressive to the extent that low chromium (5-9%) steels are not adequate. Molecular hydrogen dissociates slightly to provide atomic hydrogen which is more reactive and can diffuse through steel. Hydrogen combines with the sulfide scale, reducing it and creating porous structure which the iron and sulfur ions can maintain high diffusion rates. (Nickel, n.d.)

Stainless steel AISI 304L seems to last well in the furnace walls above the char bed (Vakkilainen, 2005). Austenitic stainless steels can be used for most wall tube sections including the screen and nose arch as long as metal temperatures remain moderate and exposure to chloride-rich molten salts and H_2S is limited, and thermal-fatigue conditions are minimal.

Sanicro 38 is a nickel-rich, Alloy 825-modified austenitic steel that Alleima (formerly Sandvik) developed specifically for the most aggressive zones of KRB floors, lower walls and air ports where molten smelt, high chloride volatiles and severe thermal-fatigue cycling quickly destroy AISI 304L claddings on tubes. It is a widespread cladding material that offers improved corrosion protection for lower furnace and is much less prone to cracking in floor conditions (Vakkilainen, 2005). It contains around 38 weight-% of Ni, 20 weight-% of Cr, 3 weight-% of Mo and with minute presence of Cu, Ti, Mn, Si and C. High nickel content gives Sanicro 38 substantially higher resistance to H_2S induced corrosion (Sandvik, n.d.). Molybdenum gives alloy 825 good resistance to chloride induced localized corrosion, including pitting, crevice corrosion, and stress corrosion cracking (SCC) (Corrosion, n.d.). The more alloying elements present, the more durable the material becomes. Chromium, nickel, molybdenum containing austenitic materials are highly corrosion resistant (Kawahara, 2006). Chromium enhances resistance in oxidizing environments, molybdenum in reducing ones, and nickel preserves the austenitic structure while helping guard against certain forms of corrosion.

Galvanic corrosion is lower in carbon steel when Sanicro 38 is used at lower wall tubes (Vakkilainen, 2005). Sanicro 38 density is 8.1 g/cm^3 (Alleima, n.d.-b).

Carbon steel has high thermal conductivity compared to austenitic stainless steels and Sanicro 38 which makes it good material for heat transferring (Tables 6 and 7). As can be seen from Table 6 Sanicro 38 has highest corrosion resistance compared to AISI 304L and carbon steel. AISI 304L has low SCC resistance because carbon steel and AISI 304L have significant difference in thermal expansion (Tables 6 and 8). The bigger is the difference in the thermal expansion between the substrate and the cladding, the lower is the fatigue limit (Vakkilainen, 2005).

Table 6. Comparison of tube material properties (adapted from Vakkilainen, 2005).

Property	Unit	Carbon steel	304L	Sanicro 38
Main elements		Fe	20Cr-10Ni	20Cr-40Ni
Thermal conductivity	(W/mK)	41	19	16
Thermal expansion	(10^{-6}/K)	13.5	17.5	14.9
SCC resistance		Excellent	Low	High
Corrosion resistance		Low	Moderate	Excellent

Table 7. Material thermal conductivities related to temperature.

Temperature	Carbon steel (4L7)	Austenitic stainless steel (304L)	Sanicro 38	Magnetite (Fe_3O_4)	Hematite (Fe_2O_3)
	Thermal conductivity				
(^{o}C)	(W/mK)				
20		15			
23			11		
100	48	16	12	3.72	5.92
200	47	18		3.58	2.25
300	46	20	16	3.44	4.59
400	44	22		3.31	3.93
500	42	23	19		
600		25			
700		26			
Reference	(Alleima, n.d.-b)	(Alleima, n.d.-a)	(Alleima, n.d.-c)	(Molgaard and Smeltzer, 1971)	

Table 8. Thermal expansion mean values temperature ranges (x10-6) (adapted from Alleima, n.d.-b).

Temperature (°C)	Carbon steel (4L7)	Austenitic stainless steel (304L)	Sanicro 38
30-100	12.3	16.5	14.2
30-200	12.8	17.2	14.6
30-300	13.5	17.7	14.9
30-400	14.0	18	15.1
30-500	14.3	18.4	15.3

3.6 Corrosion, fouling and deposits

Correct material choices are essential when designing KRB furnace, as high temperatures and corrosive atmosphere cause stress to furnace surfaces. Eagerness to increase steam pressure increases tube temperatures at lower furnace, which increases sulfidation risk (Yli-Olli et al., 2007). Corrosion varies in different locations in the KRB because of great differences in heat transfer surface temperatures and flue gas and deposit chemistries (Tran et al., 1988).

There are several different kinds of corrosion in KRB, which are mostly location-orientated. Water side corrosion occurs in water/steam side of the tube due to impurities in feedwater. Low temperature corrosion occurs in economizers and air heaters, and it is linked to the formation of acidic deposits. Gas side corrosion of heat transfer surfaces is caused by the formation of deposits that have a molten alkali phase and a gaseous reducing atmosphere. High temperature corrosion occurs on superheater surfaces. (Vakkilainen, 2005)

The most common types of corrosion include sulfidation corrosion of wall tubes in the lower furnace area, molten hydroxide corrosion around air ports, cracking of smelt spout opening tubes, and sulfidation/oxidation corrosion of superheater tubes. Less common corrosion forms are acidic sulfate corrosion in the boiler bank, oxidation corrosion of casing steels in the boiler bank and economizer regions, and cold side corrosion of wall tubes due to moist conditions during boiler outages. Corrosion has also been observed on screen tubes and upper boiler wall tubes near the furnace roof. (Tran et al., 1988)

Corrosion resistance is mostly related to how dense deposit layers are formed at the metal surfaces, as they prevent corrosive agent passage. Carbon steel tube surfaces consist of a protective magnetite (Fe_3O_4) layer and a flaky and porous hematite (Fe_2O_3) layer where gases can move easily and cause a high CR (Figure 23). Outer layers consist of solidified ash and black liquor

particles, which form deposits and condensation of vapors and gaseous species. Regarding corrosion, the layer closest to the tube is the most important. (Vakkilainen, 2005; Tran et al., 1988)

Fe_3O_4 thermal conductivity is 3-4 W/mK and Fe_2O_3 thermal conductivity is 4-7 W/mK (Dooley, 2003). Thermal conductivities at room temperature for Fe_3O_4 is 2.9 W/mK and for Fe_2O_3 0.6 W/mK (Dillon et al., 2011). Thermal conductivities related to temperature are in Table 7.

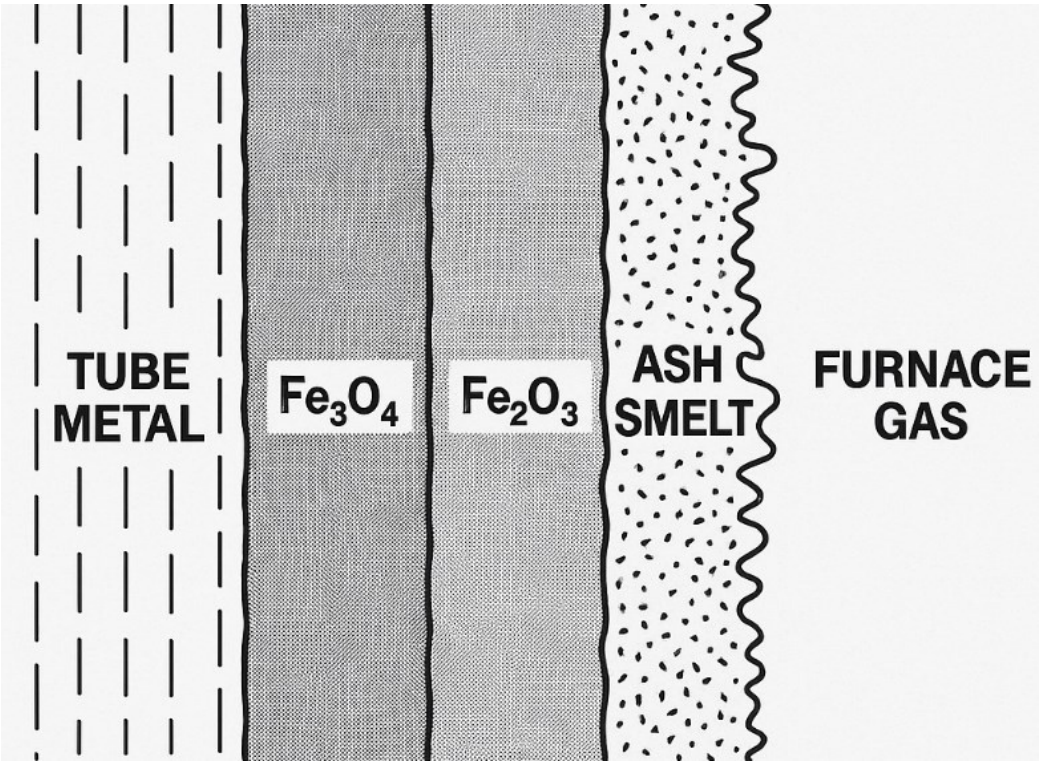

Figure 23. Surface of a carbon steel tube facing furnace (adapted from Vakkilainen, 2005).

The localized corrosion was considered to be accelerated by the breakdown of the protective oxides layer due to the thermal stresses that resulted from the difference in the thermal expansion rates of tube's carbon-steel core and stainless steel cladding. Once that barrier is disrupted, sulfidation and oxidation become the dominant corrosion mechanisms. Thermal cycles further enlarges the loss as each heat-up/ cool-down step cracks or spalls portions of the scale, exposing fresh metal. At the same time, the ash that settles on the scale raises the local partial pressures of chlorine and sulfur, intensifying chlorination and sulfidation reactions at the metal/scale interface. In this way, daily temperature fluctuations chiefly damage the scale itself, while differential temperatures amplify the environmental side of the problem by enriching aggressive species in the deposit layer. Under the thick, partially intact scale a low-oxygen micro-environment develops, and a cluster of

reactions chlorination, sulfidation, and residual oxidation continue to propagate the corrosion front even during otherwise steady operation. (Kawahara, 2006)

Sulfidation is most common type of corrosion in the lower furnace because of the nature of the black liquor and its sulfur content. In sulfidation, H_2S reacts with iron, forming iron sulfides (FeS), which cause damage to protective oxidized layer reducing its ability to protect the metal (Vakkilainen, 2005; Tran et al., 1988). Sulfidation of Fe_2O_3 (Equation 36) and sulfidation of iron oxide (FeO) (Equation 37) occurs at the surface layer (Stewart and Arnold, 2013). Acidic sulfate corrosion occurs in boiler bank and is caused by high SO_2 emissions (Vakkilainen, 2005).

$$Fe_2O_3 + 3H_2S \rightarrow Fe_2S_3 + H_2O \quad (36)$$

$$FeO + H_2S \rightarrow FeS + H_2O \quad (37)$$

The presence of H_2S would constrain the generation of oxides in the passivation layer, thereby impairing the corrosion property of steel (Li et al., 2021). AISI 304L forms protective oxidation layer to protect it against corrosion if water vapor is present but without it, sulfidation starts at even low H_2S levels and accelerates when H_2S concentration increases (Yli-Olli et al., 2007). Alloy 825 forms protective film from Cr, Ni and Mo oxides, which is highly corrosion-resistant, but the presence of sulfide reduces its effectiveness (Feng et al., 2021). CR decreases when chromium containing metal is used, as chromium oxides at the surface of the alloy are very slow to react even in thermodynamically unstable environment (Barnhart, 1997). Possible corrosion mechanism for Sanicro 38 is shown in Figure 24.

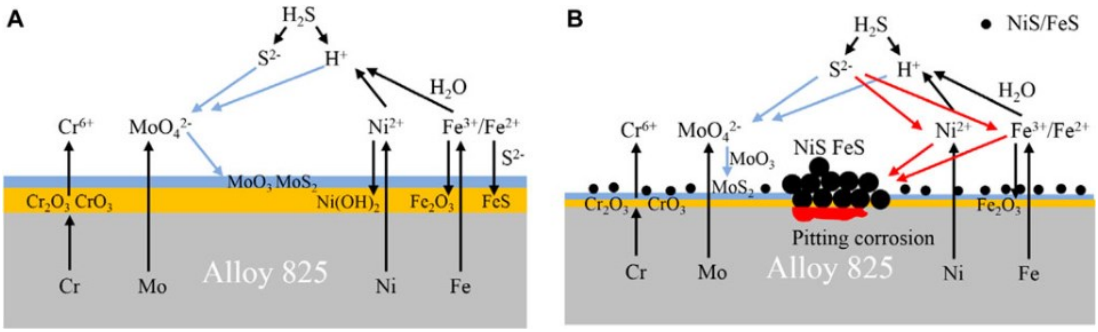

Figure 24. Possible corrosion mechanisms of Alloy 825 at 150 °C (A) and at 230 °C (B) (Feng et al., 2021).

H_2S concentrations depending on furnace location have been gathered on Table 9. Carbon steel, austenitic stainless steel and Sanicro 38 CR related to H_2S concentrations and temperatures have been gathered on Table 10 and material specific CR curves related to temperature in Figures 25-27.

Table 9. H_2S concentrations at different furnace locations.

Location	H_2S concentration (ppm)	Reference
Char bed	60-750	(Connolly and Van Heiningen, 2004 from Vaino et al., 2010)
	250-750	(Borg et al., 1973 from Vakkilainen, 2005)
Lower furnace	300	(Borg et al., 1974 from Vakkilainen, 2005)
	1000	(Perjyd and Hupa, 1984 from Vakkilainen, 2005)
	3940	(Vainio et al., 2010)
	1-10000	(Roos, 1968 from Vakkilainen, 2005)
	200000	(Singh et al.,1999 from Vakkilainen, 2005)
Above tertiary air port	10-50	(Vakkilainen and Holm, 2001 from Vakkilainen, 2005)

Table 10. Materials CR in different temperatures and H_2S concentrations.

Temperature (°C)	Corrosion rating (mm/y)			H_2S concentration ppm	Comments	Reference
	Carbon steel	Austenitic stainless steel	Sanicro 38			
250	0.1	0	0	1000	AISI 304, AISI 310	(Tavares & Karjunen, 2020)
300	0.4	0.1	0	1000		
350	0.8	0.3	0	1000		
400	1.7	0.6	0	1000		
450	3.3	1.4	0.2	1000		
500	5.7	2.1	0.3	1000		
250	0.1	0		10000	AISI 304	(Salmenoja and Tuiremo, 2001 from Vakkilainen, 2005)
300	0.2	0		10000		
350	0.4	0		10000		
400	0.7	0.1		10000		
450	1.3	0.3		10000		
500	2.3	0.5		10000		
550	3.5	0.8		10000		
600	4.7	1.3		10000		
360		0.02	0.02	5000 (H_2S-N_2 vppm)	304L	(Mäkipää et al., 2001)
400		0.05	0.15	5000 (H_2S-N_2 vppm)		

Temperature (°C)	Corrosion rating (mm/y)			H_2S concentration ppm	Comments	Reference
	Carbon steel	Austenitic stainless steel	Sanicro 38			
300	0.8	0		10000	5 % Cr carbon steel, 18Cr-8Ni	(Nickel, n.d.)
350	1.9	0		10000		
400		0		10000		
450		0.1		10000		
420		0.12		Low	S30403	(Nimmervoll et al., 2022)
480		0.23		Low		
580		0.8		Low		
420		0.12		Medium		
480		0.27		Medium		
580		0.95		Medium		
420		0.16		High		
480		0.28		High		
580		1.32		High		
440		0.05	0.10	500	304L (no water vapor)	(Yli-Olli et al., 2007)
440		0.08	0.15	1000		
440		0.06	0.13	2500		
440		0.09	0.20	5000		
440	4	0.6	0.07		3R12	(Pohjanne, 2013)
High		0.057	0		AISI 304, Sanicro 38, measured	(Kiwa, 2014)
Varies		0.058			AISI 304, measured	(Khodahami, 2024)
		0.059				
		0.041				
		0.047				
		0.030				
		0.026				
High		2.000			AISI 304, measured	(Liikola, 2015)

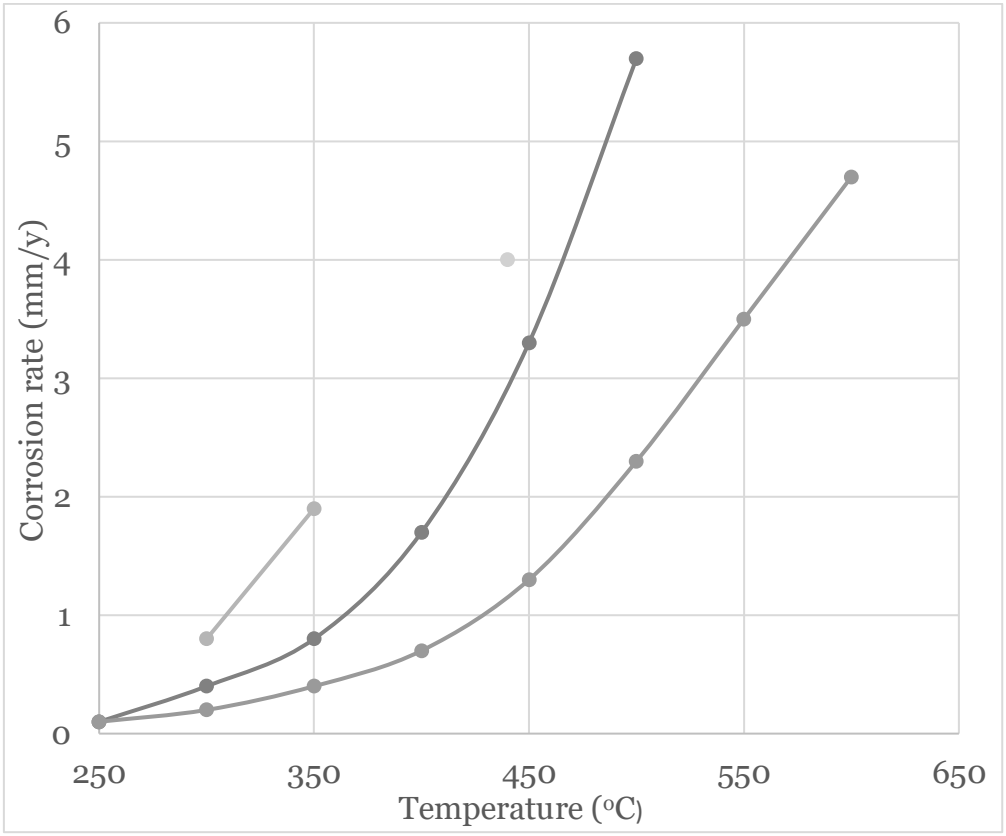

Figure 25. Carbon steel CR as a function of temperature from Table 10.

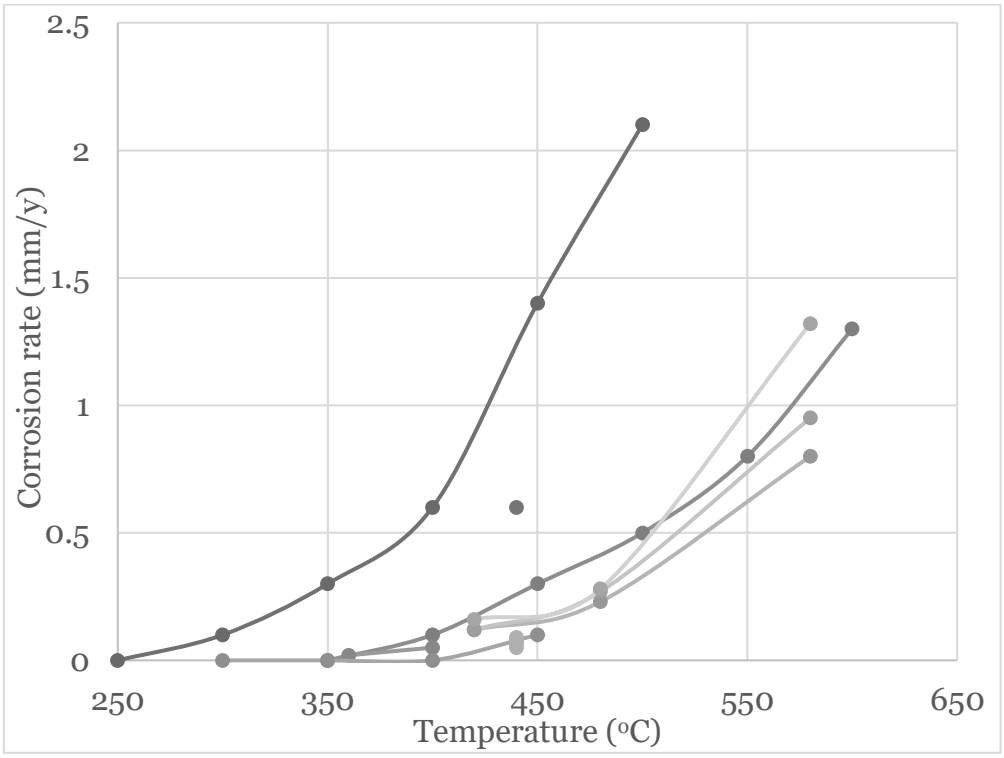

Figure 26. Austenitic stainless steel CR as a function of temperature from Table 10.

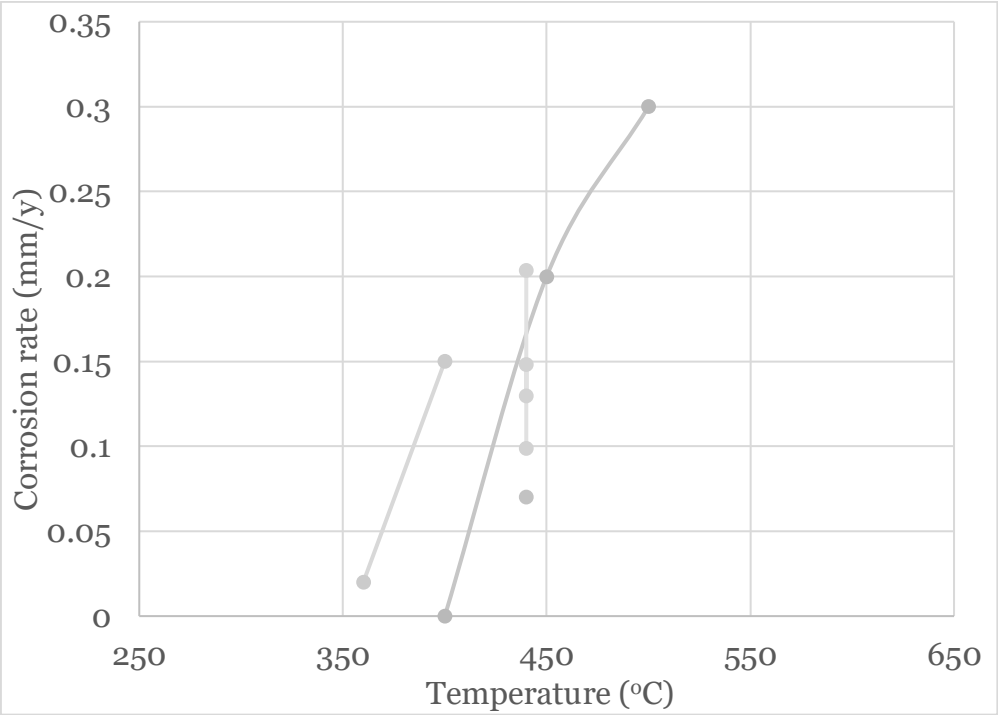

Figure 27. Sanicro 38 CR as a function of temperature from Table 10.

Deposit and surface fouling occurs in different ways. After the liquor droplets complete char combustion, their inorganic residue reaches a high temperature and turns molten. Most droplets end up into the char bed where they flow towards the smelt spout openings as a continuous film. As smelt temperature drops when it gets in closer with cooled floor tubes, it partially solidifies forming a protective layer over the floor tubes. Black liquor spraying in conjunction of air flows cause some of the black liquor droplets to end up flying towards wall tubes forming smelt layer. Smelt solidifies when it comes in contact with a cooler surface. Flue gases carry droplets towards higher furnace levels where they form ash layers on thermal conductive surfaces.

Smelt and ash layer thickness depends on their properties such as melting point and thermal conductivity, black liquor properties, water/steam pressure and furnace heat input. KRB fireside deposits consist mainly of Na_2CO_3, Na_2SO_4, Na_2S and a small amount of NaCl and potassium salts (Tran et al., 1988). KRB ash deposits are often heterogeneous in nature, with different compositions and structures across the deposit, mainly due to the way of the deposit are formed (Niemi et al., 2019). Thin layer is usually reactive and thick rather static (Vakkilainen, 2005). During combustion and reduction significant amount of alkali compounds vaporize. Combustion gases carry important particles such as H_2S, carbonyl sulfide (COS), Na_2 and NaOH from lower furnace to upper furnace (Hupa, 2007). Small char fragments and liquor particles may entrain in flue gas flow and cause formation of deposits on heat transfer surfaces (Vakkilainen, 2005). Coarser particles size ranges from

10-100 μm (Hupa, 2007). Deposits in the upper furnace consist more of Na_2SO_4 and NaCl and potassium salts and less of Na_2CO_3 and Na_2S compared to the lower furnace (Tran et al., 1988). Smelt and ash thermal conductivity is around 0.15-3 W/mK depending on sintering stage (Robinson et al., 2001). Loose and unsintered deposits' thermal conductivity is 0.15 W/mK (Robinson et al., 1998). Composition of ash will modify deposit composition and melting point (Niemi et al., 2021). Thermal conductivity of frozen smelt is around 0.6 W/mK and smelt melting point is 720 °C (Tan, 2000).

Alkali compounds such as alkali chloride evaporate from hotter particles in the deposit and condense on colder particles closer to the cooled metal surface or even condense on the metal surface (Lindberg et al., 2016; Niemi et al., 2019; Niemi et al., 2017). Sulfur and alkali metals such as sodium and potassium can react in liquid deposits causing corrosion especially in high temperatures because chemical reactions are faster in molten phase as liquid phase provides an electrolyte for electrochemical reactions and liquid phase can dissolve corrosion products and fluidize the ash (Vakkilainen, 2005). AISI 304L corrodes rapidly in molten NaOH at 380 °C at CR of 0.8 mm/y (Crowe and Cameron, 1988). Sulfur, chlorides and potassium lowers smelt melting point and increase viscosity which can make frozen protective layer thinner (Vakkilainen, 2005). Deposits in furnace side are usually dense and sintered on furnace side and porous when closer to heat transfer surface (Niemi et al., 2019; Niemi et al., 2021). Deposit aging has direct effects on the deposit removability and chemistry (Niemi et al., 2019). Heat transfer surface temperature needs to be lower than deposit melting temperature to reduce corrosion (Lindberg et al., 2016).

In chloride corrosion NaCl, chlorine (Cl_2) and HCl gases reacts with iron to produce iron(II) chloride ($FeCl_2$) and when in contact with oxygen reacts back to Fe_2O_3 releasing reactive chloride in gas form (Vakkilainen, 2005). Porous iron oxide structure causes problems as it provides no protection against alkalis and is even optimal for chloride corrosion cycle because of available fresh iron oxides (Vakkilainen, 2005). Alkali chlorides enrich towards the cooled metal surface which can increase chlorine-induced corrosion as the deposits mature over time (Lindberg et al., 2016; Niemi et al., 2019; Niemi et al., 2021). CR increases especially for low alloy steels when chloride content increases in ash, because of higher amount of molten phases (Schaal et al., 2016). Alkali chloride amount in the ash is a key factor in CR (Brossard et al., 2011). Alkali chloride migration into deposit cracks can locally lower the initial melting point, increase the molten fraction, and thus foster both deposit hardening and accelerated corrosion (Niemi et al., 2021). Hotter and shallower char bed causes tube contact with liquid smelt and risk of floor tube cracking especially if smelt is rich of potassium and chloride (Vakkilainen, 2005). Figure 28 shows corroded stainless steel cladding.

Figure 28. Corroded stainless steel cladding (internal report form Isberg, 2018).

Maximum wall tube corrosion is usually observed right above smelt pool. Tube cladding temperature can be high as 400 °C because radiant heat transfer and thinner deposits. Such temperature is too low for melting deposits which rules out possibility of corrosion caused by molten deposits and effects of chloride and potassium at lower furnace corrosion. Na_2CO_3 found in lower furnace deposits protects wall tubes against HCl and SO_2 attacks by converting them to NaCl and Na_2SO_4 (Equations 38 and 39). (Tran et al., 1988)

$$Na_2CO_3 + 2HCl \rightarrow +2NaCl + CO_2 + H_2O \quad (38)$$

$$Na_2CO_3 + SO_2 \rightarrow +Na_2SO_4 + CO \quad (39)$$

In molten hydroxide corrosion sodium oxide (Na_2O) reacts with brittle Fe_2O_3 layer producing $NaFeO_2$ (Equation 40). This is common behind furnace tubes close to air ports, where gases can leak, and at black liquor gun openings. It is a significant corrosion type as carbon steel corrodes in molten hydroxide 10 times faster compared to AISI 304. Cold side corrosion, membrane cracking and tube cracking are common corrosion types in air ports. In cold side corrosion, vaporized NaOH forms deposits on cold back side of air port tubes, which causes a problem if protective cladding isn't present. Larger width of membrane at air ports caused by tube bends increase membrane temperatures and local corrosion. (Vakkilainen, 2005)

$$Fe_2O_3 + Na_2O \rightarrow +2NaFeO_2 \quad (40)$$

Even though KRB furnaces have very reducing environment, high levels of carbon dioxide, hydrogen and reductive gases, general corrosion is not limiting factor of current recovery boiler furnace life cycle. Galvanic corrosion occurs when two metals are in contact to one another, and both are in presence of an electrolyte. Galvanic corrosion happens closest to welds in composite tubing. (Vakkilainen, 2005)

Corrosion rate grows exponentially with the metal temperature, and it is usually located between 1-4 meters from floor tubes (Tavares & Karjunen, 2020). Figure 29 and 30 shows highly corroded and ruptured boiler wall tube due to the pitting corrosion and high pressure.

Strains causes SCC at tube surfaces which enhance chemical corrosion. Thermal fatigue cracks happen in KRB wall tubes when temperature peaks locally and especially if carbon steel and cladding have high difference in thermal expansion. Thermal fatigue causes serious risks as fracture can continue growing through both cladding and carbon steel layers. (Vakkilainen, 2005)

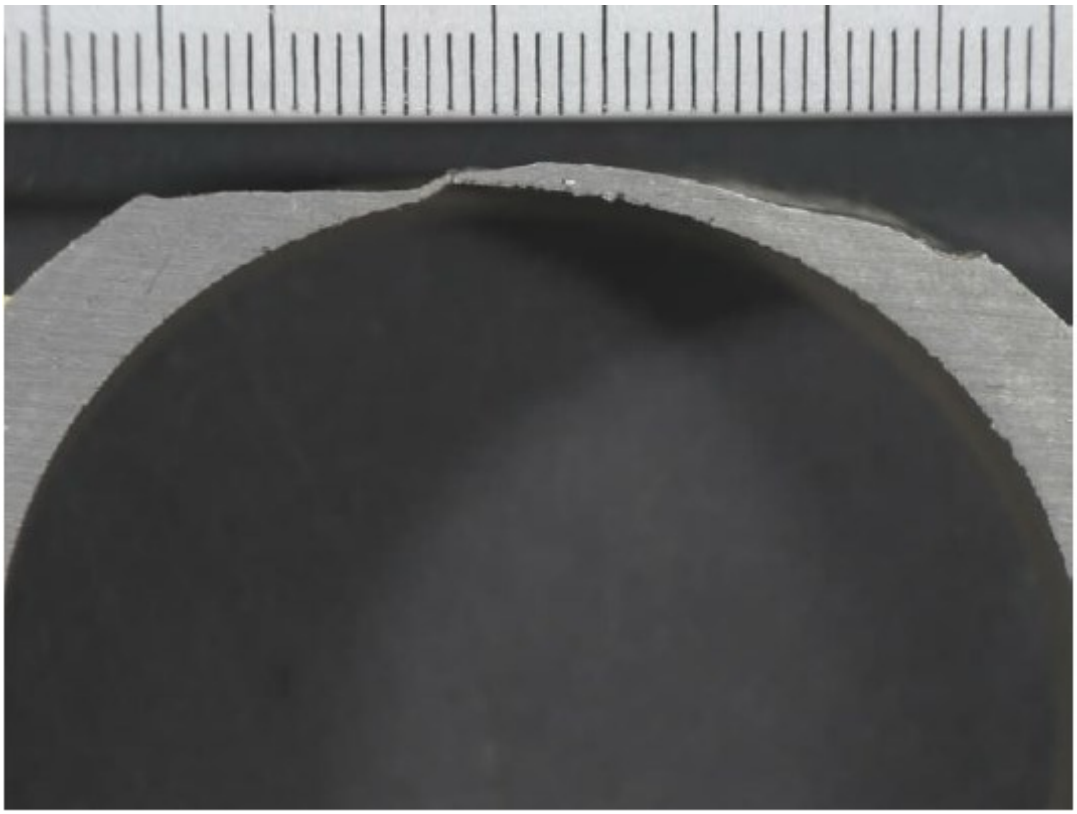

Figure 29. Cross section of highly corroded and ruptured boiler wall tube (internal report from Inkinen et al., 2024).

Figure 30. Corroded and ruptured wall tube due pitting corrosion and pressure (internal report from Inkinen et al., 2024).

Erosion is caused by high velocity particles such as ash colliding with heat transfer surfaces. Flue gas ash is rather soft, and its velocities are moderate 4-12 m/s therefore, erosion is minor in KRBs. However, erosion occurs during sootblowing as pressured steam contains condensate droplets, which hit the tubes. Erosion increases when velocity increases. (Vakkilainen, 2005)

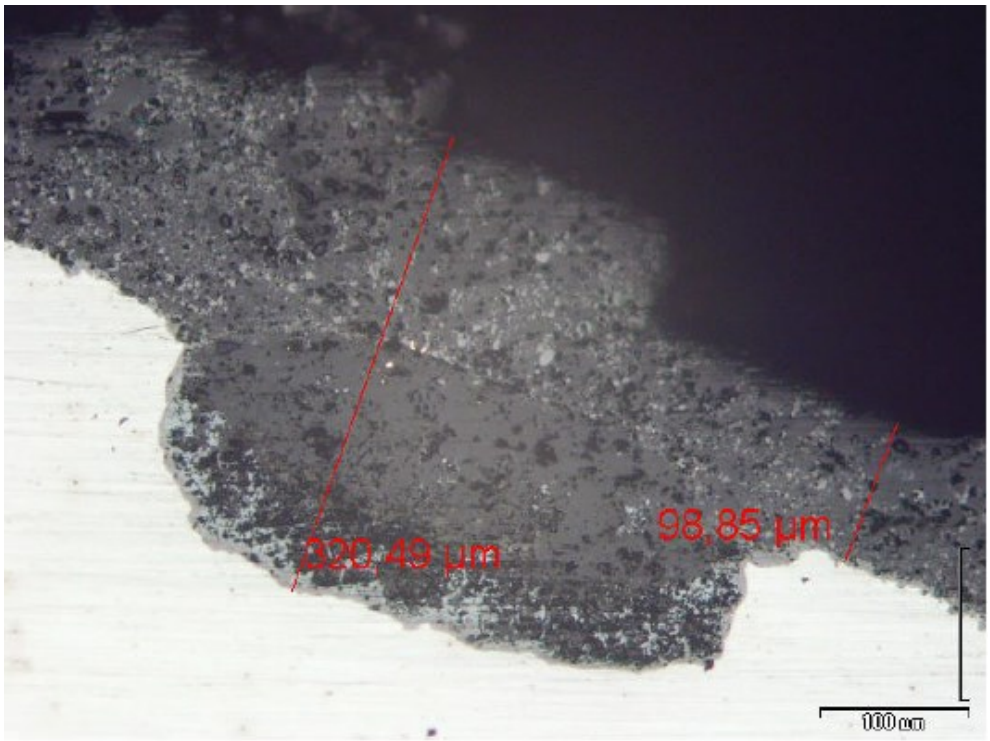

Figure 31. Magnetite layer and corroded pit (internal report from Karjunen, 2009).

Water/steam side tube corrosion prevention is achieved by forming a protective magnetite layer inside the wall tube. In normal operating pH, carbon steel reacts with water to form a thin and tenacious Fe_3O_4 (Equation 41) film on boiler tube, which protects the steel against normal attacks. Protective Fe_3O_4 layers are formed on both outside and inside surfaces. Waterside corrosion occurs inside boiler tubes and is caused by feedwater impurities and extreme pH. (Vakkilainen, 2005) Figure 31 shows magnetite layer and corroded pit.

$$3Fe + 4H_2O \rightarrow Fe_3O_4 + 4H_2 \quad (41)$$

Oxygen corrosion causes pitting inside tube surface and rupture can happen with relatively low metal losses. It is important to remove oxygen from water using deaerator or chemicals, as small amount of dissolved oxygen can cause severe damage. Oxygen is extremely corrosive in hot water environment and causes damage especially in locations where water temperature rises rapidly, such as feedwater heaters and economizers. During maintenance, stagnant water might cause oxygen corrosion in water/air interface and it is prevented with nitrogen gas. (Vakkilainen, 2005)

Stainless steel alloys are relatively immune to attack by gases such as O_2 and CO_2. Carbon steel corrosion accelerates greatly above 330 ^oC (Bartholomew, n.d).

In high pressure boiler, water pH should be maintained above 8.5 to control acid corrosion. Acid corrosion occurs when feedwater pH is too low, and it causes general wastage of metals inside tubes unlike localized oxidized corrosion. If pH is lower than 4.5, Fe_3O_4 film is loosened from tubes and could result blockage of tubes. High pressure boilers are more susceptible to caustic attack compared to acidic attack. Caustic corrosion occurs when pH is too high, and it causes removal of Fe_3O_4 layer that protects carbon steel. Fe_3O_4 film dissolves forming complex caustic-ferritic compounds. Carbon steel reforms Fe_3O_4 layer which dissolves again by the caustic, and this continues as long as concentrated caustic exists. Caustic gouging results metal losses in irregular patterns inside boiler tubes and is accompanied by Na_2CO_3 residues and crystallized NaOH. Feedwater is subject of extreme pH swings because of minor changes in acid or alkali concentrations, so swings are reduced by buffering chemicals such as phosphate. (Vakkilainen, 2005) Figure 32 shows deposit and heat effect inside tube surfaces.

Figure 32. Tube insides after deposits were removed. Cold side (top) is smooth and has minor pitting. Hot side (bottom) has rough irregularities (internal report from Jörgensen, 2018)

Flow assisted corrosion (FAC) occurs in turbulent areas where water velocity is high and tube flow changes directions such as bends, orifices and headers. CR due to FAC is high between 100-250 °C and when pH is low (Vakkilainen, 2005). Very low dissolved oxygen level, excessive velocity and excessive feed of oxygen can lead to FAC of carbon steel feedwater lines (Bartholomew, n.d). Hydrogen attacks cause damage to boiler tubes as they reduce metal strength, and it cannot be detected visually as it leaves no marks (Vakkilainen, 2005).

When researchers want to compare how aggressive a corrosive environment is or how resistant different alloys are they often resort to simplified, high-temperature laboratory tests such as ash embedding or ash coating. These bench-scale methods isolate only a subset of the variables present in service, allowing rapid, side-by-side ranking of materials. While invaluable for short-term screening, the conditions they create are milder and less complex than those in full-scale equipment, so the resulting data cannot be extrapolated reliably to predict long-term service life or exact in-plant CRs. Factors that are difficult to reproduce in laboratories include various fluctuations such as the temperature and chemical composition of combustion gas and heat transfer rates and temperature gradients in KRBs and heat exchangers. (Kawahara, 2006)

Keeping boiler tubes internal surfaces clean from internal deposits prevents fireside and waterside corrosion. Water quality control is the most important part of keeping tube internal deposits thin. Internal deposits consist of contaminating elements present in makeup water, drifting metal oxides, contaminants from the plant and solids present in condenser leakage. High-pressure boilers with high makeup are prone to form internal deposits. Insufficient removal of calcium bicarbonate ($Ca(HCO_3)_2$) from the makeup water will decompose forming CaCO3 (Equation 42). CaCO3 has limited solubility which causes it to agglomerate at the heated surfaces. Internal deposits have a low thermal conductivity, and even thin layers can cause significant tube temperature increase, overheating and fireside corrosion. (Vakkilainen, 2005)

$$Ca(HCO_3)_2 \rightarrow CaCO_3 + CO_2 + H_2O \quad (42)$$

Carbon steel tube with heavy internal deposits in lower furnace will experience severe fireside corrosion and failure well before they will experience overheating failure. While composite tubes may require much higher temperature before experiencing overheating and fireside corrosion, upper furnace still contains mostly easily corroding carbon steel. Usually, most deposits can be found in around primary and secondary air ports. They can also be found further up in wall tubes, sloped roof, nose, screen, floor tubes, and in tubes in the generation bank (Figure 33). (Bartholomew, n.d)

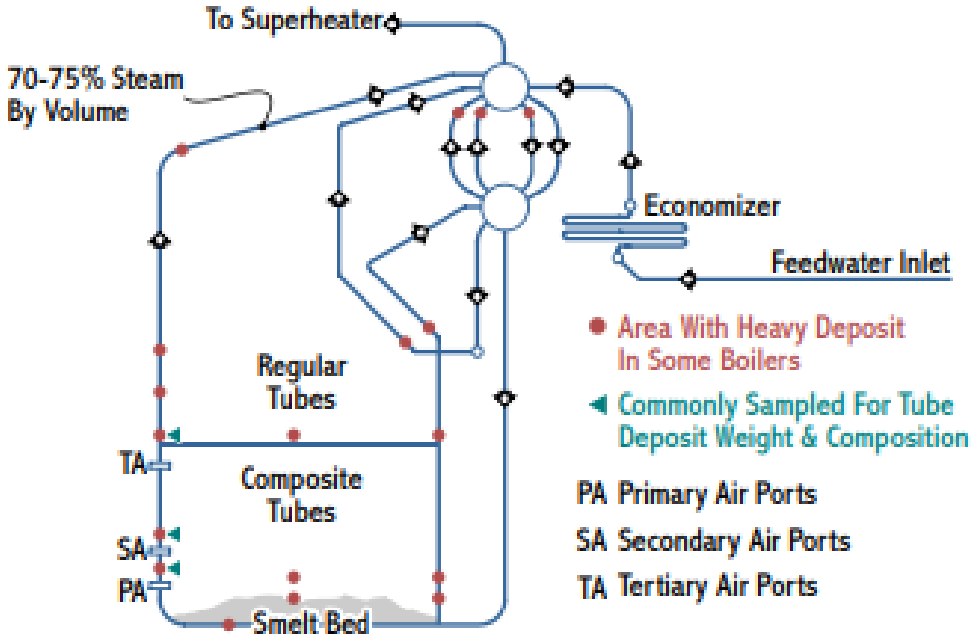

Figure 33. Typical locations of thick internal deposits in KRBs (Bartholomew, n.d.).

Tube internal deposits with porosities between 30-50% have thermal conductivity of 1.2-2.5 W/mK but experiments show they can be as low as 0.8-1.4 W/mK (Dooley, 2003). $CaCO_3$ thermal conductivity is 0.9 W/mK at room temperature (Dillon et al., 2011). Internal deposit thermal conductivity can be as low as 0.3 W/mK (Tavares & Karjunen, 2020).

Figure 34. Internal deposits inside a boiler tube (internal report form Isberg, 2018).

Internal deposits can lead to tube rupture, severe leaks and potential smelt-water explosions, which might cause irreversible damage to the furnace. Internal deposit composition and growth depend on boiler water quality and local heat flux. Corrosion on the waterside can be dangerous, as it is usually localized and therefore difficult to detect. Tube wall and cladding thicknesses are relatively easy to confirm with non-destructive testing (NDT). Deposit thicknesses as low as 20 µm can be measured using ultrasonic techniques. In NDT ultrasonic method, thicknesses can be measured and deducted with pulse travelling time. (Tavares & Karjunen, 2020)

According to Varo, internal deposits can be measured ultrasonically across the range of 0–300 µm with an accuracy of ±25 µm. This is sufficient in typical KRBs, since internal deposits thicknesses that affect cladding performance are usually around 100–150 µm. In very high-pressure units, corrosion tolerance for internal deposits is low as tens of µm, but these are a small minority of KRBs. In high-pressure KRBs, corrosion is primarily driven by the high pressure itself, hence the use of Sanicro 38, as is standard practice in new installations. Figure 35 shows correlation between wall and internal scale thickness and height.

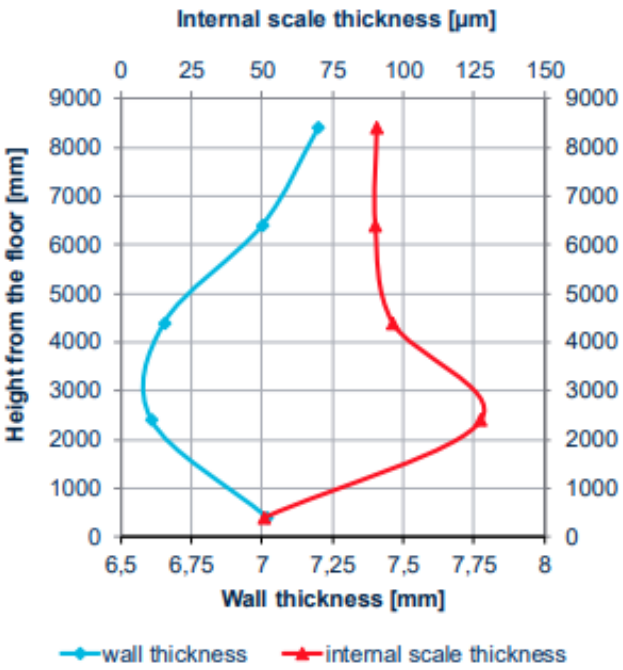

Figure 35. Internal deposit and wall thicknesses related to height (Tavares & Karjunen, 2020).

Internal deposits and tube cladding and carbon steel quality control relies on tube sampling where tubes are removed, cut, polished and visually observed. The problem is the small number of samples, which are taken during shutdown and don't represent boiler tube conditions accurately, as deposit formations are localized. In most cases, samples aren't taken close to critical areas, such as between primary and secondary air ports, because additional welds weaken furnace wall integrity and interfaces outside boiler makes sampling difficult. (Tavares & Karjunen, 2020)

According to Swedish Recovery Boiler Committee allowed maximum internal deposit thickness is 150 µm when steam drum pressure doesn't exceed 85 bar and internal deposits composition is within recommended limits. Deposits are removed with chemical acid cleaning. Acid cleaning timing is done based on varying reasons as in some cases acid cleaning cycle is based on NDT and tube samples deposit data but in some cases it is done in relatively short intervals regardless of tube sampling results. Time based acid cleaning cycles are problematic as thick deposits might be formed locally between cycles causing internal and external corrosion or on the other hand lead to extra expenses and mill outages when unnecessary acid cleaning are done. (Tavares & Karjunen, 2020)

Chemical cleaning solvent usually contains hydrochloric acid, ammonium bifluoride, copper complexor and inhibitor and is followed by rinses and neutralization with soda ash (Bartholomew, n.d.).

4 Calculation model and methods

In this chapter, the structure and purpose of the developed calculation model are presented. The model is designed to predict how internal deposits accumulating on the inner surfaces of water/steam wall tubes in kraft recovery boilers impact the thermal behaviour of the boiler tubes, particularly the temperature of the tube cladding materials, such as AISI 304 and Sanicro 38. The fundamental motivation for developing this calculation model stems from the limitations of current evaluation methods. While NDT and tube sampling can accurately measure internal deposit thickness, they fail to reliably predict how these deposits will affect tube integrity during continued operation. This uncertainty arises because there is no method available to forecast the future corrosion rate of the cladding.

Boiler tubes and cladding materials, especially Sanicro 38, are designed to endure in volatile and corrosive environments when cladding temperatures remain within their intended limits. Internal deposits work as an insulator, reducing tube total thermal conductivity, resulting carbon steel and cladding temperature increase especially on high internal deposit locations. In result, cladding that would normally endure the corrosive environment, corrodes with intensive rate that might end up resulting in tube failure. A sudden failure of this nature may result in a smelt water explosion, potentially rendering the entire KRB unusable and posing serious safety risks, including injury and loss of life.

Of particular concern is that CR increases sharply in AISI 304 when surface temperatures surpass recommended values. While Sanicro 38 offers better resistance, it too experiences accelerated corrosion at elevated temperatures. Because Sanicro 38 costs substantially more than AISI 304 stainless steels, cladding every furnace surface with it is not economically feasible.

The main purpose of the calculation model is to create a flexible and broadly applicable framework that can be adapted to different KRB configurations. The model predicts how internal deposits affect cladding surface temperature and estimates corrosion progression for both AISI 304 and Sanicro 38 at a specified vertical location within the furnace. The calculation of CR is based on sulfidation, which makes it more accurate at furnace lower levels where H_2S is present and CRs in wall tubes are highest.

Calculation model is structured into five sequential steps, each representing a critical aspect of the thermal system. Section 4.1 estimates the total heat production related to boiler properties. It takes into account the boiler's physical dimensions, daily boiler load, and the higher heating value (HHV) of the black liquor and calculates heat flux. Section 4.2 determines the

temperature of the internal deposit/magnetite layer on the wall tube, using parameters such as steam drum pressure, saturated water velocity and water/steam mixture liquid-vapor ratio, and the local heat flux calculated in the previous phase. Section 4.3 simulates heat conduction across the multilayer structure from furnace to water/steam mixture. It evaluates how layer thicknesses and thermal conductivities of deposits, carbon steel and cladding materials affect the final temperatures of AISI 304 and Sanicro 38 on the surface facing the furnace. Section 4.4 links the calculated cladding surface temperature to CR predictions for AISI 304 and Sanicro 38. Section 4.5 provides a basis to estimate local heat flux related to furnace height position. Section 4.6 provides a correlation between internal deposit thickness, cladding surface temperature, and cladding CR.

Beyond CR estimation, the calculation model provides valuable insight for decision making regarding material selection and boiler maintenance. The results can support the choice of cladding material in different furnace areas, considering site-specific factors such as boiler water purity levels. Additionally, when the average deposit growth rate is known, boiler operators could estimate when chemical acid cleaning should be scheduled to prevent accelerated corrosion and maintain safe operating conditions.

4.1 Furnace heat production and heat flux

First step in the calculation model is to create correlation between average heat flux (q_a) and floor loading (HHRR). Input parameters are furnace width (l_w), furnace depth (l_d), black liquor higher heating value (HHV) and DS firing rate ($\dot{m}$DS). Total heat input of the furnace is calculated using Equation (43)

$$Q_{tot} = \dot{m}DS \times HHV \tag{43}$$

where Q_{tot} is total heat input (MW), $\dot{m}$DS is DS firing rate (kgDS/s) and HHV is black liquor higher heating value (MJ/kgDS) (Vakkilainen, 2005). Furnace floor area is calculated using Equation (44)

$$A_f = l_w l_d \tag{44}$$

where A_f is floor area (m^2), l_w is furnace width (m) and l_d is furnace depth (m) (Vakkilainen, 2005). Floor loading is calculated using Equation (45)

$$HHRR = \frac{Q_{tot}}{A_f} \tag{45}$$

where HHRR is floor loading (MW/m^2), Q_{tot} is total heat input (MW) and A_f is floor area (m^2) (Vakkilainen, 2005).

The correlation between floor loading (HHRR) and maximum heat flux (q_m) was created using internal research data from Valmet (Viswamoorthy, 2021). Valmet provided data of different KRB floor loading in relation to maximum heat flux (Table 11). Same data provided information that the maximum heat flux multiplier was estimated to be 160%. (Figure 12 from Section 3.3). Average heat flux (q_a) values were calculated by dividing the maximum heat flux by 1.6 (Table 11). Functions were created from given data (Figure 36).

Table 11. Heat flux related to floor loading (adapted from internal data from Viswamoorthy, 2021).

Floor loading (HHRR)	Heat flux max (q_m)	Heat flux average (q_a)
(MW/m²)	(kW/m²)	(kW/m²)
3.0	140	87.500
3.3	160	100.000
3.5	166	103.750
3.8	180	112.500

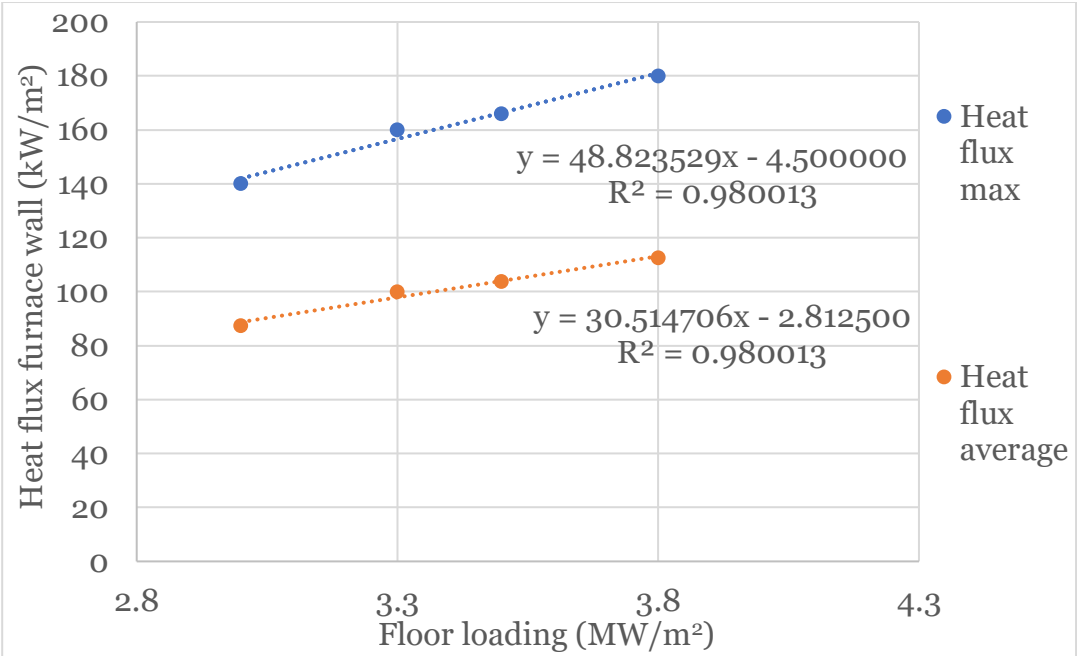

Figure 36. Maximum and average heat flux as a function of floor loading.

Average heat flux is calculated using Equation (46)

$$y = 30.514706x - 2.812500 \quad (46)$$

where y is average heat flux (q_a) (kW/m²) and x is floor loading (HHRR) (MW/m²). Maximum heat flux is calculated using Equation (47)

$$y = 48.823529x - 4.500000 \quad (47)$$

where y is maximum heat flux (q_m) (kW/m²) and x is floor loading (HHRR) (MW/m²). Vertically located and observed heat flux is calculated using Equation (48)

$$q_l = k_l q_a \quad (48)$$

where q_l is heat flux in observed location (W/m²), k_l is heat flux multiplier based on height location in the furnace (%), and q_a is average heat flux (W/m²).

4.2 Water properties in water/steam tubes

In this section, the focus shifts to simulating water-side heat transfer and calculating the temperature of the deposit surface facing the water/steam mixture inside the wall tube. Input parameters are tube outside diameter (D_{to}), total wall thickness (x_t), steam drum pressure (P) and optionally drum saturated water velocity (u_l) and water/steam mixture liquid-vapor ratio (v-%). Tube inside diameter is calculated using Equation (49)

$$D_{ti} = D_{to} - 2x_t \quad (49)$$

where D_{ti} is tube inside diameter (m), D_{to} is tube outside diameter (m) and x_t is total wall thickness (m). The tube inside area is calculated using Equation (50)

$$A_{ti} = \frac{\pi {D_{ti}}^2}{4} \quad (50)$$

where A_{ti} is tube inside area (m²) and D_{ti} is tube inside diameter (m). Calculation model retrieves the corresponding thermodynamical properties including water/steam mixture density (ρ), dynamic viscosity (μ), specific heat capacity (c), thermal conductivity (k) and temperature (T) from a built-in database (Appendix 2) depending on steam drum pressure (P) and water/steam mixture liquid-vapor ratio (v-%). Using these parameters, the model calculates the mass flow of liquid water ($\dot{m}_l$), water/steam mixture velocity inside wall tube (u_w), Reynolds number (Re), Prandtl number (Pr), Nusselt number (Nu), convective heat transfer coefficient (h) and finally temperature of deposit surface facing water (T_{wd}). To estimate the velocity of water/steam mixture inside the wall tubes, the model first calculates the mass flow rate

assuming that water flow is 100% liquid. Mass flow of liquid water is calculated using Equation (51)

$$\dot{m}_l = u_l A_{ti} \rho_l \tag{51}$$

where $\dot{m}_l$ is mass flow of saturated 100% liquid water (kg/s), u_l is velocity of saturated 100% liquid water (m/s), A_{ti} is tube inside area (m^2) and ρ_l is density of saturated 100% liquid water (kg/m^3) (NASA, n.d.). Water/steam mixture velocity inside the wall tubes is calculated using Equation (52)

$$u_w = \frac{\dot{m}_l}{\rho_w A_{ti}} \tag{52}$$

where u_w is velocity of water/steam mixture (m/s), $\dot{m}_l$ is mass flow of saturated 100% liquid water (kg/s), ρ_w is density of water/steam mixture (kg/m^3) and A_{ti} is tube inside area (m^2) (NASA, n.d.). Reynolds number is calculated using Equation (53)

$$Re = \frac{\rho_w u_w D_{ti}}{\mu_w} \tag{53}$$

where Re is Reynolds number, ρ_w is density of water/steam mixture (kg/m^3), u_w is velocity of water/steam mixture (m/s), D_{ti} is tube inside diameter (m) and μ_w is dynamic viscosity of water/steam mixture (Pa·s) (Lienhard, 2024). Prandtl number is calculated using Equation (54)

$$Pr = \frac{c_w \mu_w}{k_w} \tag{54}$$

where Pr is Prandtl number, c_w is specific heat capacity of water/steam mixture (J/kgK), μ_w is dynamic viscosity of water/steam mixture (Pa·s) and k_w is thermal conductivity of water/steam mixture (W/mK) (Bergman et al., 2011). Nusselt number is calculated using Dittus-Boelter equation for turbulent flow when the fluid is being heated, as seen in Equation (55)

$$Nu = 0{,}023 Re^{0,8} Pr^{0,4} \tag{55}$$

where Nu is Nusselt number, Re is Reynolds number and Pr is Prandtl number (Winterton, 1998). The heat transfer coefficient is calculated using Equation (56)

$$h = Nu \frac{k_w}{D_{ti}} \tag{56}$$

where h is the heat transfer coefficient (W/m^2K), Nu is the Nusselt number, k_w is the thermal conductivity of water/steam mixture (W/mK) and D_{ti} is the tube inside diameter (m) (Bergman et al., 2011). Finally, the temperature of deposit surface facing water is calculated using Equation (57)

$$T_{wd} = \frac{q_l}{h} + T_w \tag{57}$$

where T_{wd} is temperature of deposit surface facing water (^oC), q_l is heat flux in observed location (W/m^2), h is heat transfer coefficient (W/m^2K) and T_w is temperature of water/steam mixture (^oC) (Kurganov, 2011). The temperature of the deposit surface facing the water is a critical input for determining temperature distribution through the tube wall and cladding layers.

The calculation model is capable of accounting for varying liquid-vapor ratios, however, its construction and the majority of simulations were performed assuming a 100% liquid phase. This assumption was necessary due to the lack of detailed research on how water/steam phase transformation progresses along the wall tube height. In the lower furnace, the fluid is presumed to be predominantly in the liquid phase, as steam generation is only beginning to be influenced by increasing heat flux. Consequently, all temperature and corrosion extrapolations within the model are based on the assumption of fully liquid internal flow conditions.

4.3 Heat transfer and thermal conductivity within layers

In this section, the model calculates how heat is transferred through multiple material layers within the KRB water/steam wall tube system as a linear vector. These layers include, in order from the water side to the furnace side internal deposit or magnetite layer, carbon steel, cladding (either AISI 304 or Sanicro 38), and finally the outer smelt (deposit) layer. Interface between water and internal deposit is called deposit surface facing water, interface between internal deposit and carbon steel is called deposit-carbon steel interface, interface between carbon steel and cladding is called carbon steel-cladding interface, interface between cladding and smelt is called cladding surface facing furnace and interface between smelt and furnace gases is smelt surface facing furnace (Figure 37). Fourier's law of heat conduction is used to calculate temperatures between interfaces (Ansys, 2020).

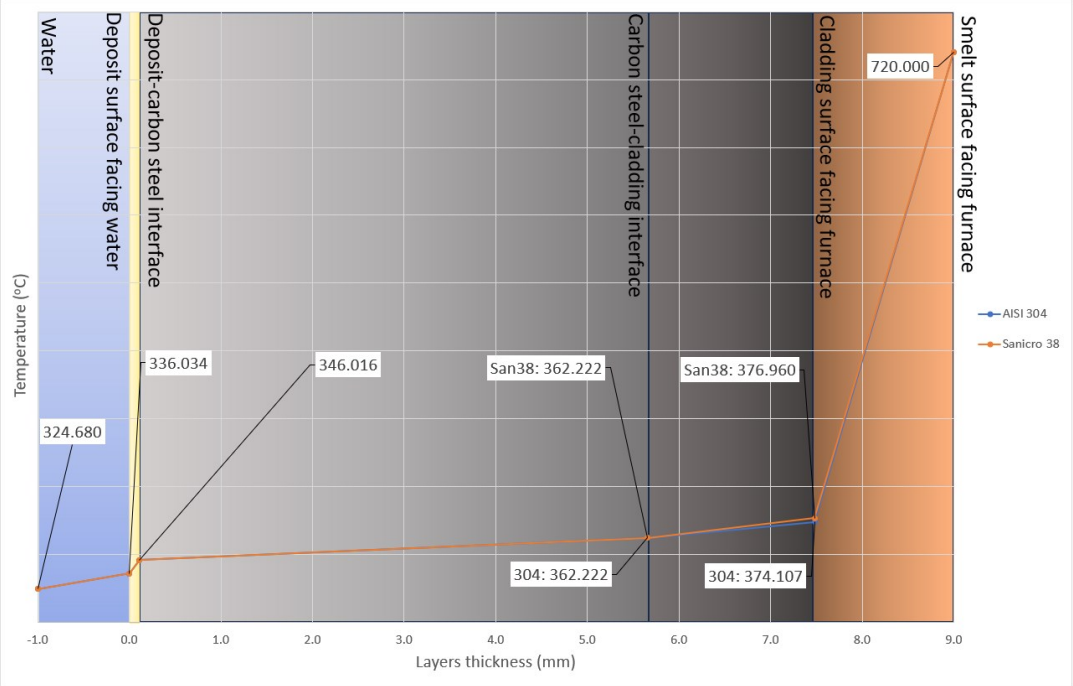

Figure 37. Visualization of thermal layers from water/steam side to furnace side.

Input parameters are cladding thickness (x_{cl}) for AISI 304 and Sanicro 38, thermal conductivity of internal deposit/magnetite (k_d), thickness of average internal deposits (x_d) and optionally smelt melting temperature (T_s) and smelt thermal conductivity (k_s). While the thermal conductivities of carbon steel, AISI 304, and Sanicro 38 can be entered manually, the model is also capable of automatically estimating these values based on the local temperature in each layer, using temperature-dependent material property functions. This layered approach enables the model to simulate realistic thermal gradients across the tube wall structure, providing accurate predictions of the furnace-facing surface temperature of the cladding, which is critical for corrosion assessment in the following section. Temperature of deposit-carbon steel interface is calculated using Equation (58)

$$T_{dc} = q_l \frac{x_d}{k_d} + T_{wd} \tag{58}$$

where T_{dc} is temperature of deposit-carbon steel interface (°C), q_l is heat flux in observed location (W/m²), x_d is thickness of average internal deposits (m), k_d is thermal conductivity of internal deposits/magnetite (W/mK) and T_{wd} is temperature of deposit surface facing water (°C). Carbon steel thickness is calculated using Equation (59)

$$x_{cs} = x_t - x_{cl} \tag{59}$$

where x_{cs} is carbon steel thickness (m), x_t is total wall thickness (m) and x_{cl} is cladding thickness (m). Carbon steel, AISI 304 and Sanicro 38 thermal conductivities as a function of temperature (Table 7 from Section 3.5) were constructed in Figure 38. This enables the calculation model to dynamically estimate the thermal conductivities of tube materials across varying temperature conditions. This approach allows for a more accurate prediction of heat transfer through each metal layer, particularly in scenarios where the temperature gradient across the tube wall is significant. All created functions regressions are close to 1 indicating a good correlation.

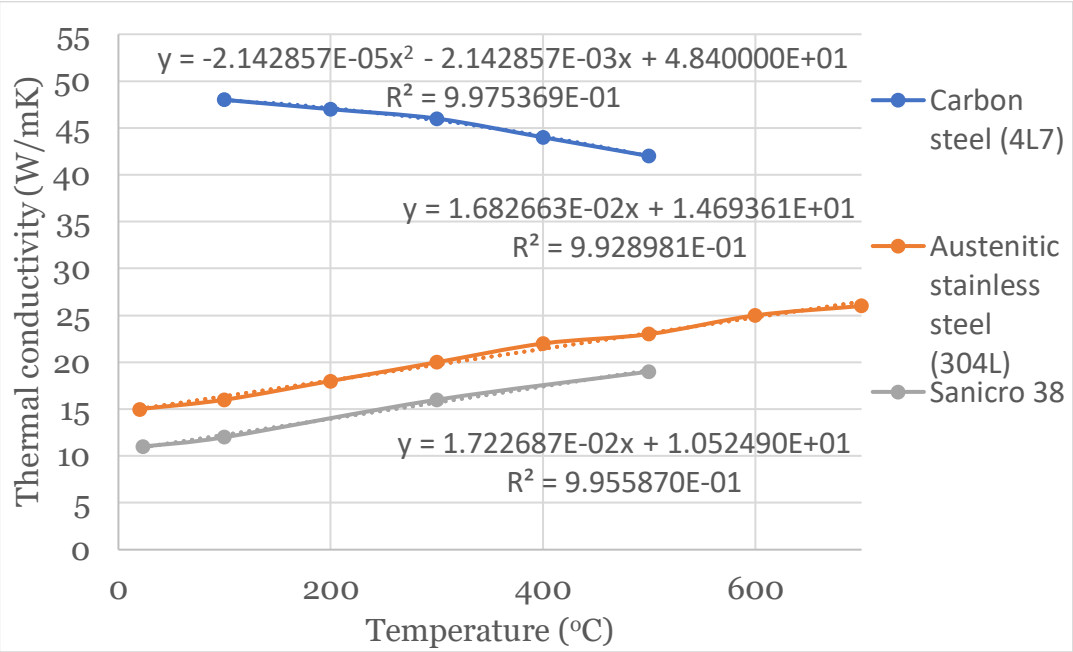

Figure 38. Materials thermal conductivities as a function of temperature.

Temperature-dependent carbon steel thermal conductivity (k_{cs}) is calculated using Equation (60)

$$y = -2.142857 \times 10^{-05}x^2 - 2.142857 \times 10^{-03}x + 48.40000 \quad (60)$$

where y is temperature-dependent carbon steel thermal conductivity (k_{cs}) (W/mK) and x is temperature of deposit-carbon steel interface (T_{dc}) (°C). Temperature of carbon steel-cladding interface is calculated using Equation (61)

$$T_{cc} = q_l \frac{x_{cs}}{k_{cs}} + T_{dc} \quad (61)$$

where T_{cc} is temperature of carbon steel-cladding interface (°C), q_l is heat flux in observed location (W/m²), x_{cs} is carbon steel thickness (m), k_{cs} is

temperature-dependent carbon steel thermal conductivity (W/mK) and T_{dc} is temperature of deposit carbon steel interface (^{o}C). Temperature-dependent AISI 304 thermal conductivity (k_{304}) is calculated using Equation (62)

$$y = 1.682663 \times 10^{-02}x + 14.69361 \quad (62)$$

where y is temperature-dependent AISI 304 thermal conductivity (k_{304}) (W/mK) and x is temperature of carbon steel-cladding interface (T_{cc}) (^{o}C). Temperature-dependent Sanicro 38 thermal conductivity (k_{38}) is calculated using Equation (63)

$$y = 1.722687 \times 10^{-02}x + 10.52490 \quad (63)$$

where y is temperature-dependent Sanicro 38 thermal conductivity (k_{38}) (W/mK) and x is temperature of carbon steel-cladding interface (T_{cc}) (^{o}C). Finally, temperatures of cladding surface facing furnace for both AISI 304 and Sanicro 38 are calculated using Equation (64)

$$T_{cf} = q_l \frac{x_{cl}}{k_{cl}} + T_{cc} \quad (64)$$

where T_{cf} is temperature of cladding surface facing furnace for either AISI 304 or Sanicro 38 (^{o}C), q_l is heat flux in observed location (W/m^2), x_{cl} is cladding thickness for either AISI 304 or Sanicro 38 (m), k_{cl} is temperature dependent cladding thermal conductivity for either AISI 304 (k_{304}) or Sanicro 38 (k_{38}) (W/mK) and T_{cc} is temperature at the carbon steel-cladding interface (^{o}C).

Once the temperature of the cladding surface facing the furnace has been determined, the model can proceed to the next phase, where corrosion behaviour of the cladding material is evaluated. On the furnace-facing side, an ash or smelt layer typically forms on the surface of the tube. If the thermal conductivity and melting point of the smelt are known, the model can estimate the thickness of the smelt layer for both AISI 304 and Sanicro 38 cladding materials. This information is crucial, as the presence and characteristics of the smelt layer might affect cladding corrosion rates. Smelt max thickness is calculated using Equation (65)

$$x_s = \frac{(T_s - T_{cf})k_S}{q_l} \quad (65)$$

where x_s is smelt max thickness (m) for either AISI 304 or Sanicro 38, T_s is smelt melting temperature (^{o}C), T_{cf} is temperature of cladding surface facing

furnace for either AISI 304 of Sanicro 38 (°C), k_s is smelt thermal conductivity (W/mK) and q_l is heat flux in observed location (W/m²).

4.4 Cladding corrosion rate as a function to temperature

This section evaluates the CR of cladding materials AISI 304 and Sanicro 38 as a function of cladding surface temperature facing the furnace. A set of temperature-corrosion data points was compiled from multiple sources (see Table 10 in Section 3.6) to construct temperature-dependent CR functions for both cladding materials. However, as illustrated in Figures 26 and 27 in Section 3.6, the literature does not present a consistent correlation between corrosion rate and temperature for these alloys. This variation arises from case-specific differences in furnace gas composition, H_2S concentrations, and other local environmental factors influencing corrosion behaviour. Laboratory conditions fail to fully replicate the complex, multireaction environment of a KRB, where fluctuating temperatures and gas chemistry complicate prediction of long-term material performance.

Among the compiled data, the most reliable point originates from internal research by VTT (Pohjanne, 2013), which measured CR values of 0.6 mm/y for AISI 304 and 0.07 mm/y for Sanicro 38 at a cladding surface temperature of 440 °C under representative KRB furnace conditions. This data point serves as the anchor for the polynomial correlation of both alloys. Further CR measurements were provided from field cases Boiler 1 (Khodahami, 2024), Boiler 2 (Kiwa, 2014) and Boiler 3 (Liikola, 2015). While annual CR were measured, precise local wall temperatures were not provided. Therefore, it was assumed that maximum CR occurred at regions of highest heat flux. Using boiler-specific parameters and applying the developed heat transfer model, cladding surface temperatures corresponding to the maximum heat flux (160% multiplier) were extrapolated and linked to the measured CR values (Table 12). White-marked values in Table 12 were selected for curve fitting.

Boilers 1 and 2 provided relatively accurate CR estimates, as average internal deposit thicknesses were low (~20 μm), minimizing the impact of insulating effects and allowing the calculated cladding temperatures to be predominantly governed by steam drum pressure and local heat flux. However, the CR data point for AISI 304 from Boiler 2 was excluded from the model (greyed in Table 12) due to inconsistency. Although the CR values from Boilers 1 and 2 were nearly identical (0.059 mm/y and 0.057 mm/y, respectively), they corresponded to a 10 °C temperature difference, which would have undermined the reliability of the regression curve. Boiler 1 was selected as the more valuable data source due to its stratified corrosion data across

different furnace heights, which was used at vertical heat flux distribution developed in Section 4.5.

Table 12. Extrapolated temperatures connected to CR for cladding materials.

Term	Symbol	Unit	Boiler 1 (Khodahami, 2024)		Boiler 2 (Kiwa, 2014)		Boiler 3 (Liikola, 2015)	
			Measured	Calculated	Measured	Calculated	Measured	Calculated
Furnace height from the primary air port to nose upper edge	l_h	(m)	37.90		28.67		10.823	
Furnace width	l_w	(m)	13.53		10.04		4.1902	
Furnace depth	l_d	(m)	15.03		11.44		4.9522	
Steam drum pressure	P	(bar)	120.00		119.00		92	
Higher heating value	HHV	(MJ/kgDS)	12.62		12.65		13	
Boiler load / DS firing rate	$\dot{m}DS$	(tDS/day)	5000.00		2400.00		250	
Tube outside diameter	D_{to}	(mm)	63.50		63.50		60.3	
Total wall thickness	x_t	(mm)	6.53		6.53		5.3	
Cladding thickness 304	x_{cl}	(mm)	1.65		1.65		1.65	
Cladding thickness Sanicro 38	x_{cl}	(mm)	1.65		1.65		1.65	
Thermal conductivity deposits	k_d	(W/mK)	0.30		0.30		0.3	
Average deposit thickness	x_d	(µm)	20.00		20.00		1180	
Heat flux multiplier	k_m	(%)	160.00 %					
AISI 304 temperature cladding surface facing furnace	T_{cf}	(°C)	High	381.059	High	371.880	High	655.143
AISI 304 corrosion rate	CR	(mm/y)	0.059	0.059	0.057	0.000	2	2.000
Sanicro 38 temperature cladding surface facing furnace	T_{cf}	(°C)		384.282	High	374.650		656.117
Sanicro 38 corrosion rate	CR	(mm/y)		0.003	0	0.000		1.108

In contrast, Boiler 3 presented a markedly different case, with internal deposit thicknesses reaching 1180 µm and a measured CR of 2.0 mm/y. The extrapolated cladding surface temperature of 655.1 °C was the most uncertain, due to high variability in deposit thermal conductivity (assumed around 0.3 W/mK), unknown internal deposit composition, and potential

measurement error on-site. Therefore, this point was treated cautiously in curve fitting.

To construct a second-order polynomial curve for Sanicro 38, a third data point was selected close to literature (see Table 10 in Section 3.6), complementing the VTT measurement and Boiler 2 data. The chosen CR points were gathered in Table 13 and the final CR functions were plotted in Figure 39: the red curve represents AISI 304, the green curve Sanicro 38, and the grey curves correspond to corrosion trends from the literature. These fitted functions provide the basis for subsequent predictions of temperature-dependent corrosion across different boiler operating conditions.

Table 13. Corrosion data chosen to create CR function related to temperature.

Source	304 temperature	304 CR	Sanicro 38 temperature	Sanicro 38 CR
	(°C)	(mm/y)	(°C)	(mm/y)
(Kiwa, 2014)			374.650	0.000
(Khodahami, 2024)	381.059	0.059		
(Pohjanne, 2013)	440.000	0.600	440.000	0.070
Chosen point			490.000	0.200
(Liikola, 2015)	655.143	2.000		

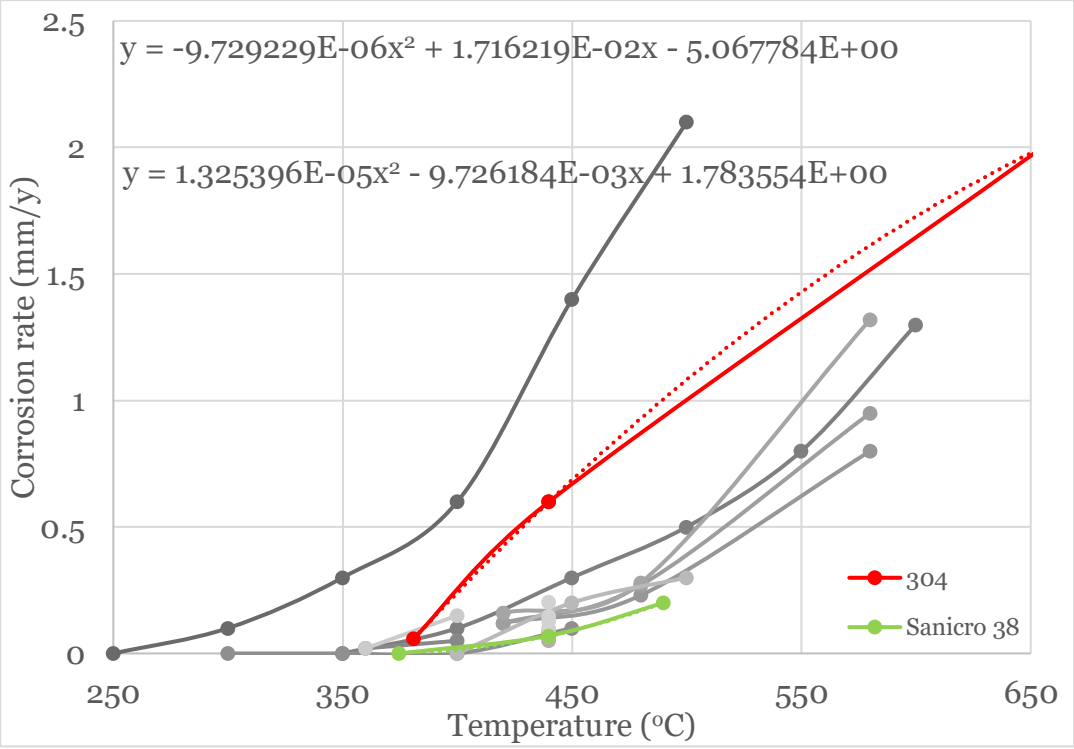

Figure 39. AISI 304 and Sanicro 38 CR as a function of temperature.

CR as a function of temperature for AISI 304 is calculated using Equation (66)

$$y = -9.729229 \times 10^{-06}x^2 + 1.716219 \times 10^{-02}x - 5.067784 \quad (66)$$

where y is corrosion rate related to temperature for AISI 304 cladding (CR) (mm/y) and x is temperature of cladding surface facing furnace (T_{cf}) (^oC). CR as a function of temperature for Sanicro 38 cladding (CR) is calculated using Equation (67)

$$y = 1.325396 \times 10^{-05}x^2 - 9.726184 \times 10^{-03}x + 1.783554 \quad (67)$$

where y is corrosion rate related to temperature for Sanicro 38 cladding (CR) (mm/y) and x is temperature of cladding surface facing furnace (T_{cf}) (^oC).

4.5 Heat flux related to height

In this section target is to estimate heat flux multiplier relation to vertical location within the furnace. Valmet internal research provided data (Figure 12 in Section 3.3) that provides information of heat flux multipliers related to height. Heat flux maximum value of 160% was measured around 22% of furnace height from furnace floor to nose arch upper edge. KRBs dimensions have been measured visually from KRB blueprints provided by boiler operators and presented in Table 14. KRB component's vertical height percentages related to height from furnace floor to nose arch upper edge are presented in Table 15.

Table 14. Measured furnace heights based on blueprints from KRBs around Finland and Sweden.

Height location (mm)	Boiler 1	Boiler 2	Boiler 3	Boiler 4	Boiler 5	Boiler 6	Boiler 7	Boiler 8
Nose arch upper edge	83400	139620	95000	34327	88725	45043	48025	47530
Tertiary air port	58100	121000	87650	15827	66448	17155	19715	26766
Black liquor guns	52600	117500	86700	12927	63298	14055	16100	23566
Top secondary air port	48800	113950	85200	8827	58698	9155	10675	19166
Bottom secondary air port	47100	112550	84590	7127	57698	8155	9988	18166
Primary air port	45500	110950	84557	5827	55798	6155	7996	16166
Furnace floor	44600	110100	83700	4827	54556	5054	6822	15055

Table 15. Relative height percentages of each component related to total height from furnace floor to nose arch upper edge.

Location	Boiler 1	Boiler 2	Boiler 3	Boiler 4	Boiler 5	Boiler 6	Boiler 7	Boiler 8	Aver-age
Nose arch upper edge	100.00 %								
Tertiary air port	34.79 %	36.92 %	34.96 %	37.29 %	34.80 %	30.26 %	31.29 %	36.06 %	34.55 %
Black liquor guns	20.62 %	25.07 %	26.55 %	27.46 %	25.58 %	22.51 %	22.52 %	26.21 %	24.56 %
Top secondary air port	10.82 %	13.04 %	13.27 %	13.56 %	12.12 %	10.26 %	9.35 %	12.66 %	11.89 %
Bottom second-ary air port	6.44 %	8.30 %	7.88 %	7.80 %	9.20 %	7.75 %	7.68 %	9.58 %	8.08 %
Primary air port	2.32 %	2.88 %	7.58 %	3.39 %	3.63 %	2.75 %	2.85 %	3.42 %	3.60 %
Furnace floor	0.00 %								

As can be observed from Table 15, components have height percentage differences. Heat flux multiplier related to height percentage in Figure 12 in Section 3.3 is misrepresenting as highest heat flux curve location varies depending on KRB size. For example, maximum heat flux multiplier value at 22% height would in some cases end up either below, close or above the black liquor guns depending on furnace size. It is also established that the highest CR occurs around primary and secondary air port, so primary air port would make more sense as a reference point. Additionally, this approach improves the model's adaptability to various KRB furnace designs, as the distance from the furnace floor to the primary air port is relatively same around 1 meter but percentage distances can vary significantly between the KRB types. KRB component's vertical locations related to primary air port are presented in Table 16. KRBs component's vertical height percentages related to height from primary air port to nose arch upper edge are presented in Table 17.

Table 16. Measured furnace widths and depths and component vertical positions related to primary air port.

Height location (m)	Boiler 1	Boiler 2	Boiler 3	Boiler 4	Boiler 5	Boiler 6	Boiler 7	Boiler 8
Width	13.526	10.038	4.190	11.582	11.810	11.811	16.382	9.524
Depth	15.028	11.440	4.952	12.040	11.811	12.573	17.906	11.810
Nose arch upper edge	37.900	28.670	10.443	28.500	32.927	38.888	40.029	31.364
Tertiary air port	12.600	10.050	3.093	10.000	10.650	11.000	11.719	10.600
Black liquor guns	7.100	6.550	2.143	7.100	7.500	7.900	8.104	7.400
Top secondary air port	3.300	3.000	0.643	3.000	2.900	3.000	2.680	3.000
Bottom secondary air port	1.600	1.600	0.033	1.300	1.900	2.000	1.992	2.000
Primary air port	0.000							
Furnace floor	-0.900	-0.850	-0.857	-1.000	-1.242	-1.101	-1.174	-1.111

Table 17. Relative height percentages of each component related to total height from the primary air port to nose arch upper edge.

Location	Boiler 1	Boiler 2	Boiler 3	Boiler 4	Boiler 5	Boiler 6	Boiler 7	Boiler 8	Average
Nose arch upper edge	100.00 %								
Tertiary air port	33.25 %	35.05 %	29.62 %	35.09 %	32.34 %	28.29 %	29.28 %	33.80 %	32.09 %
Black liquor guns	18.73 %	22.85 %	20.52 %	24.91 %	22.78 %	20.31 %	20.25 %	23.59 %	21.74 %
Top secondary air port	8.71 %	10.46 %	6.16 %	10.53 %	8.81 %	7.71 %	6.69 %	9.57 %	8.58 %
Bottom secondary air port	4.22 %	5.58 %	0.32 %	4.56 %	5.77 %	5.14 %	4.98 %	6.38 %	4.62 %
Primary air port	0.00 %								
Furnace floor	-2.37 %	-2.96 %	-8.21 %	-3.51 %	-3.77 %	-2.83 %	-2.93 %	-3.54 %	-3.77 %

A vertical heat flux curve was created by mirroring and adjusting calculation model simulation results to Boiler 1 (Khodahami, 2024) internal corrosion data in different locations. Boiler 1 operator provided back wall tube inspection data covering changes of AISI 304 cladding thickness across 192 tubes between 2023 and 2024 at six different height Pos 1-6 (Figure 40). The dataset includes height-specific corrosion information, detailed in Appendices 3–8. To isolate actual material loss, only negative thickness changes were considered. Positive changes, which may result from measurement uncertainties or surface buildup, were excluded and filtered data can be observed in Appendix 9. The average AISI 304 measured cladding losses at each

vertical position Pos 1-6 is presented in Table 18, providing an empirical baseline to support and validate the modelled vertical heat flux distribution. In Table 18 height and height-% for Pos 1-6 were adjusted from Figure 40 to be related to primary air port instead of furnace floor.

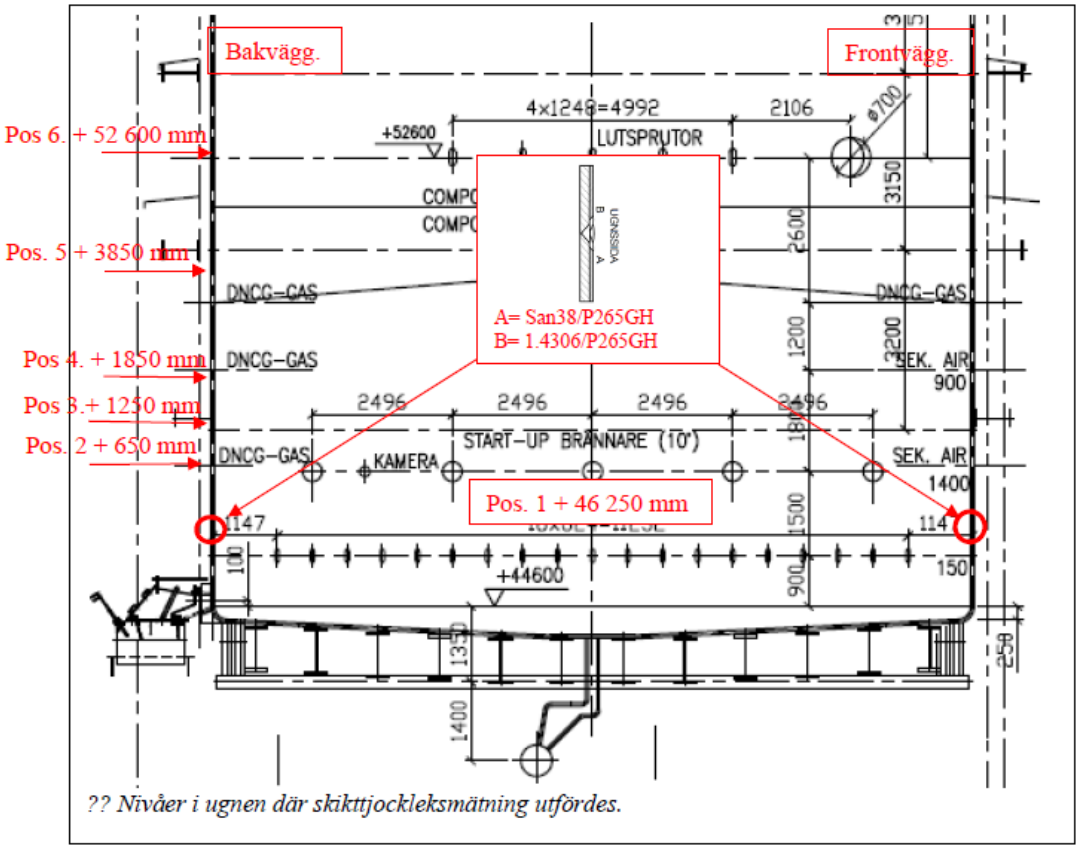

Figure 40. Boiler 1 Pos 1-6 vertical locations (internal document from Khodahami, 2024).

Table 18. Boiler 1 Pos 1-6 measured CRs and calculated CRs.

Location	Height	Height-%	Measured CR	Calculated CR
	(m)	(%)	(mm/y)	(mm/y)
Pos 1	0.750	1.98	0.058	0.059
Pos 2	1.400	3.69	0.059	0.058
Pos 3	2.000	5.28	0.041	0.056
Pos 4	2.600	6.86	0.047	0.053
Pos 5	4.600	12.14	0.030	0.039
Pos 6	7.100	18.73	0.026	0.017

The measured CR results, summarized in Table 18, indicate that Pos 2 experiences the most significant material loss, suggesting it is the location of highest local heat flux. Calculated CRs are calculated by using Boiler 1 parameters

(Table 12) and using different heat flux multiplier values providing basis for vertical heat flux curve locations. Maximum heat flux multiplier 160% was placed between 0-3% related to total height from primary air port to nose arch upper edge. Vertical heat flux curve was formed by adjusting heat flux multipliers in different heights (Table 19) to achieve calculated CRs as similar as measured CRs (Table 18). New heat flux curve was created (Figure 41).

Table 19. Heat flux multiplier related to height.

Furnace height (%)	Heat flux multiplier (%)	Furnace height (%)	Heat flux multiplier (%)	Furnace height (%)	Heat flux multiplier (%)	Furnace height (%)	Heat flux multiplier (%)
0.00	160.00	26.00	140.19	52.00	96.18	78.00	55.18
1.00	160.00	27.00	139.19	53.00	94.18	79.00	53.68
2.00	160.00	28.00	138.69	54.00	92.18	80.00	52.18
3.00	160.00	29.00	136.99	55.00	90.18	81.00	51.27
4.00	159.50	30.00	135.74	56.00	88.18	82.00	50.36
5.00	159.00	31.00	133.92	57.00	86.18	83.00	49.45
6.00	158.50	32.00	132.10	58.00	84.18	84.00	48.54
7.00	158.00	33.00	130.28	59.00	82.18	85.00	47.63
8.00	157.50	34.00	128.46	60.00	80.82	86.00	46.73
9.00	157.00	35.00	127.19	61.00	79.45	87.00	45.82
10.00	156.00	36.00	125.83	62.00	78.09	88.00	44.91
11.00	155.00	37.00	124.01	63.00	76.73	89.00	44.00
12.00	154.00	38.00	122.19	64.00	75.36	90.00	43.09
13.00	153.00	39.00	120.37	65.00	74.00	91.00	42.18
14.00	152.00	40.00	118.55	66.00	72.63	92.00	41.07
15.00	151.00	41.00	116.74	67.00	71.27	93.00	40.96
16.00	150.00	42.00	114.92	68.00	69.91	94.00	40.85
17.00	149.00	43.00	113.10	69.00	68.54	95.00	40.74
18.00	148.00	44.00	111.28	70.00	67.18	96.00	40.62
19.00	147.00	45.00	109.46	71.00	65.68	97.00	40.51
20.00	146.19	46.00	107.64	72.00	64.18	98.00	40.40
21.00	145.19	47.00	105.83	73.00	62.68	99.00	40.29
22.00	144.19	48.00	104.01	74.00	61.18	100.00	40.00
23.00	143.19	49.00	102.19	75.00	59.68		
24.00	142.19	50.00	100.19	76.00	58.18		
25.00	141.19	51.00	98.17	77.00	56.68	Average	100.00 %

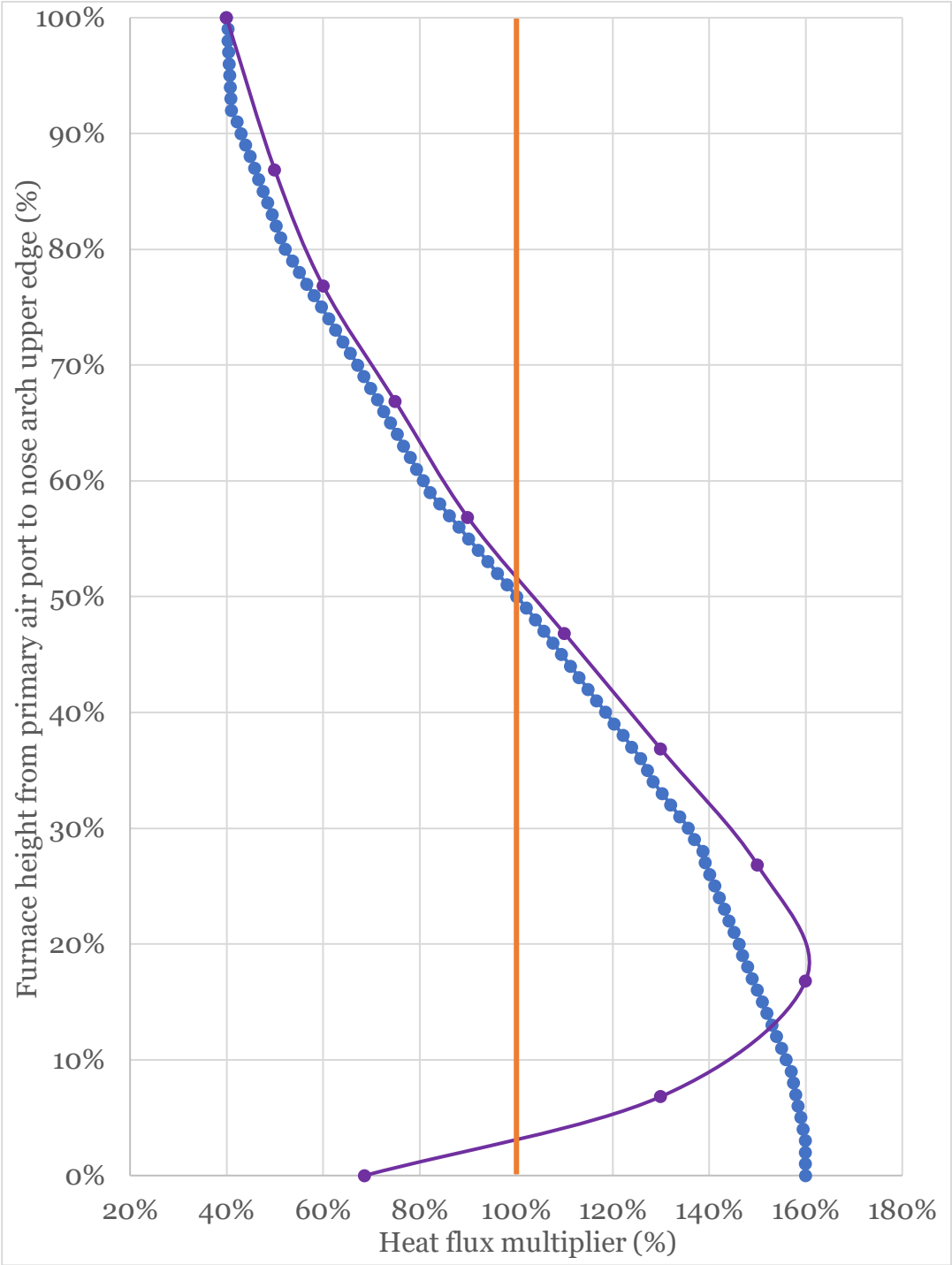

Figure 41. Blue curve is heat flux multiplier related to height measured from primary air port to nose arch upper edge using Table 19 data and purple is rescaled Figure 12 in Section 3.3 vertical heat flux curve.

New heat flux curve (Figure 41) supports both Boiler 1 CR results at lower furnace levels and Figure 12 in Section 3.3 heat flux curve. There are no CR

values measured above 20% of height so above that point heat flux multipliers were chosen based on Figure 12 in Section 3.3 curve.

Observed height is calculated using Equation (68)

$$l\% = \frac{l_m}{l_h} \tag{68}$$

where l% is height observed (%), l_m is measurement point height from primary air port (m) and l_h is furnace height from primary air port to nose arch upper edge (m).

4.6 Calculation model correlations

With the foundational principles of the calculation model established in previous sections, it becomes possible to evaluate multiple correlations by systematically combining the derived equations. Correlation between internal deposit thickness and the temperature of the cladding surface facing the furnace can be obtained by combining Equations (58), (61), and (64), resulting in Equation (69)

$$T_{cf} = q_l \frac{x_{cl}}{k_{cl}} + q_l \frac{x_{cs}}{k_{cs}} + q_l \frac{x_d}{k_d} + T_{wd} \tag{69}$$

where T_{cf} is temperature of cladding surface facing the furnace (°C) for either AISI 304 or Sanicro 38, q_l is heat flux in observed location (W/m²), x_{cl} is cladding thickness for either AISI 304 or Sanicro 38 (m), k_{cl} is cladding thermal conductivity for either AISI 304 or Sanicro 38 (W/mK), x_{cs} is carbon steel thickness (m), k_{cs} is carbon steel thermal conductivity (W/mK) and x_d is average internal deposits thickness (m), k_d is deposits thermal conductivity (W/mK) and T_{wd} is temperature of deposit surface facing water (°C). Figure 42 shows cladding surface facing furnace temperature as a function of internal deposit thickness when Boiler 1 Table 12 parameters are used.

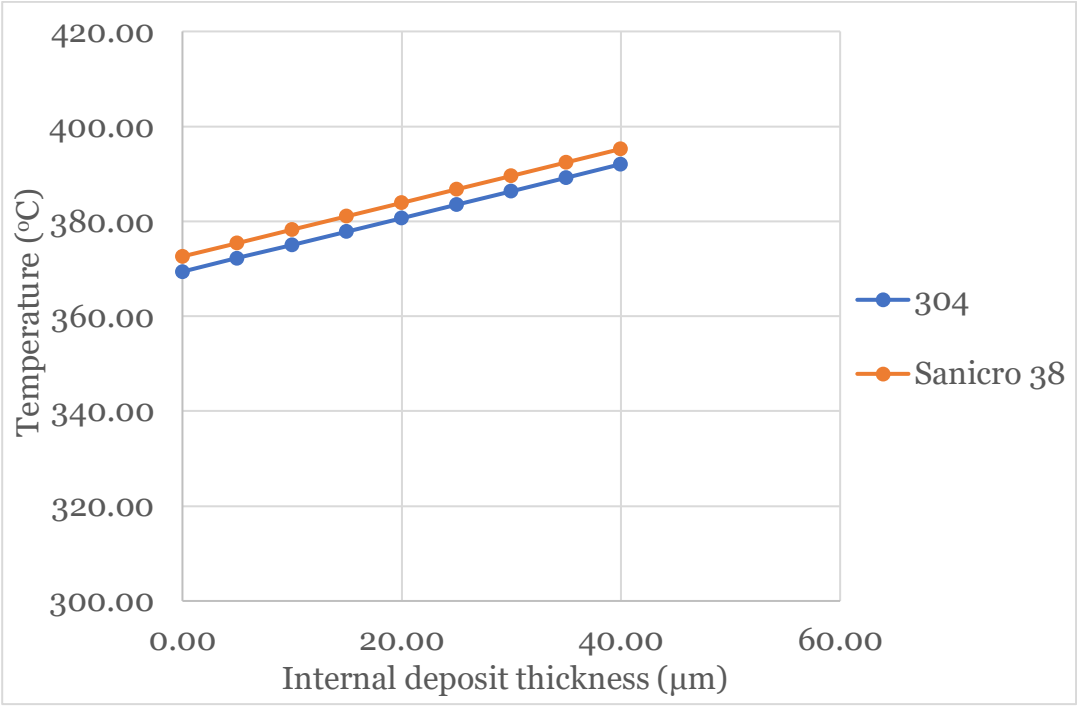

Figure 42. Boiler 1 temperature of cladding surface facing furnace as a function of internal deposits thickness.

Equation (69) in conjunction with Equations (66) and (67), forms a core predictive function for evaluating the CR of AISI 304 and Sanicro 38 cladding materials under varying internal deposit conditions as can be seen in Figure 43.

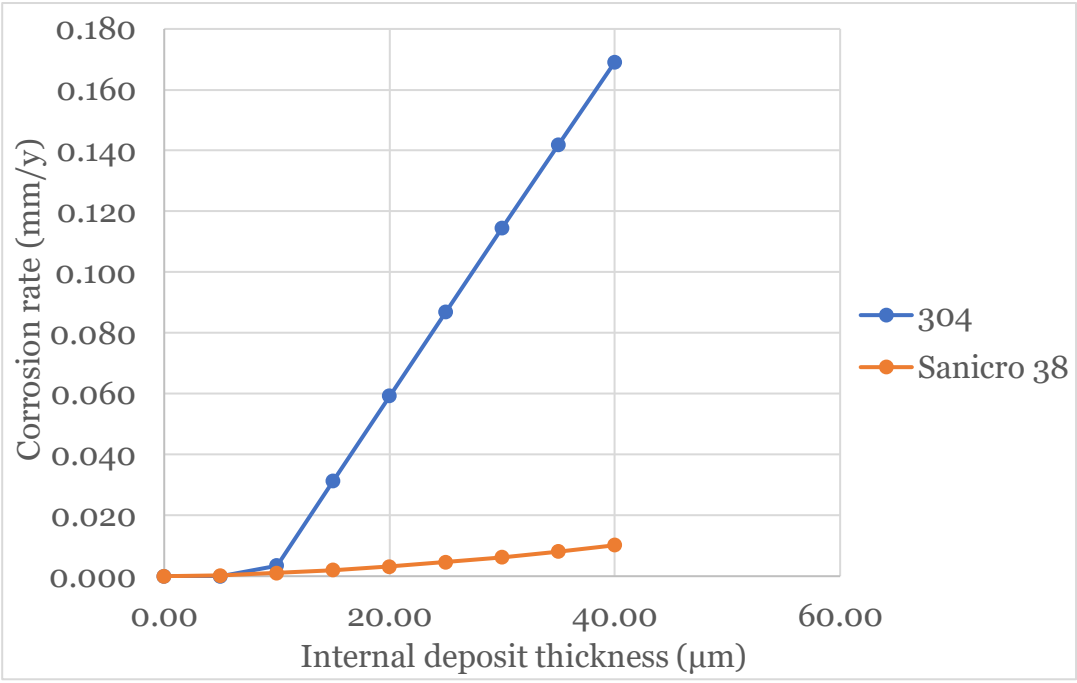

Figure 43. Boiler 1 CR as a function of internal deposit thickness.

By extending the model further, one can explore how boiler height impacts corrosion behaviour. By combining Equations (57) and (69) results Equation (70)

$$T_{cf} = q_l \frac{x_{cl}}{k_{cl}} + q_l \frac{x_{cs}}{k_{cs}} + q_l \frac{x_d}{k_d} + \frac{q_l}{h} + T_w \quad (70)$$

where T_{cf} is temperature of cladding surface facing furnace (^oC) for either AISI 304 or Sanicro 38, q_l is heat flux in observed location (W/m^2), x_{cl} is cladding thickness for either AISI 304 or Sanicro 38 (m), k_{cl} is cladding thermal conductivity for either AISI 304 or Sanicro 38 (W/mK), x_{cs} is carbon steel thickness (m), k_{cs} is carbon steel thermal conductivity (W/mK) and x_d is average deposit thickness (m), k_d is deposit thermal conductivity (W/mK) and h is heat transfer coefficient (W/m^2K) and T_w is saturated water temperature (^oC). Rearranging Equation (70), Equation (71) is formed.

$$T_{cf} = q_l \left(\frac{x_{cl}}{k_{cl}} + \frac{x_{cs}}{k_{cs}} + \frac{x_d}{k_d} + \frac{1}{h}\right) + T_w \quad (71)$$

In this formation, the heat flux multiplier can be adjusted according to the relative height within the furnace, based on the values presented in Table 19. By combining Equations (66), (67) and (71) enables the calculation model to evaluate how corrosion behaviour varies across different vertical levels of the KRB for both cladding materials as can be seen in Figure 44.

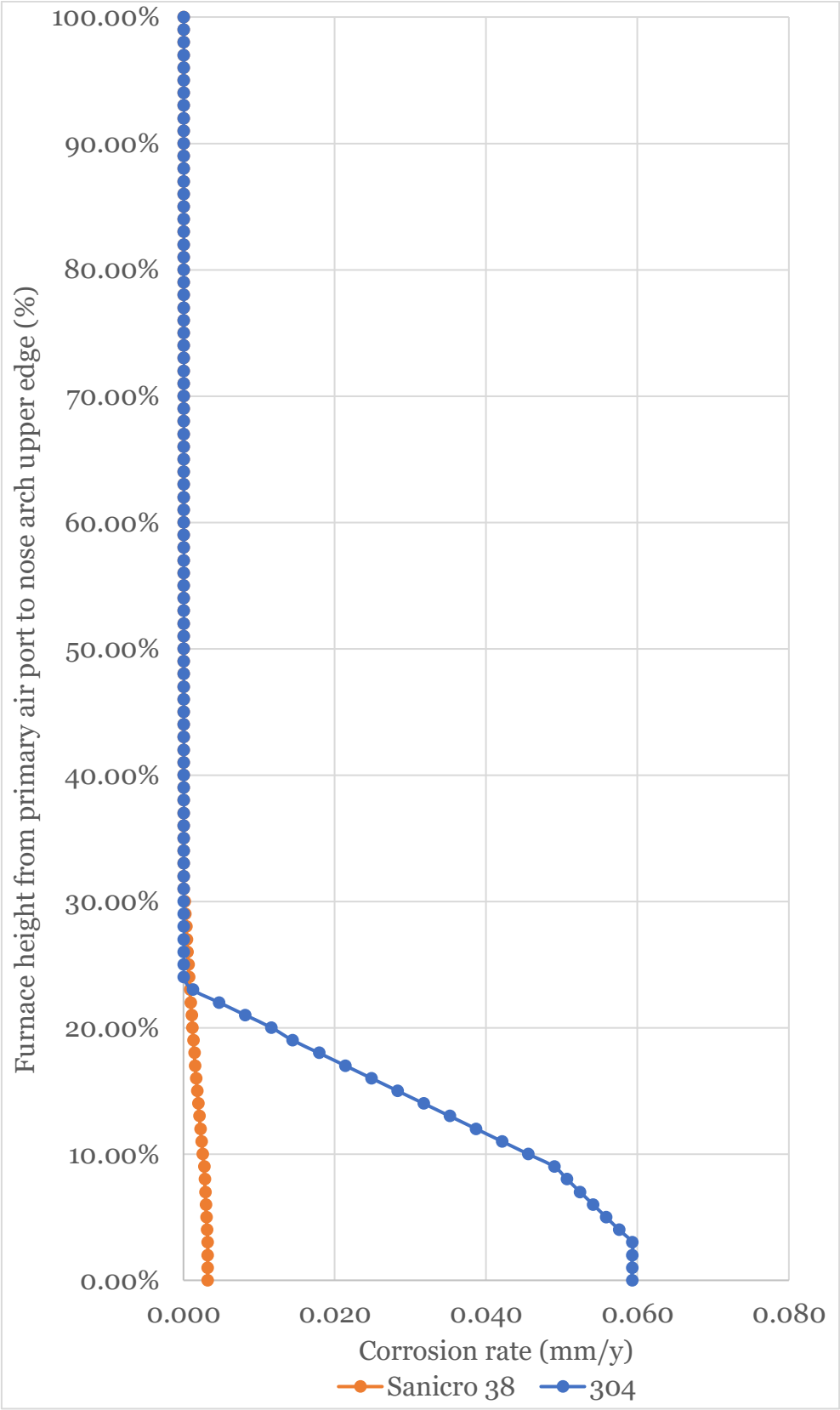

Figure 44. Boiler 1 CR in different relative heights using Table 12 values.

5 Results and discussion

In this section, the developed calculation model is applied using input parameters provided by boiler operators. These inputs include operational conditions such as furnace dimensions, DS firing rate, black liquor HHV, steam drum pressure, tube geometry, and material specifications for both cladding types AISI 304 and Sanicro 38.

There are no universally defined guidelines specifying the maximum allowable annual corrosion rate for cladding materials. However, to establish a practical baseline for comparison, it is assumed in this work that up to 20% of the original cladding thickness may be lost over the material's service life. Given that the typical thickness of AISI 304 cladding is approximately 1.65 mm, this corresponds to a permissible reduction of 0.33 mm before tube replacement is required. Assuming a design life of 30 years, this yields an allowable average corrosion rate of approximately 0.011 mm/year. In practice, the critical consideration is not necessarily full compliance with this annual CR, but rather ensuring that a sufficient layer of cladding remains intact until the next scheduled maintenance or inspection interval.

In Section 5.1 calculation model results are compiled and evaluated separately for Boilers 1-3. In Section 5.2 input parameters such as steam drum pressure, internal deposit thickness and thermal conductivity, water vapor/liquid ratio and floor loading and floor area are changed in Boiler 1 and results are analysed. In Section 5.3 sensitivity analysis for calculation model is presented.

5.1 Boiler simulations

To evaluate the applicability and accuracy of the developed calculation model, input data were collected from operators of eight different KRBs located across Finland and Sweden. These KRBs, referred to as Boiler 1 through Boiler 8, represent a diverse set of operational conditions, furnace dimensions, and material configurations.

For each KRB, a simulation was performed using operator-provided parameters. The calculation model then predicted key variables, including cladding surface temperature and estimated CR for both AISI 304 and Sanicro 38. Results for Boilers 1-3 are in Chapters 5.1.1-5.1.3.

5.1.1 Boiler 1

Data from Boiler 1 (Khodahami, 2024) served as the foundation for determining the temperature-dependent corrosion rate (CR) of AISI 304, as well as for constructing the vertical heat flux distribution curve. According to the information provided, Sanicro 38 is used as the cladding material below Pos 1, approximately 0.75 meters above the primary air port, while AISI 304 is employed above that point. Based on this configuration, the model is used to extrapolate the maximum allowable internal deposit thickness that would keep the corrosion rate below 0.011 mm/year for both cladding materials. The input parameters used for this calculation are presented in Table 20, and the corresponding results are summarized in Table 21.

Table 20. Boiler 1 inputs.

Term	Symbol	Unit	AISI 304	Sanicro 38
Furnace width	l_w	(m)	13.526	
Furnace depth	l_d	(m)	15.028	
Furnace height from the primary air port to nose arch upper edge	l_h	(m)	37.900	
Height observed from primary air port	l_i	(m)	1.000	
Relative location percentage	l%	(%)	2.64 %	
Boiler load / DS firing rate	$\dot{m}DS$	(tDS/day)	5000.000	
Higher heating value	HHV	(MJ/kgDS)	12.620	
Total wall thickness	x_t	(mm)	6.530	
Tube outside diameter	D_{to}	(mm)	63.500	
Tube inside diameter	D_{ti}	(mm)	50.440	
Tube inside area	A_{ti}	(m^2)	0.002	
Steam drum pressure	P	(bar)	120.000	
Drum water velocity	u_l	(m/s)	2.000	
Density water liquid 100%	ρ_l	(kg/m^3)	655.180	
Water vapor-%	v-%	(%)	0 %	
Water liquid-%	l-%	(%)	100 %	
Velocity water/steam	u_w	(m/s)	2.000	
Density water/steam	ρ_w	(kg/m^3)	655.180	
Dynamic viscosity water/steam	μ_w	(Pa·s)	7.65E-05	
Specific heat capacity water/steam	c_w	(J/kgK)	6809.100	
Thermal conductivity water/steam	k_w	(W/mK)	0.512	

Term	Symbol	Unit	AISI 304	Sanicro 38
Thermal conductivity deposits	k_d	(W/mK)	0.300	
Thermal conductivity carbon steel	k_{cs}	(W/mK)	45.042	
Thermal conductivity cladding	k_{cl}	(W/mK)	20.878	16.857
Thermal conductivity smelt	k_s	(W/mK)	0.600	
Average deposit thickness	x_d	(µm)	20.000	
Carbon steel thickness	x_{cs}	(mm)	4.880	4.880
Cladding thickness	x_{cl}	(mm)	1.650	1.650
Maximum smelt thickness	x_s	(mm)	1.190	1.179

Table 21. Boiler 1 results.

Term	Symbol	Unit	AISI 304	Sanicro 38
Floor area	A_f	(m^2)	203.269	
Heat input	Q_{tot}	(MW)	730.324	
Floor loading	HHRR	(MW/m^2)	3.593	
Heat flux average	q_a	(kW/m^2)	106.824	
Heat flux multiplier	k_t	(%)	160 %	
Heat flux location	q_l	(kW/m^2)	170.918	
Mass flow water liquid 100%	$\dot{m}_l$	(kg/s)	2.618	
Reynolds number	Re		863834.360	
Prandtl number	Pr		1.018	
Nusselt number	Nu		1300.188	
Heat transfer coefficient	h	(W/m^2K)	13189.280	
Temperature water/steam	T_w	(^oC)	324.680	
Temperature deposit surface facing water	T_{wd}	(^oC)	337.639	
Temperature deposit-carbon steel interface	T_{dc}	(^oC)	349.033	
Temperature carbon steel-cladding interface	T_{cc}	(^oC)	367.551	367.551
Temperature cladding surface facing furnace	T_{cf}	(^oC)	381.059	384.282
Temperature smelt surface facing furnace	T_{ss}	(^oC)	720.000	
Corrosion rate	CR	(mm/y)	0.059	0.003

As can be observed from Table 20 and 21 Boiler 1 is relatively large KRB with high floor loading, heat flux and steam drum pressure. High steam drum pressure and heat flux increases water/steam and tube temperature (Figure 45) allowing only thin layer of internal deposits as can be seen on Figure 46. Internal deposit thickness must remain thinner than 12 µm to maintain

allowed CR for AISI 304 and 42 µm for Sanicro 38. According to Figure 47 only relatively thin layer of internal deposits are allowed in furnace wall tubes as even 20 µm results five times higher CR for AISI 304. It is recommended that water quality needs to be controlled, and Sanicro 38 cladding material switched below 20% of furnace height from primary air port to nose arch upper edge as approximately 8 meters from furnace floor (Table 16 and 17 from Section 4.5).

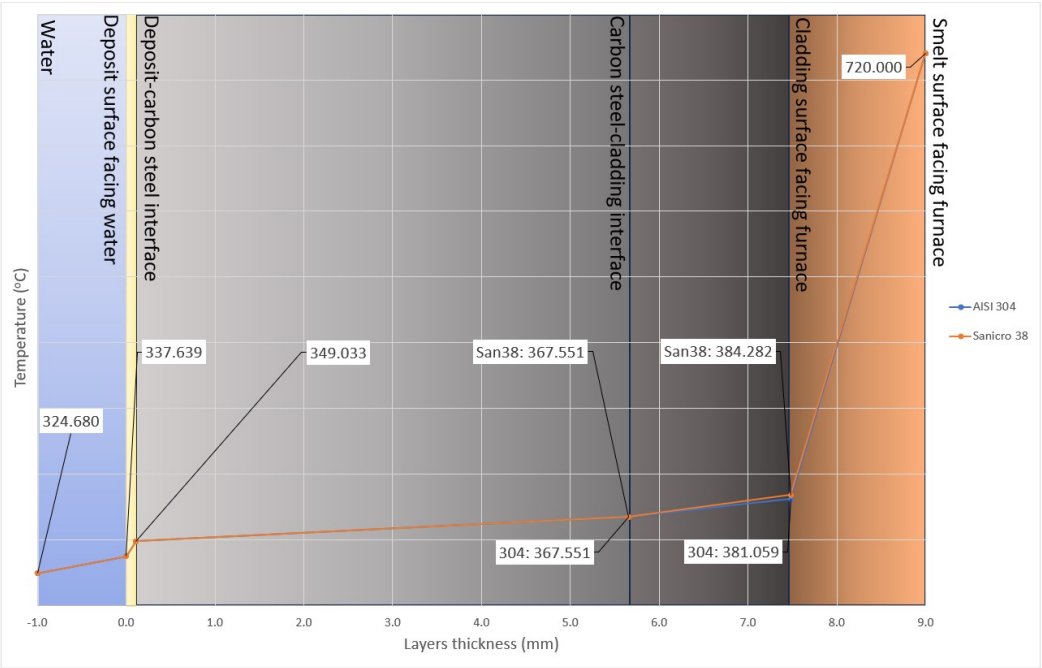

Figure 45. Boiler 1 interface temperatures with 20 µm internal deposits thickness.

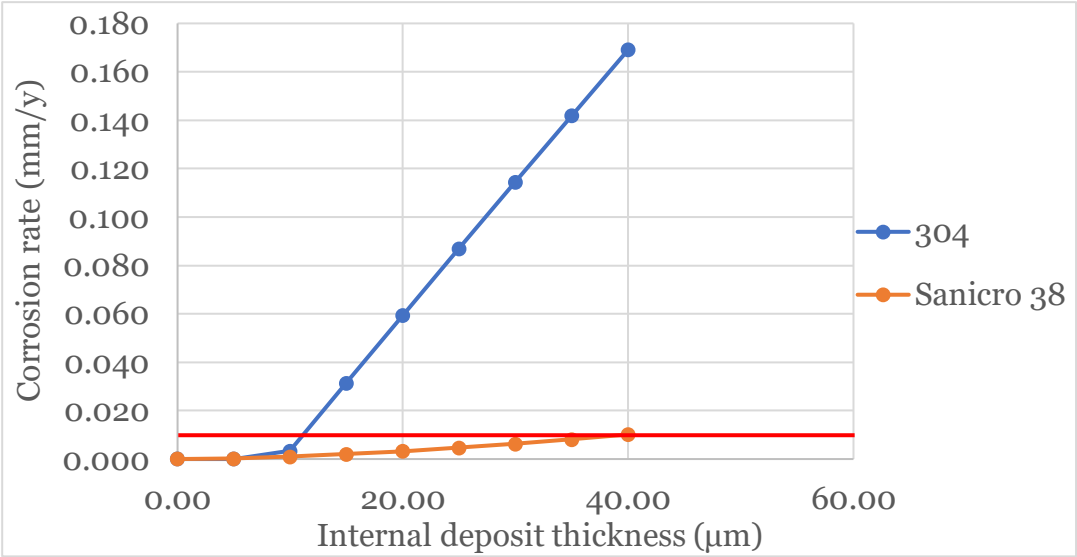

Figure 46. Boiler 1 cladding CR as a function of internal deposit thickness. Red line marks permitted CR of 0.011 mm/y.

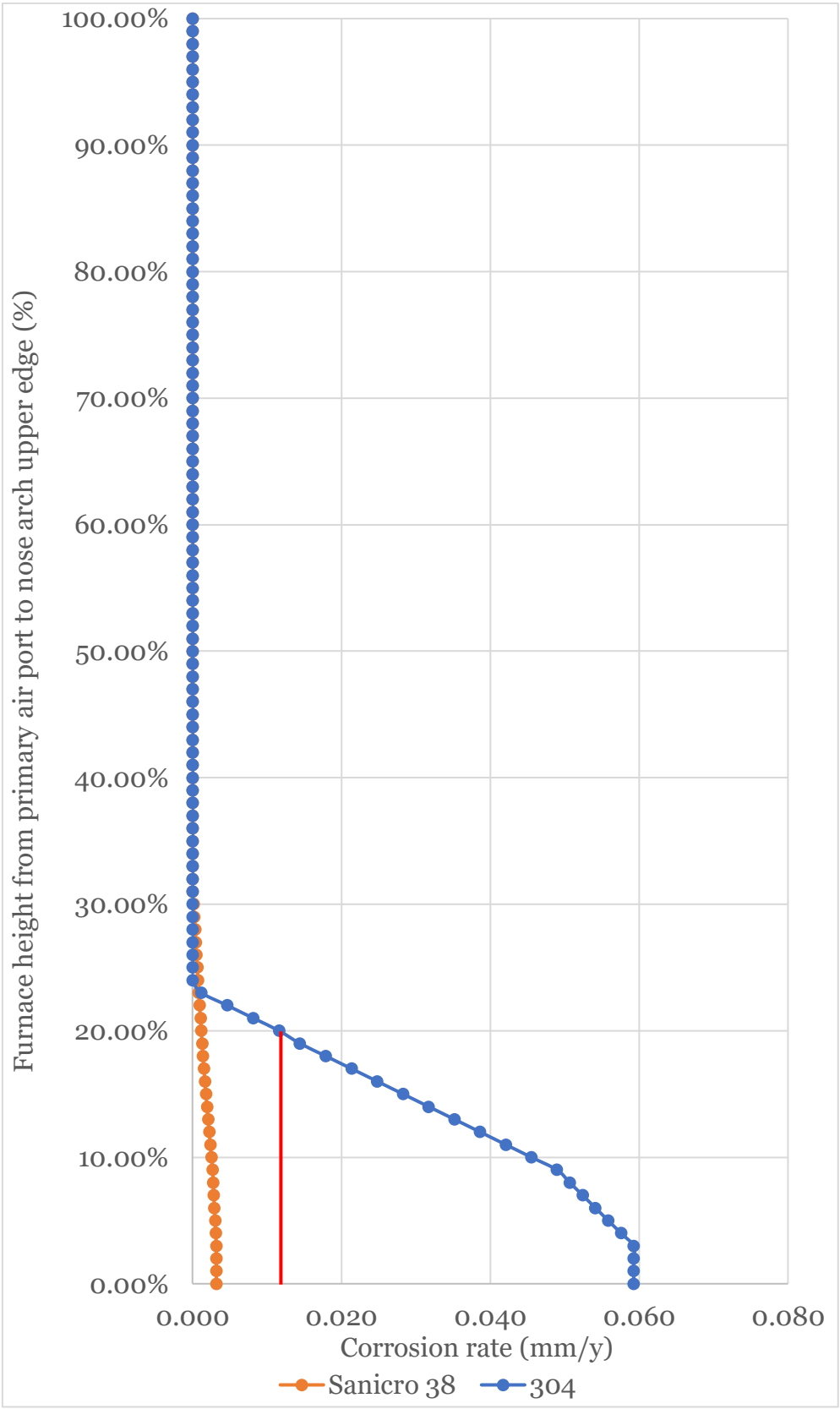

Figure 47. Boiler 1 CR as a function of furnace height. Red line marks permitted CR of 0.011 mm/y.

5.1.2 Boiler 2

Data from Boiler 2 (Kiwa, 2014) was used to construct the polynomial CR curve for Sanicro 38 and to more precisely determine the temperature at which the CR approaches zero for this material (Table 13 from Section 4.4). The AISI 304 corrosion data point from Boiler 2 reporting a CR of 0.057 mm/year at 371.88 °C was excluded from the model. This decision was made because the value was too close to the Boiler 1 data point 0.059 mm/year at 381.06 °C (Table 12 from Section 4.4), and including both would have introduced inconsistency into the regression function. As a result, the model does not predict corrosion for AISI 304 in Boiler 2 accurately, since the operating temperature is approximately 10 °C lower than the threshold defined by the selected corrosion function.

As shown in Tables 22 and 23, Boiler 2 is a medium-sized KRB with average floor loading and heat flux but operates at a relatively high steam drum pressure. The elevated steam drum pressure maintains a higher water/steam saturation temperature. However, the lower heat flux results in reduced tube wall temperatures when compared to Boiler 1 (Figure 48). This combination of thermal parameters permits relatively thicker internal deposit layers in Boiler 2 while still maintaining acceptable corrosion performance (Figure 49).

Table 22. Boiler 2 inputs.

Term	Symbol	Unit	AISI 304	Sanicro 38
Furnace width	l_w	(m)	10.038	
Furnace depth	l_d	(m)	11.440	
Furnace height from the primary air port to nose upper edge	l_h	(m)	28.670	
Height observed from primary air port	l_i	(m)	0.400	
Relative location percentage	l%	(%)	1.40 %	
Boiler load / DS firing rate	$\dot{m}DS$	(tDS/day)	2400.000	
Higher heating value	HHV	(MJ/kgDS)	12.650	
Total wall thickness	x_t	(mm)	6.530	
Tube outside diameter	D_{to}	(mm)	63.500	
Tube inside diameter	D_{ti}	(mm)	50.440	
Tube inside area	A_{ti}	(m^2)	0.002	
Steam drum pressure	P	(bar)	119.000	
Drum water velocity	u_{lt}	(m/s)	2.000	

Term	Symbol	Unit	AISI 304	Sanicro 38
Density water liquid 100%	ρ_l	(kg/m³)	656.850	
Water vapor-%	v-%	(%)	0 %	
Water liquid-%	l-%	(%)	100 %	
Velocity water/steam	u_w	(m/s)	2.000	
Density water/steam	ρ_w	(kg/m³)	656.850	
Dynamic viscosity water/steam	μ_w	(Pa·s)	7.68E-05	
Specific heat capacity water/steam	c_w	(J/kgK)	6769.000	
Thermal conductivity water/steam	k_w	(W/mK)	0.513	
Thermal conductivity deposits	k_d	(W/mK)	0.300	
Thermal conductivity carbon steel	k_{cs}	(W/mK)	45.033	
Thermal conductivity cladding	k_{cl}	(W/mK)	20.839	16.817
Thermal conductivity smelt	k_s	(W/mK)	0.600	
Average deposit thickness	x_d	(µm)	30.000	
Carbon steel thickness	x_{cs}	(mm)	4.880	4.880
Cladding thickness	x_{cl}	(mm)	1.650	1.650
Maximum smelt thickness	x_s	(mm)	1.422	1.410

Table 23. Boiler 2 results.

Term	Symbol	Unit	AISI 304	Sanicro 38
Floor area	A_f	(m²)	114.835	
Heat input	Q_{tot}	(MW)	351.389	
Floor loading	HHRR	(MW/m²)	3.060	
Heat flux average	q_a	(kW/m²)	90.561	
Heat flux multiplier	k_t	(%)	160 %	
Heat flux location	q_l	(kW/m²)	144.898	
Mass flow water liquid 100%	$\dot{m}_l$	(kg/s)	2.625	
Reynolds number	Re		863238.207	
Prandtl number	Pr		1.013	
Nusselt number	Nu		1296.908	
Heat transfer coefficient	h	(W/m²K)	13185.828	
Temperature water/steam	T_w	(°C)	324.040	
Temperature deposit surface facing water	T_{wd}	(°C)	335.029	
Temperature deposit-carbon steel interface	T_{dc}	(°C)	349.519	

Term	Symbol	Unit	AISI 304	Sanicro 38
Temperature carbon steel-cladding interface	T_{cc}	(°C)	365.220	365.220
Temperature cladding surface facing furnace	T_{cf}	(°C)	376.693	379.437
Temperature smelt surface facing furnace	T_{ss}	(°C)	720.000	
Corrosion rate	CR	(mm/y)	0.017	0.001

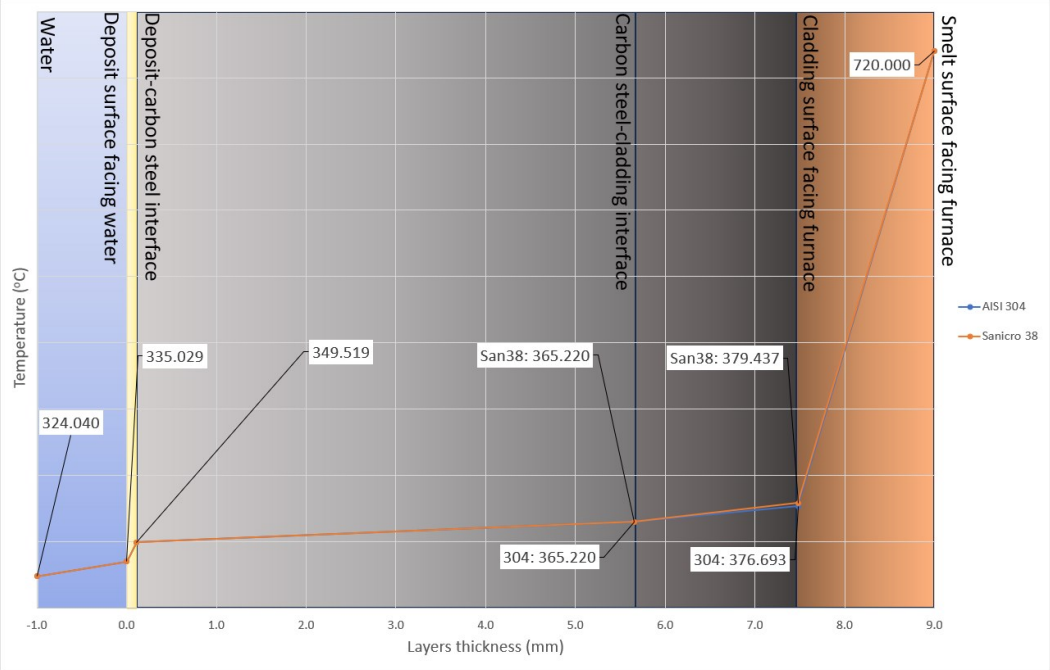

Figure 48. Boiler 2 interface temperatures with 30 µm internal deposits thickness.

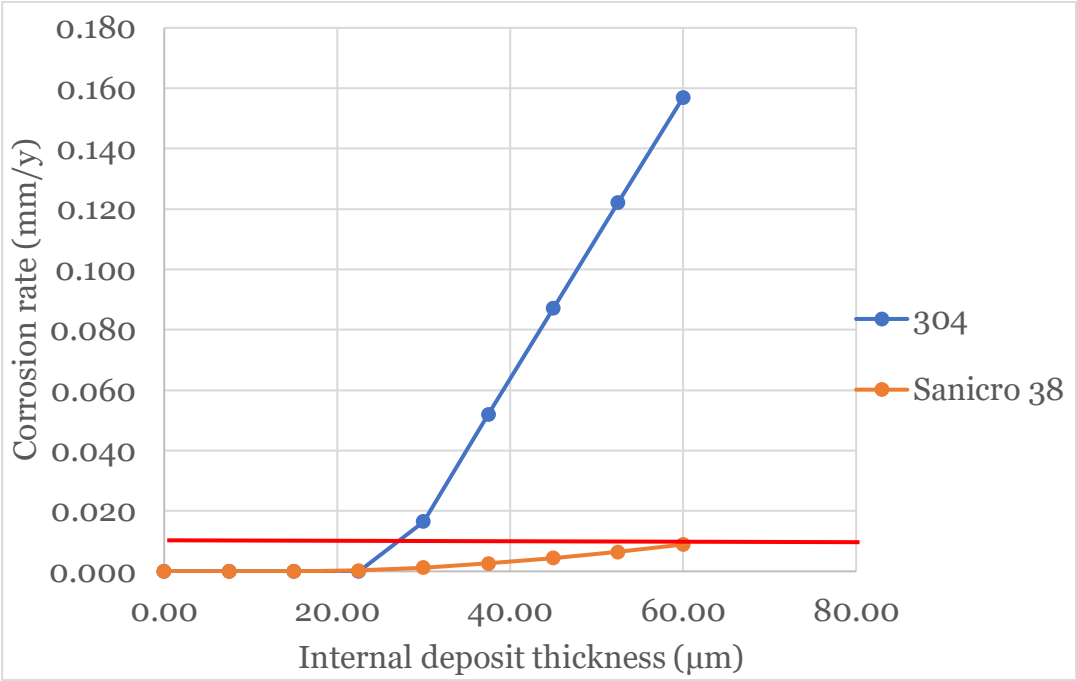

Figure 49. Boiler 2 cladding CR as a function of internal deposit thickness. Red line marks permitted CR of 0.011 mm/y.

Internal deposit thickness must remain thinner than 27 µm to maintain allowed CR for AISI 304 and 60 µm for Sanicro 38. According to Figure 50 there can be relatively thick internal deposits as 30 µm deposits increase AISI 304 CR to 0.017 mm/y and CR is higher than recommended just at lower 6% of furnace height from primary air port to nose arch upper edge approximately 2.5 meters from furnace floor (Table 16 and 17 from Section 4.5). It is recommended to control water quality or change cladding materials to Sanicro 38 at lower 10% of furnace height.

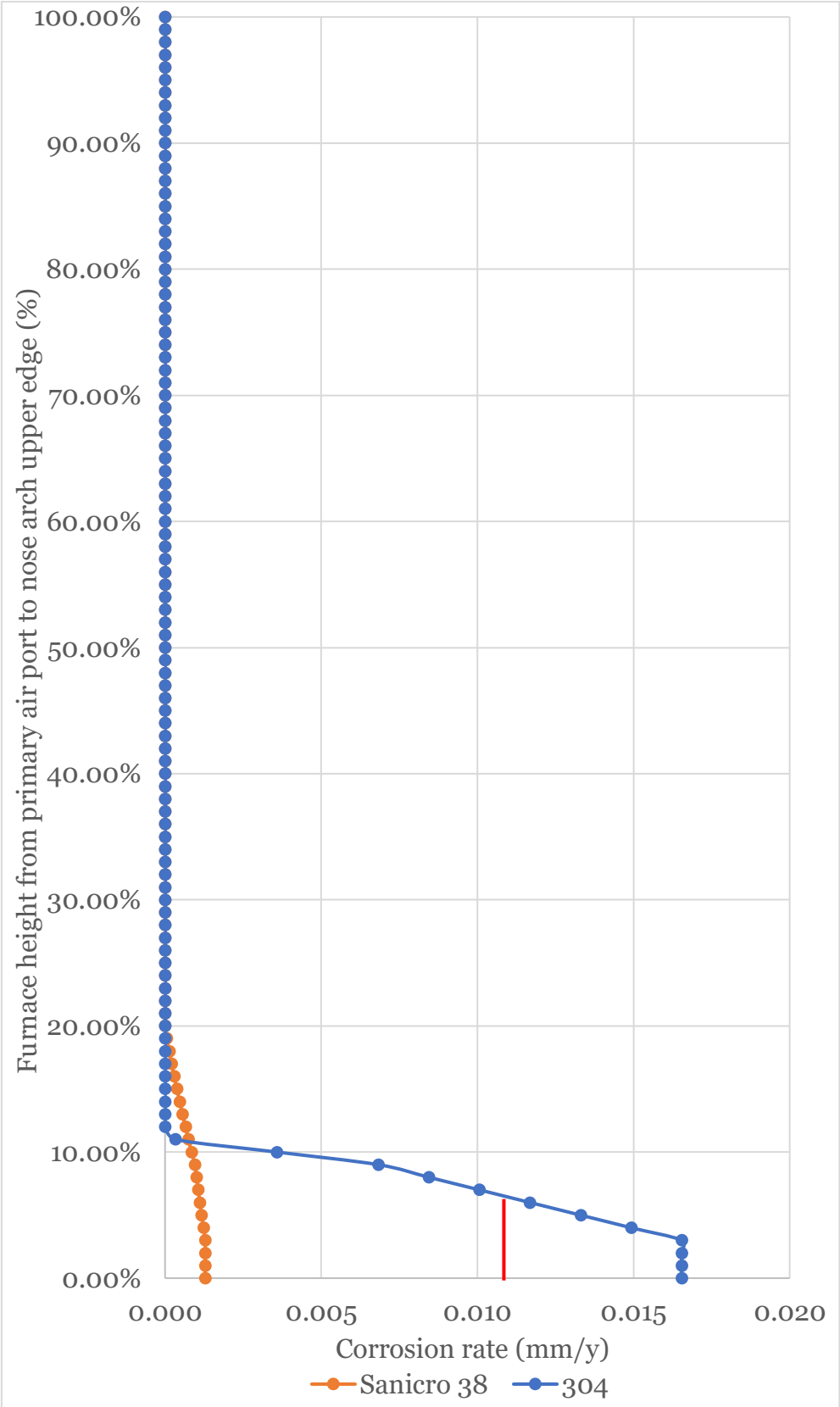

Figure 50. Boiler 2 CR as a function of furnace height. Red line marks permitted CR of 0.011 mm/y.

5.1.3 Boiler 3

Data from Boiler 3 (Liikola, 2015) was used to construct the polynomial CR curve for AISI 304 in extremely high CR and cladding temperature as thick internal deposits were measured during inspection. As shown in Tables 24 and 25, Boiler 3 is a small-sized KRB with small floor loading and heat flux and operates at a relatively low steam drum pressure. Low steam drum pressure maintains a low water/steam saturation temperature (Figure 51). Low heat flux results reduced tube wall temperatures when compared to Boiler 1 and 2. This combination of thermal parameters permits significantly thicker internal deposit layers in Boiler 3 while still maintaining acceptable corrosion performance (Figure 52).

Table 24. Boiler 3 inputs.

Term	Symbol	Unit	AISI 304	Sanicro 38
Furnace width	l_w	(m)	4.190	
Furnace depth	l_d	(m)	4.952	
Furnace height from the primary air port to nose arch upper edge	l_h	(m)	10.823	
Height observed from primary air port	l_i	(m)	0.300	
Relative location percentage	l%	(%)	2.77 %	
Boiler load / DS firing rate	$\dot{m}$DS	(tDS/day)	250.000	
Higher heating value	HHV	(MJ/kgDS)	13.000	
Total wall thickness	x_t	(mm)	5.300	
Tube outside diameter	D_{to}	(mm)	60.300	
Tube inside diameter	D_{ti}	(mm)	49.700	
Tube inside area	A_{ti}	(m^2)	0.002	
Steam drum pressure	P	(bar)	92.000	
Drum water velocity	u_l	(m/s)	2.000	
Density water liquid 100%	ρ_l	(kg/m^3)	701.800	
Water vapor-%	v-%	(%)	0 %	
Water liquid-%	l-%	(%)	100 %	
Velocity water/steam	u_w	(m/s)	2.000	
Density water/steam	ρ_w	(kg/m^3)	701.800	
Dynamic viscosity water/steam	μ_w	(Pa·s)	8.40E-05	
Specific heat capacity water/steam	c_w	(J/kgK)	5903.500	
Thermal conductivity water/steam	k_w	(W/mK)	0.545	

Term	Symbol	Unit	AISI 304	Sanicro 38
Thermal conductivity deposits	k_d	(W/mK)	0.300	
Thermal conductivity carbon steel	k_{cs}	(W/mK)	44.722	
Thermal conductivity cladding	k_{cl}	(W/mK)	20.989	16.970
Thermal conductivity smelt	k_s	(W/mK)	0.600	
Average deposit thickness	x_d	(µm)	200.000	
Carbon steel thickness	x_{cs}	(mm)	3.650	3.650
Cladding thickness	x_{cl}	(mm)	1.650	1.650
Maximum smelt thickness	x_s	(mm)	2.423	2.412

Table 25. Boiler 3 results.

Term	Symbol	Unit	AISI 304	Sanicro 38
Floor area	A_f	(m^2)	20.751	
Heat input	Q_{tot}	(MW)	37.616	
Floor loading	HHRR	(MW/m^2)	1.813	
Heat flux average	q_a	(kW/m^2)	52.503	
Heat flux multiplier	k_t	(%)	160 %	
Heat flux location	q_l	(kW/m^2)	84.005	
Mass flow water liquid 100%	$\dot{m}_l$	(kg/s)	2.723	
Reynolds number	Re		830453.447	
Prandtl number	Pr		0.910	
Nusselt number	Nu		1204.388	
Heat transfer coefficient	h	(W/m^2K)	13208.038	
Temperature water/steam	T_w	(^oC)	304.930	
Temperature deposit surface facing water	T_{wd}	(^oC)	311.290	
Temperature deposit-carbon steel interface	T_{dc}	(^oC)	367.293	
Temperature carbon steel-cladding interface	T_{cc}	(^oC)	374.149	374.149
Temperature cladding surface facing furnace	T_{cf}	(^oC)	380.753	382.317
Temperature smelt surface facing furnace	T_{ss}	(^oC)	720.000	
Corrosion rate	CR	(mm/y)	0.056	0.002

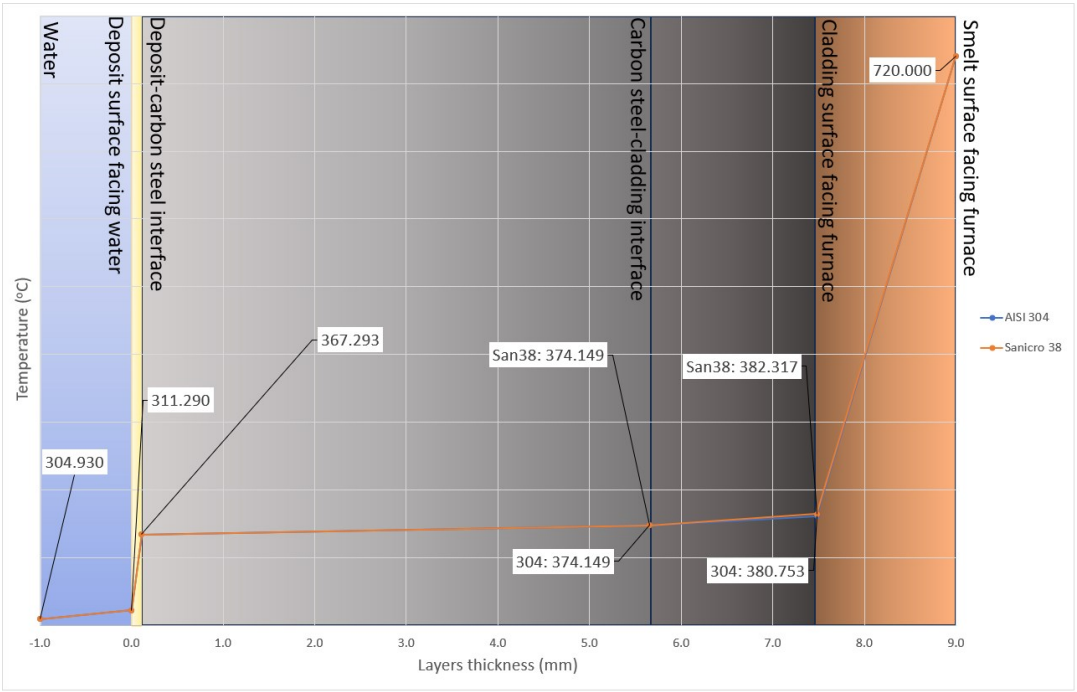

Figure 51. Boiler 3 interface temperatures with 200 µm internal deposits thickness.

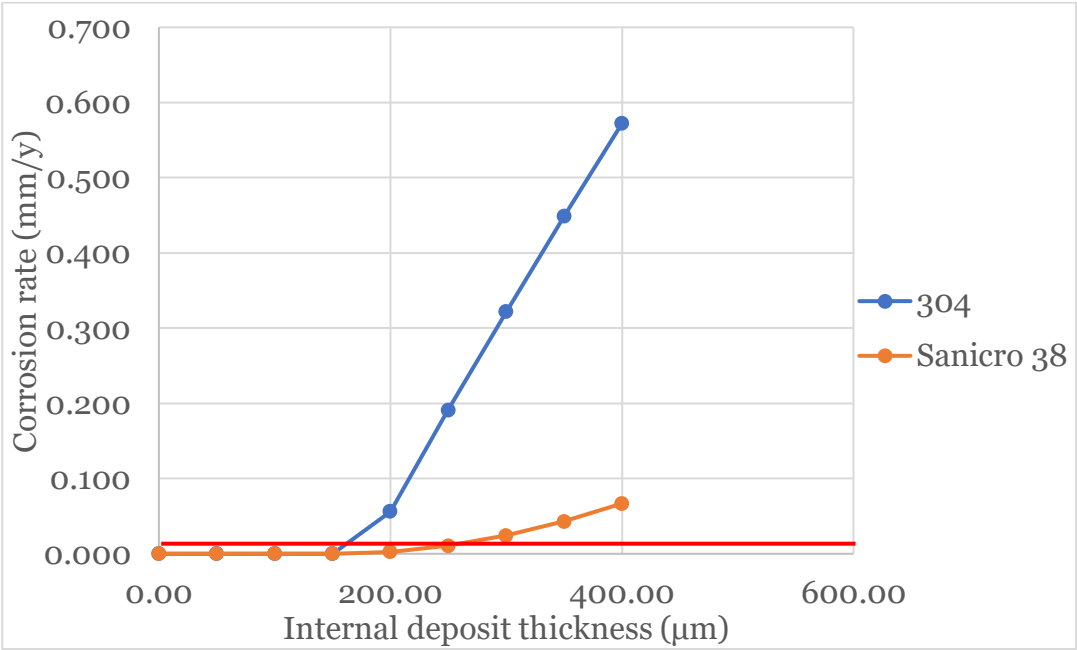

Figure 52. Boiler 3 cladding CR as a function of internal deposit thickness. Red line marks permitted CR of 0.011 mm/y.

Internal deposit thickness can be as thick as 160 µm to maintain allowed CR for AISI 304 and 275 µm for Sanicro 38. According to Figure 53 there can be thick internal deposits as 200 µm deposits increase AISI 304 CR to only four times higher than recommended just at lower 10% of furnace height from

primary air port to nose arch upper edge approximately 1.5 meters from furnace floor (Table 16 and 17 from Section 4.5). As inspections revealed that there have been findings of extremely thick internal deposit, it is suggested to control water quality and change cladding materials to Sanicro 38 at lower 15% of furnace height approximately 2.5 meters from furnace floor (Table 16 and 17 from Section 4.5).

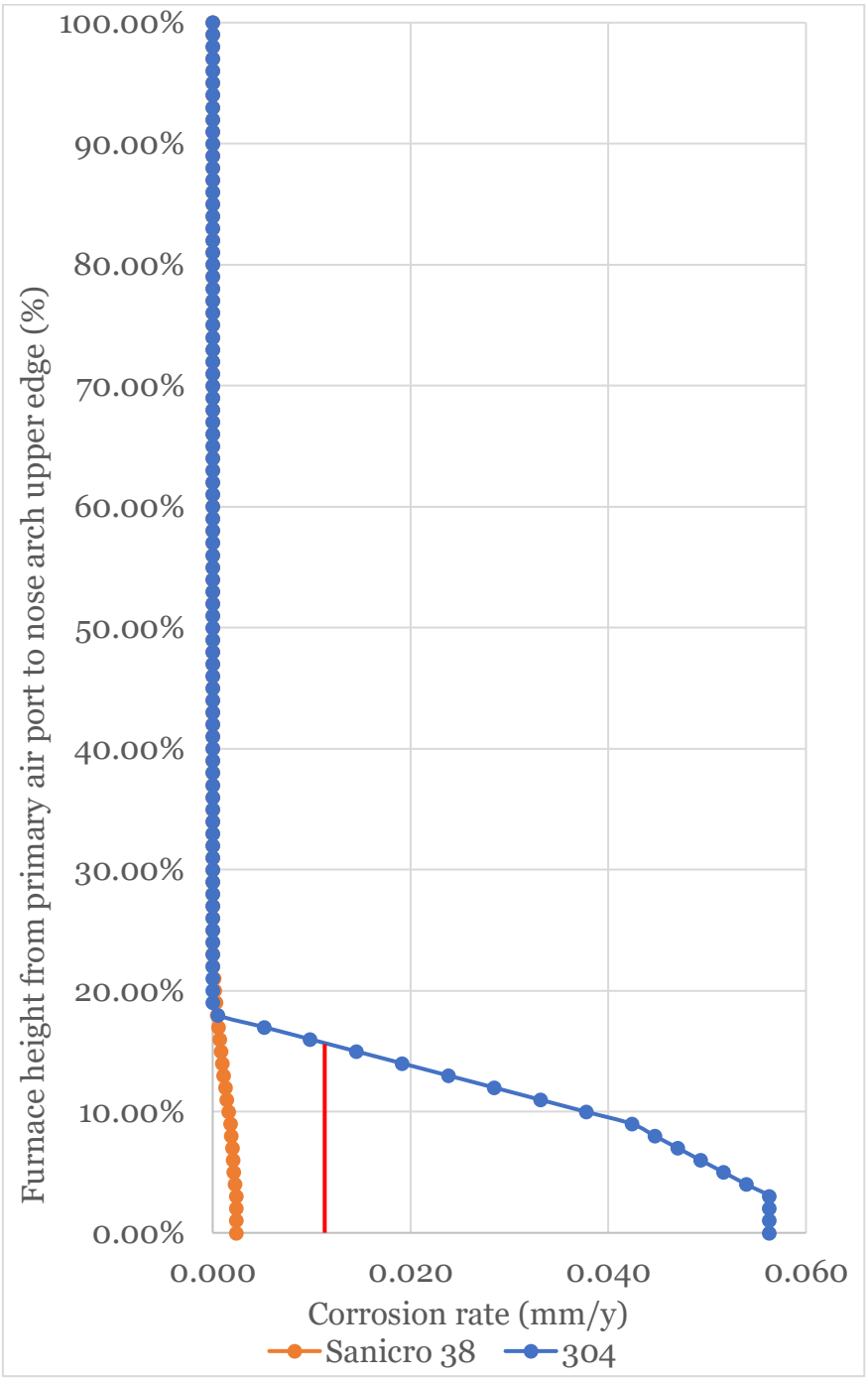

Figure 53. Boiler 3 CR as a function of furnace height. Red line marks permitted CR of 0.011 mm/y.

5.2 Parameter changes in reference boiler

In Section 5.2 input parameters (Table 20) are changed for Boiler 1 and results presented in Table 26. As expected, decreasing steam drum pressure lowers the saturation temperature of water/steam and consequently reduces the CR. As illustrated in Figure 54, the CR of AISI 304 is reduced by approximately 50% when the steam drum pressure is lowered from 120 bar to 115 bar. At 112 bar, the CR falls below the recommendable threshold. When the pressure drops below 108 bar, the CR for both AISI 304 and Sanicro 38 approaches zero.

Table 26. Boiler 1 CR changes when parameters are changed.

Term	CR (mm/y)	
	AISI 304	Sanicro 38
Corrosion rate (120 bar, 20 µm, 0.3 W/mK)	0.059	0.003
Corrosion rate (115 bar)	0.028	0.002
Corrosion rate (112 bar)	0.008	0.001
Corrosion rate (108 bar)	0.000	0.000
Corrosion rate (40 µm)	0.169	0.010
Corrosion rate (80 µm)	0.380	0.034
Corrosion rate (160 µm)	0.773	0.123
Corrosion rate (100 µm, 3 W/mK)	0.004	0.001
Corrosion rate (150 µm, 3 W/mK)	0.032	0.002
Corrosion rate (200 µm, 3 W/mK)	0.059	0.003
Corrosion rate (75% liquid - 25% vapor)	0.063	0.003
Corrosion rate (50% liquid - 50% vapor)	0.070	0.004
Corrosion rate (25% liquid - 75% vapor)	0.084	0.004
Corrosion rate (0% liquid - 100% vapor)	0.124	0.007
Corrosion rate (3300 tDS/day, 11.28 m)	0.000	0.001

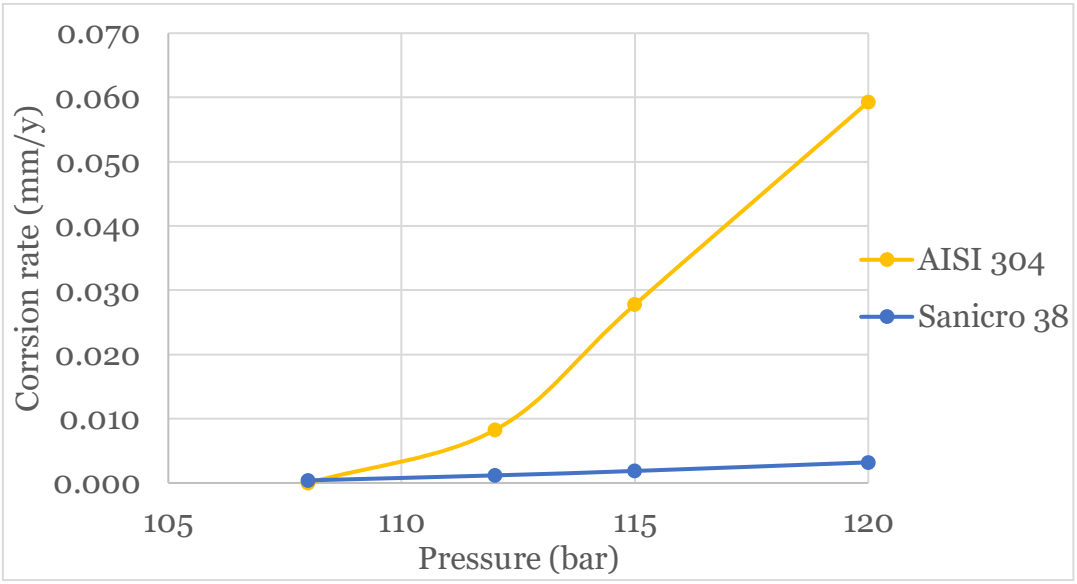

Figure 54. Boiler 1 CR when pressure is changed.

Similarly, increasing the thickness of internal deposits leads to higher CR for both cladding materials (Figure 55). For AISI 304, increasing the internal deposit thickness from 50 µm to 100 µm doubles the corrosion rate, and a further increase to 150 µm doubles it again. However, the thermal conductivity of the deposit plays a critical role. If the deposit consists of high-conductivity magnetite (3 W/mK) instead of low-conductivity impurities (0.3 W/mK), the CR is significantly reduced. For example, at a thickness of 150 µm, the CR for AISI 304 is 0.72 mm/y for an impurity layer, compared to only 0.04 mm/y for a magnetite layer of the same thickness.

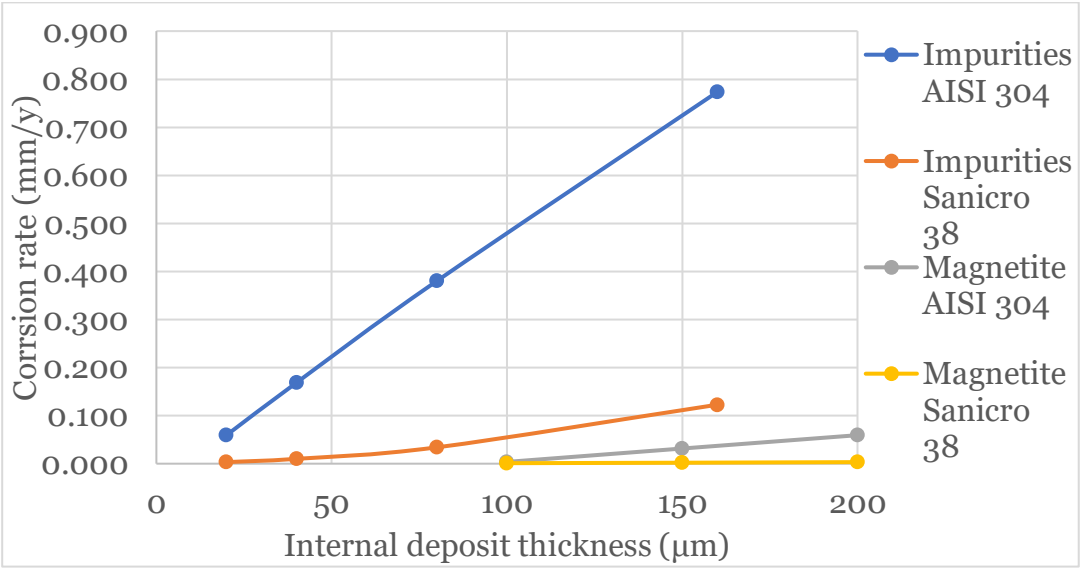

Figure 55. Boiler 1 CR when internal deposit thickness and thermal conductivities are changed. Impurities thermal conductivity is 0.3 W/mK and magnetite thermal conductivity is 3 W/mK.

Changes in the liquid-vapor ratio inside the wall tubes also affect the CR, as shown in Figure 56. The CR remains relatively stable when the vapor content is below 40%, but it increases sharply as the ratio approaches 100% vapor. This highlights the sensitivity of the model to two-phase flow behaviour.

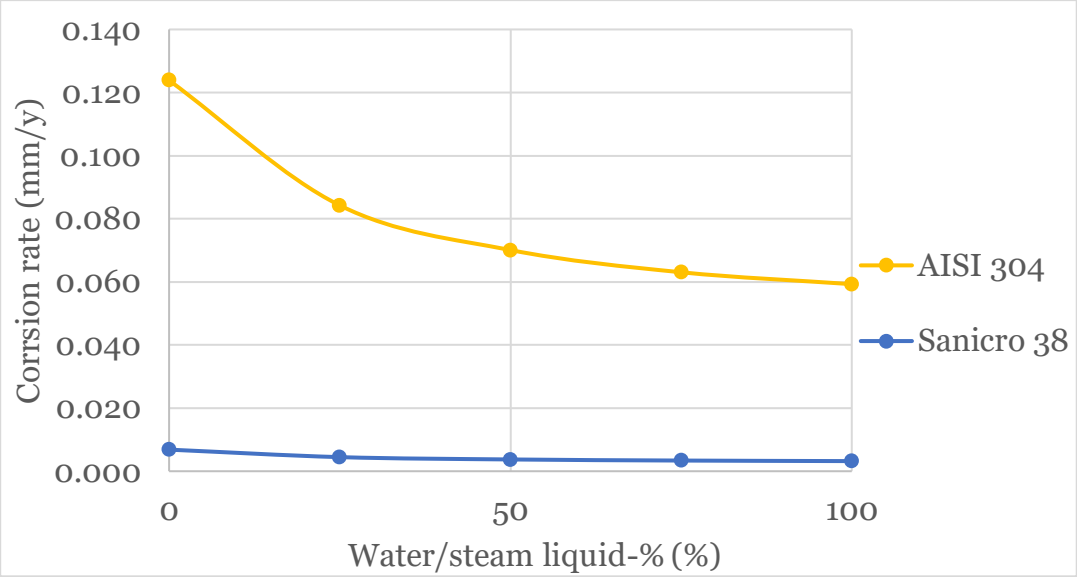

Figure 56. Boiler 1 CR when water/steam mixture liquid-vapor ratio is changed.

Boiler 1 underwent a retrofit in which its furnace size was increased, allowing for a higher DS throughput. Prior to the upgrade, the boiler operated at 3300 tDS/day with a furnace depth of 11.28 m. This older configuration had a significantly lower floor loading of 3.16 MW/m², compared to 3.59 MW/m² post-upgrade. As a result, the average heat flux was reduced from 171 kW/m² to 150 kW/m², effectively decreasing the cladding temperature and eliminating corrosion for both materials under the revised operating conditions.

5.3 Sensitivity analysis

The accuracy and applicability of the developed calculation model are influenced by several key assumptions and limitations. This section summarizes the primary sources of uncertainty and discusses areas requiring further research or refinement.

The model is specifically designed for straight vertical wall tubes and does not account for geometric discontinuities such as bends, tube openings, air ports, or floor tubes. These areas are subject to elevated heat fluxes, enhanced thermal cycling, mechanical stress, and direct smelt contact all of which contribute to accelerated corrosion. Field data consistently show that CRs in these regions are significantly higher than in uniform vertical wall segments.

Because the model assumes uniform, average heat flux and omits local effects, it should not be applied to assess corrosion or deposit growth in these critical high-stress zones.

The vertical heat flux multiplier curve (Figure 41 from Section 4.5) is based on data from Boiler 1 and may not represent other KRBs. Component placement such as the height of black liquor guns and air ports varies significantly among KRBs, affecting the vertical distribution of heat flux. Furthermore, differences in floor loading and furnace geometry result in different average heat flux values. The current model assumes identical heat fluxes across all furnace walls, which oversimplifies reality. Additionally, the upper portion of the heat flux profile was extrapolated based on a mirrored curve from Figure 12 from Section 3.3, as empirical corrosion data was only available up to 20% furnace height. The correlation between floor loading (HHRR) and heat flux is also uncertain. It is derived from a single reference (Viswamoorthy, 2021), and no additional empirical studies were found to support or verify this relationship.

The model assumes a 100% liquid phase inside the wall tubes. In practice, the water/steam mixture ratio changes with elevation in the furnace. While this assumption introduces only a minor error in the lower furnace where the model is primarily intended, the lack of phase distribution data across the wall tube height limits accuracy in higher regions. Furthermore, water/steam distribution likely varies with KRB design and operating conditions.

The model assumes a fixed internal deposit thermal conductivity of 0.3 W/mK, corresponding to low-conductivity impurity deposits. In reality, thermal conductivity varies significantly with deposit composition and temperature. Internal deposit thermal conductivity might change in relation to thickness especially when they are thick and temperature difference between interfaces is huge. Magnetite deposits can exhibit thermal conductivity values around 3 W/mK, which would drastically reduce calculated cladding surface temperatures and corresponding CRs. This was particularly evident in the Boiler 3 case, where a thick deposit (1.18 mm) combined with low thermal conductivity led to an extremely high calculated cladding temperature for CR of 2 mm/y, an unrealistically high value for sustainable operation. However, using conservative conductivity values ensures safety margins in practice. Additionally, thermal conductivity in each layer is currently calculated using the temperature at the cold-side interface. Accuracy could be improved by calculating conductivity at the mid-plane of each material layer, though the impact is likely minimal in the overall model performance.

Corrosion rate functions for AISI 304 and Sanicro 38 were derived primarily from temperature extrapolation. This introduces systematic error, especially

when the extrapolated heat flux multiplier or assumed thermal conductivities are inaccurate. Furthermore, cladding corrosion data is limited and often derived under conditions that differ significantly from the KRB environment. Reproducing KRB-like conditions in laboratory testing is challenging due to the presence of volatile gases, multi-phase reactions, and the influence of internal tube pressure. The model also assumes CR functions are universal, but differences in KRB design, operation, and internal deposit behaviour may require boiler-specific calibration. For instance, selecting the AISI 304 CR value from Boiler 1 over Boiler 2 may introduce error when the model is applied to Boiler 2 conditions. Measured CR values from Pos 1–6 in Boiler 1 deviated slightly from calculated CRs. At lower elevations, calculated CRs tended to be higher, whereas at Position 6, they were lower. This discrepancy suggests localized deviations in heat flux, phase ratio, or internal deposit characteristics not captured by the model.

The model does not account for waterside corrosion resulting from internal deposits and poor water quality. Parameters such as pH, dissolved oxygen, and waterborne impurities contribute to corrosion from the tube interior. Elevated temperatures in carbon steel further reduce corrosion resistance. Although the primary focus is on fireside (smelt- and gas-facing) corrosion, omitting waterside mechanisms could underestimate overall material degradation.

6 Conclusions

The primary objective of this thesis was to develop a predictive calculation model that enables kraft recovery boiler (KRB) operators and manufacturers to assess how internal water-side deposits influence the performance of wall tube cladding materials, specifically AISI 304 and Sanicro 38. The goal was to quantify the relationship between deposit thickness and two key output variables: cladding surface temperature and corrosion rate (CR).

To achieve this, the thesis focused on the following key developments: (i) Establishing a correlation between floor loading and furnace heat flux, enabling the model to be scaled to different KRB designs. (ii) Creating a heat-transfer model to solve the temperature at the tube/deposit interface on the water-side, based on input steam drum pressure and furnace-side heat flux. (iii) Incorporating temperature-dependent thermal conductivity for each material layer (deposits, carbon steel, and claddings) to account for linear conduction effects. (iv) Constructing corrosion functions for both AISI 304 and Sanicro 38 that reflect actual KRB operating conditions, particularly sulfidation at elevated temperatures. (v) Estimating how heat flux is vertically distributed along the furnace height to evaluate corrosion distribution over tube elevations.

Together, these features form a flexible tool that allows users to: (i) Predict the effect of internal deposits on wall tube temperature and corrosion rate. (ii) Assess how corrosion is distributed with furnace height under the assumption of uniform deposit thickness. (iii) Evaluate the suitability of cladding materials across different furnace zones based on thermal and corrosive load.

The results show that even thin layers (~10-20 μm) of low-conductivity, impurity-rich deposits can significantly elevate cladding temperature and accelerate corrosion, particularly in KRBs with high floor loading, elevated heat flux, and high steam drum pressure. For example, a 5-bar reduction in steam drum pressure can significantly lower cladding temperatures and CR but may reduce overall water/steam temperature, affecting process efficiency. If the internal deposits are composed primarily of magnetite, with its higher thermal conductivity (~3 W/mK), significantly thicker deposits can be tolerated without exceeding critical CR thresholds.

The model also demonstrates that high water quality is essential for minimizing deposit growth, especially in high-pressure units. Impurities such as calcium, silicates, and phosphorus readily form insulating layers that not only raise temperatures but also lead to increased localized corrosion, particularly near tube curves and lower furnace elevations. Additionally, the water/steam

vapor ratio has a substantial impact on CR, with a rapid increase in corrosion observed when vapor content exceeds 70%.

The model performs best in the lower 20% of the furnace height, where sulfidation corrosion is most aggressive and validation data are most complete. In these zones typically between the primary air ports and black liquor guns, it is strongly recommended, that high-performance alloys such as Sanicro 38 be used to mitigate corrosion risk. Even moderate deposit formation in this region can lead to rapid overheating and failure if less resistant materials are employed.

Despite its strengths, the model includes simplifying assumptions that limit its accuracy and generalizability: (i) The vertical heat flux distribution is based on a single reference case (Boiler 1) and mirrored extrapolation from Figure 12. (ii) Water/steam is assumed to be 100% liquid throughout the tube, which may underestimate temperature in higher elevations and when calculation model was built. (iii) Deposit thickness is treated as a static input, even though in reality it evolves over time based on water chemistry and operational conditions. (iv) The model does not currently account for complex geometries such as bends, welds, and air ports, which are known to exhibit locally elevated corrosion rates.

To address these limitations, future work should focus on: (i) Expanding the heat flux database across multiple KRBs to improve vertical and wall-specific resolution. (ii) Measuring site-specific values for H_2S concentrations, internal deposit composition and thickness, water/steam phase ratios, and cladding temperature. (iii) Incorporating dynamic deposit growth based on boiler-specific impurity levels and feedwater quality.

For example, chemical cleaning cycle could be calculated using Equation (72)

$$t_c = \frac{x_d}{g_d} \tag{72}$$

where t_c is time between chemical cleaning (y), x_d is thickness of average internal deposits that keeps cladding CR in recommended levels (µm) and g_d is KRB specific deposit grow rate (µm/y), and chemical cleaning recommendations could be embedded directly into model outputs.

Overall, the developed model provides a useful decision-support tool for selecting appropriate cladding materials at different furnace heights, valuating the impacts of water quality and boiler operating parameters on corrosion behaviour and enhancing predictive maintenance planning and improving safety by proactively identifying corrosion risks before failure occurs.

7 Summary

The kraft recovery boiler (KRB) is a critical component in modern pulp mills, simultaneously converting black liquor into high-pressure steam, regenerating cooking chemicals, and reducing environmental emissions. However, the harsh conditions within the furnace, characterized by high heat flux, alkali-rich flue gases, hydrogen sulfide, and molten smelt subject wall tubes to severe corrosion, especially in lower furnace zones. While cladding materials such as AISI 304 and Sanicro 38 are employed to mitigate corrosion, the presence of internal deposits formed due to poor water quality significantly accelerates material degradation.

This thesis, conducted in collaboration with the Finnish and Swedish Recovery Boiler Committees and Aalto University, develops a predictive, physics-based calculation model to estimate the effect of internal deposits on wall tube temperature and corrosion rate (CR). The model integrates several key elements: (i) a correlation between floor loading and furnace-side heat flux, (ii) a multilayer thermal model based on steam pressure and heat flux, (iii) temperature-dependent thermal conductivity functions for key materials, and (iv) empirical corrosion functions for AISI 304 and Sanicro 38 under sulfidation conditions.

The model enables mill engineers to assess how deposit thickness influences wall temperature and CR, and how corrosion is distributed across furnace height. Results indicate that even thin layers (10–20 μm) of low-conductivity internal deposits can elevate tube temperatures significantly, particularly in high-floor loading, heat flux and pressure KRBs, resulting in accelerated corrosion. Magnetite-rich deposits, due to their higher conductivity, allow for greater thickness without exceeding safe limits.

Model accuracy is highest within the lower 20% of the furnace, where sulfidation is most aggressive and field data are most reliable. However, limitations remain due to assumptions about heat flux profiles, static deposit thickness, steam phase behaviour, and exclusion of geometric effects near air ports and bends. Recommendations for future work include improving heat flux correlations across KRB types, measuring site-specific H_2S concentrations and internal deposit properties, and implementing dynamic deposit growth functions based on water quality and time.

Overall, the model provides a valuable decision-support tool for predicting corrosion behaviour, optimizing cladding material selection, and enhancing condition-based maintenance strategies in kraft recovery boilers.

References

Adams, T., (1997). General Characteristics of Kraft Black Liquor Recovery Boilers. In: T. N. Adams, ed. Kraft Recovery Boilers. New York: TAPPI PRESS, pp. 3-38. https://www.tappi.org/content/pdf/member_groups/Pulp/0102B064b.pdf

Alleima. (n.d.). Alleima® 3R12: Seamless tube and pipe—technical datasheet. Retrieved May 29, 2025, from https://www.alleima.com/en/technical-center/material-datasheets/tube-and-pipe-seamless/alleima-3r12/

Alleima. (n.d.). Sanicro® 38 composite tubes for recovery boilers. Retrieved May 29, 2025, from https://www.alleima.com/en/products/tube-pipe-fittings-and-flanges/tubular-products/composite-tubes/sanicro-38-composite-tubes-for-recovery-boilers/

Alleima. (n.d.). Sanicro® 67 for black liquor recovery boilers. Retrieved May 29, 2025, from https://www.alleima.com/en/products/tube-pipe-fittings-and-flanges/tubular-products/composite-tubes/sanicro-67-for-black-liquor-recovery-boilers/

American Metals Co. (n.d.). 304L stainless steel technical data sheet. Retrieved May 28, 2025, from https://metalshims.com/pages/304l-stainless-steel-technical-data-sheet

Andritz. (n.d.). 304L composite tube and Sanicro 38. (Unpublished internal report)

Ansys Innovation Courses. (2020). Lesson 1: Introduction to Fourier's law [PDF]. Ansys, Inc. https://innovationspace.ansys.com/courses/wp-content/uploads/sites/5/2020/03/Lesson-1-Introduction-to-Fouriers-Law.pdf

Bajpai, P. (2017). Properties, composition, and analysis of black liquor (Chap. 2). In Pulp and paper industry (pp. 25–38). Elsevier. https://doi.org/10.1016/B978-0-12-811103-1.00002-4

Barnhart, J. (1997). Occurrences, uses, and properties of chromium. Regulatory toxicology and pharmacology, 26(1), S3-S7.

Bartholomew, R. D. (n.d.). Recovery boiler water treatment (Paper 5-2). In Proceedings of the 2008 TAPPI Kraft Recovery Operations Short Course (KROS). Technical Association of the Pulp and Paper Industry. https://www.tappi.org/content/events/08kros/manuscripts/5-2.pdf

Bergman, T. L., Lavine, A. S., Incropera, F. P., & DeWitt, D. P. (2011). Fundamentals of heat and mass transfer 7E. Chichester, England: John Wiley & Sons. ISBN 13 978-0470-50197-9

Brossard, J. M., Diop, I., Chaucherie, X., Nicol, F., Rapin, C., & Vilasi, M. (2011). Superheater fireside corrosion mechanisms in MSWI plants: Lab-scale study and on-site results. Materials and Corrosion, 62(6), 543-548.

Bryers, R. W. (1996). Fireside slagging, fouling, and high-temperature corrosion of heat-transfer surface due to impurities in steam-raising fuels. Progress in energy and combustion science, 22(1), 29-120.

Cardoso, M., de Oliveira, É. D., & Passos, M. L. (2009). Chemical composition and physical properties of black liquors and their effects on liquor recovery operation in Brazilian pulp mills. Fuel, 88(4), 756-763.

Childs, P. R. N., Greenwood, J. R., & Long, C. A. (1999). Heat flux measurement techniques. Proceedings of the Institution of Mechanical Engineers, Part C: Journal of Mechanical Engineering Science, 213(7), 655-677.

Clay, D. T. (2008). Evaporation principles and black liquor properties. TAPPI Kraft Recovery Short Course, 1-6. https://www.tappi.org/content/events/08kros/manuscripts/3-1.pdf

Corrosion Resistant Alloys. (n.d.). Alloy 825 schedule pipe and tube. Retrieved May 29, 2025, from https://www.cralloys.com/alloys/alloy-825/alloy-825-schedule-pipe-and-tube/

Crowe, D. C., & Cameron, J. H. (1988). Recovery boiler air port corrosion. IPC Technical Paper Series, (299).

Dillon, J. J., Desch, P. B., & Lai, T. S. (2011). The Nalco Water guide to boiler failure analysis (D. J. Flynn, Ed.; 2nd ed.). McGraw-Hill.

Dooley, R. B. (2003). Deposition in boilers–Review of Soviet and Russian literature. EPRI, Paolo Alto, CA, 1004193.

Dwivedi, D., Lepková, K., & Becker, T. (2017). Carbon steel corrosion: a review of key surface properties and characterization methods. RSC advances, 7(8), 4580-4610.

Feng, Z., Fan, X., Wang, Z., Yu, Y., Chen, L., Du, Y., & Dong, L. (2021). Corrosion behavior and passive film composition of alloy 825 in high

temperature and high H2S-CO2 containing environment. Frontiers in Materials, 8, 728898.

Frederick Jr, W. J., & Hupa, M. (1993). Combustion properties of kraft black liquors (No. DOE/CE/40936-T1). USDOE Assistant Secretary for Energy Efficiency and Renewable Energy, Washington, DC (United States). Office of Industrial Technologies; Tampella Power, Tampere (Finland); Ministry of Trade and Industry, Helsinki (Finland). Energy Dept.; Oregon State Univ., Corvallis, OR (United States); Aabo Akademi, Turku (Finland).

García Pérez, M., Vakkilainen, E., & Hyppänen, T. (2016). Unsteady CFD analysis of kraft recovery boiler fly-ash trajectories, sticking efficiencies and deposition rates with a mechanistic particle rebound-stick model. Fuel., 181, 408–420. https://doi.org/10.1016/j.fuel.2016.05.004

Gillenwater, M., Woodfield, M., Simmons, T., McCormick, M., Camobreco, V., Hockstad, L., & Upton, B. (2005). Calculation tool for direct emissions from stationary combustion. World Resources Institute, Washington DC. https://ghgprotocol.org/sites/default/files/2023-02/Stationary_Combustion_Guidance_final_1_0.pdf

Hamaguchi, M., & Vakkilainen, E. K. (2011). Influence of chlorine and potassium on operation and design of chemical recovery equipment. TAPPI JOURNAL, 10(1), 33-39.

Hupa, M. (2007). Recovery boiler chemical principles. TAPPI Kraft Recover. Course, 2007(2). https://www.tappi.org/content/events/08kros/manuscripts/4-4.pdf

Hupa, M., & Frederick, W. J. (n.d.). Combustion of black liquor droplets [Conference paper]. TAPPI Kraft Recovery Operations Short Course. https://www.tappi.org/content/events/08kros/manuscripts/4-2.pdf

IEA Bioenergy. (2007). Black liquor gasification: Summary and conclusions (ExCo:2007:03). International Energy Agency Bioenergy Programme. https://www.ieabioenergy.com/wp-content/uploads/2013/10/Black-Liquor-Gasification-summary-and-conclusions1.pdf

Inkinen, S., Haaga, K., Wahlman, T., & Nieminen, A. (2024). Tulipesän pohjan putkivuoto huhtikuussa 2024. Valmet. (Unpublished internal report)

International Flame Research Foundation. (n.d.). What is black liquor? IFRF Online Handbook. Retrieved May 29, 2025, from https://ifrf.net/research/handbook/what-is-black-liquor/

Isberg, P.-A. O. (2018). Inspection Report TS&I: 010/18. Valmet. (Unpublished internal report)

Jaroudi, E., Stretenovic, I., Evans, G., & Tran, H. (2018). Factors affecting particulate removal efficiency of kraft recovery boiler electrostatic precipitators: a technical review. https://utoronto.scholaris.ca/server/api/core/bitstreams/9325f634-4222-4764-aec6-96c8d6056049/content

Jörgensen, H. (2018). Laboratory report 271173. Valmet. (Unpublished internal report)

Karhula, T. (2022). Testausseloste [Test report]. Metlab Oy. (Unpublished internal report)

Karjunen, T. (2009). Soodakattilan seinäputken sisäpuoliset kerrostumat. Boildec Oy. (Unpublished internal report)

Kawahara, Y. (2006). Evaluation of high-temperature corrosion life using temperature gradient corrosion test with thermal cycle component in waste combustion environments. Materials and Corrosion, 57(1), 60-72.

Keiser, J. R., Sarma, G. B., Wang, X. L., Hubbard, C. R., Swindeman, R. W., Singbeil, D. L., & Singh, P. M. (2001). Why do kraft recovery boiler composite floor tubes crack?. Tappi journal, 84(8), 48-48.

Khaleel, O. J., Ismail, F. B., Ibrahim, T. K., & bin Abu Hassan, S. H. (2022). Energy and exergy analysis of the steam power plants: A comprehensive review on the Classification, Development, Improvements, and configurations. Ain Shams Engineering Journal, 13(3), 101640.

Khodahami, M. (2024). Statusbedömning på tubprover från panna SP 6. Dekra. (Unpublished internal report)

Kiwa Inspecta. (2014). Teknisk rapport Nr. 21-1021623-118. (Unpublished internal report)

Kurganov, V. A. (2011, February 2). Heat transfer coefficient. Thermopedia. https://www.thermopedia.com/content/841/
https://doi.org/10.1615/AtoZ.h.heat_transfer_coefficient

Li, L., Yan, J., Xiao, J., Sun, L., Fan, H., & Wang, J. (2021). A comparative study of corrosion behavior of S-phase with AISI 304 austenitic stainless steel in H2S/CO2/Cl-media. Corrosion Science, 187, 109472.

Lienhard, J. H., V, & Lienhard, J. H., IV. (2024). A heat transfer textbook (6th ed., Version 6.00). Phlogiston Press. https://ahtt.mit.edu/wp-content/uploads/2024/04/AHTTv600.pdf

Liikola, E. (2015). Soodakattilavauriot. Stora Enso. (Unpublished internal report)

Lin, B., & Eng, P. (2007). Collecting and burning noncondensible gases. TAPPI Kraft Recovery Course, 2007, 295-305. https://www.tappi.org/content/events/08kros/manuscripts/3-6.pdf

Lind, T., Hokkinen, J., Jokiniemi, J. K., Hillamo, R., Makkonen, U., Raukola, A., ... & Saviharju, K. (2006). Electrostatic precipitator performance and trace element emissions from two kraft recovery boilers. Environmental science & technology, 40(2), 584-589.

Llamas, P., Dominguéz, T., Vargas, J. M., Llamas, J., Franco, J. M., & Llamas, A. (2007). A novel viscosity reducer for kraft process black liquors with a high dry solids content. Chemical Engineering and Processing: Process Intensification, 46(3), 193-197.

Lundborg, A. (2005). Simulation of the flue gas flow through the superheater in a recovery boiler. School of Chemical Science and Engineering. KTH-Royal Institute of Technology, Stockholm Sweden. Master of Science Thesis. 93.

Mäkipää, M., Oksa, M., & Pohjanne, P. (2001). Corrosion testing of high-nickel alloy composite tube materials in simulated recovery boiler lower furnace conditions. In 10th International Symposium On corrosion in the Pulp and Paper Industry, ISCPPI (pp. 73-88). VTT Technical Research Centre of Finland.

Metso Flow Control Inc. (2019). Recovery boiler valves: Application report 2611/09/01 EN. https://www.awc-inc.com/wp-content/uploads/2021/02/Recovery-Boiler-Valves.pdf

Molgaard, J., & Smeltzer, W. W. (1971). Thermal conductivity of magnetite and hematite. Journal of applied physics, 42(9), 3644-3647.

NASA Glenn Research Center. (n.d.). Mass flow rate. NASA. Retrieved May 29, 2025, from https://www.grc.nasa.gov/www/k-12/BGP/mflow.html

Nickel Development Institute. (n.d.). High-temperature characteristics of stainless steels (Designers' Handbook Series No. 9004). Nickel Institute.

https://nickelinstitute.org/media/1699/high_temperaturecharac-teristicsofstainlesssteel_9004_.pdf

Niemi, J., Engblom, M., Laurén, T., Yrjas, P., Lehmusto, J., Hupa, M., & Lindberg, D. (2021). Superheater deposits and corrosion in temperature gradient–Laboratory studies into effects of flue gas composition, initial deposit structure, and exposure time. Energy, 228, 120494.

Nilsson, J. (2023). SODAPANNA SP6 Inspektionsrapport IU 2023. Dekra. (Unpublished internal report)

Nimmervoll, M., Mori, G., Hönig, S., & Haubner, R. (2022). High-temperature corrosion of austenitic alloys in HCl and H2S containing atmospheres under reducing conditions. Corrosion science, 200, 110214.

NIST Chemistry WebBook. (n.d.). Thermophysical properties of saturated water. National Institute of Standards and Technology. Retrieved May 14, 2025, from https://webbook.nist.gov/cgi/fluid.cgi?PLow=60&PHigh=120&PInc=1&Digits=5&ID=C7732185&Action=Load&Type=SatT&TUnit=C&Punit=bar&DUnit=kg%2Fm3&HUnit=kJ%2Fkg&WUnit=m%2Fs&VisUnit=Pa*s&STUnit=N%2Fm&RefState=DEF

Pettersson, K.; Mahmoudkhani, M.; von Schenck, A. Opportunities for Biorefineries in the Pulping Industry. In Systems Perspectives on Biorefineries; Sandén, B., Pettersson, K., Eds.; Chalmers University of Technology: Göteborg, Sweden, 2014. https://publications.lib.chalmers.se/records/fulltext/185714/local_185714.pdf

Pohjanne, P. (2013). Characterisation of probe test samples exposed to BLRB lower furnace environments. VTT. (Unpublished internal report)

Poon, W., Barham, D., & Tran, H. (1993). Formation of acidic sulfates in kraft recovery boilers. Tappi journal, 76(7), 187-193.

Puustinen, M. (2015). Sustainability aspects of crude sulfate soap acidulation to crude tall oil within the EU biofuel policy framework (Master's thesis, Aalto University School of Chemical Technology). Aalto University. (83)

Robinson, A. L., Buckley, S. G., & Baxter, L. L. (1998, January). In situ measurements of the thermal conductivity of ash deposits. In Symposium (International) on Combustion (Vol. 27, No. 2, pp. 1727-1735). Elsevier.

Robinson, A. L., Buckley, S. G., Yang, N., & Baxter, L. L. (2001). Experimental measurements of the thermal conductivity of ash deposits: Part 2. Effects of sintering and deposit microstructure. Energy & Fuels, 15(1), 75-84.

Saari, J., Sermyagina, E., Kaikko, J., Haider, M., Hamaguchi, M., & Vakkilainen, E. (2021). Evaluation of the Energy Efficiency Improvement Potential through Back-End Heat Recovery in the Kraft Recovery Boiler. Energies., 14(6). https://doi.org/10.3390/en14061550

Sandvik Materials Technology. (n.d.). Sandvik Sanicro® 38/4L7 composite tube for black-liquor-recovery and other boilers [Product brochure]. Scribd. https://www.scribd.com/document/408276933/SANICRO-38-pdf

Schaal, E., David, N., Panteix, P. J., Rapin, C., Vilasi, M., Mathieu, S., ... & Maad, F. (2016). Effect of zinc chloride in ash in oxidation kinetics of Ni-based and Fe-based alloys. Oxidation of Metals, 85(5), 547-563.

Steel Tubes India. (n.d.). SA 210 Grade A1 boiler tube. Retrieved May 28, 2025, from https://www.steeltubesindia.net/sa-210-grade-a1-boiler-tube.html

Stewart, M., & Arnold, K. (2013). Surface production operations: Design of oil-handling facilities (3rd ed.). Gulf Professional Publishing. https://www.sciencedirect.com/book/9780123822079/surface-production-operations

Suhr, M., Klein, G., Kourti, I., Gonzalo, M. R., Santonja, G. G., Roudier, S., & Sancho, L. D. (2015). Best available techniques (BAT) reference document for the production of pulp, paper and board. Eur. Comm, 906(10.2791), 370629.

Tan, G. (2000). Cooling characteristics and thermal properties of kraft recovery boiler smelt (Doctoral dissertation). University of Toronto. 150

Tavares, R. M. & Karjunen, T. (2020). Advances in boiler tube internal deposit monitoring and guidelines to determine the need for recovery boiler chemical cleaning. International Chemical Recovery Conference, May, 18-21, 2020, Santos, São Paulo, Brazil.

Tran, H. N., Barham, D., & Hupa, M. (1988). Fireside corrosion in kraft-recovery boilers: An overview. Materials Performance, 27(7), 40–46. https://www.researchgate.net/publication/255546278

Vainio, E., Brink, A., Demartini, N., Hupa, M., Vesala, H., Tormonen, K., & Kajolinna, T. (2010). In-furnace measurement of sulphur and nitrogen species in a recovery boiler. Journal of Pulp and Paper Science, 36(3), 135.

Vakkilainen, E. (2005). Kraft recovery boilers–Principles and practice. Suomen Soodakattilayhdistys r.y. Valopaino Oy, Helsinki, Finland. 246

Vakkilainen, E. K. (1996). Recovery boiler adjustable air system. In Black Liquor Recovery Boiler Annual Conference, Atlanta, USA (pp. 1-14).

Vakkilainen, E. K. (2016). Steam Generation from biomass: Construction and design of Large Boilers. Oxford, England: Butterworth-Heinemann.

Viswamoorthy, R. (2021). Lower furnace heat flux data. Valmet. (Unpublished internal report)

Wessel, R. (2008). Black liquor sprays. Paper presented at the 2008 Kraft Recovery Operations Short Course (KROS), Technical Association of the Pulp and Paper Industry (TAPPI). Retrieved from https://www.tappi.org/content/events/08kros/handouts/4-3.pdf

Winterton, R. H. (1998). Where did the Dittus and Boelter equation come from?. International journal of heat and mass transfer, 41(4-5), 809-810.

Yli-Olli, S., Pohjanne, P., Heikinheimo, L., Kinnunen, T., & Pankakoski, P. H. (2007, June). Sulphidation behaviour of advanced materials for elevated kraft recovery boiler conditions. In VTT SYMPOSIUM (Vol. 247, p. 135). VTT; 1999.

Appendix 1. Chemical formulas

$Ca(HCO_3)_2$	Calcium bicarbonate
$Ca(OH)_2$	Slacked lime
$CaCO_3$	Lime mud
CaO	Quicklime
$(CH_3)_2S$	Dimethyl sulfide
CH_3OH	Methanol
CH_3SSCH_3	Dimethyl disulfide
CH_4	Methane
CH_4S	Methyl mercaptan
CO	Carbon monoxide
CO_2	Carbon dioxide
COS	Carbonyl sulfide
Fe_2O_3	Hematite
Fe_3O_4	Magnetite
$FeCl_2$	Iron(II) chloride
FeO	Iron oxide
FeS	Iron sulfide
H_2O	Water
H_2S	Hydrogen sulfide
HCl	Hydrogen chloride
K_2CO_3	Potassium carbonate
K_2S	Potassium sulfide
K_2SO_4	Potassium sulfate
KCl	Potassium chloride
KOH	Potassium hydroxide
Na_2CO_3	Sodium carbonate
Na_2O	Sodium oxide
Na_2S	Sodium sulfide
$Na_2S{\cdot}9H_2O$	Hydrated sodium sulfide
$Na_2S_2O_3$	Sodium thiosulfate
Na_2SO_4	Sodium sulfate
$NaCl$	Sodium chloride
$NaHSO_3$	Sodium bisulfate
$NaHSO_4$	Sodium bisulfate
$NaOH$	Sodium hydroxide
NH_3	Ammonia
SO_2	Sulfur dioxide
SO_3	Sulfur trioxide

Appendix 2. Saturated water/steam mixture properties 60-150 bar (NIST, n.d.)

Both		Liquid				Vapor			
P	T_w	ρ_w	μ_w ($\times 10^{-05}$)	c_w	k_w	ρ_w	μ_w ($\times 10^{-05}$)	c_w	k_w
(bar)	(^{0}C)	(kg/m^3)	(Pa·s)	(J/kgK)	(W/mK)	(kg/m^3)	(Pa·s)	(J/kgK)	(W/mK)
60	275.58	758.00	9.53	5211.60	0.59	30.82	1.84	4879.40	0.06
61	276.67	756.13	9.49	5229.90	0.59	31.38	1.85	4925.30	0.06
62	277.73	754.27	9.45	5248.40	0.58	31.94	1.85	4971.50	0.06
63	278.79	752.42	9.40	5267.00	0.58	32.50	1.86	5018.20	0.06
64	279.83	750.58	9.36	5285.80	0.58	33.07	1.86	5065.30	0.06
65	280.86	748.75	9.32	5304.80	0.58	33.64	1.87	5112.70	0.06
66	281.87	746.93	9.28	5323.90	0.58	34.21	1.87	5160.60	0.06
67	282.88	745.11	9.24	5343.30	0.58	34.79	1.88	5208.90	0.06
68	283.87	743.31	9.20	5362.80	0.58	35.36	1.88	5257.70	0.06
69	284.86	741.51	9.16	5382.50	0.57	35.94	1.88	5306.90	0.06
70	285.83	739.72	9.13	5402.50	0.57	36.53	1.89	5356.60	0.06
71	286.79	737.94	9.09	5422.60	0.57	37.11	1.89	5406.80	0.06
72	287.74	736.17	9.05	5443.00	0.57	37.70	1.90	5457.40	0.06
73	288.68	734.40	9.02	5463.50	0.57	38.29	1.90	5508.60	0.06
74	289.61	732.64	8.98	5484.30	0.57	38.88	1.91	5560.30	0.07
75	290.54	730.88	8.95	5505.40	0.57	39.48	1.91	5612.50	0.07
76	291.45	729.14	8.91	5526.60	0.57	40.08	1.92	5665.30	0.07
77	292.35	727.39	8.88	5548.10	0.56	40.68	1.92	5718.70	0.07
78	293.25	725.66	8.84	5569.80	0.56	41.29	1.92	5772.60	0.07
79	294.13	723.92	8.81	5591.80	0.56	41.90	1.93	5827.10	0.07
80	295.01	722.20	8.77	5614.10	0.56	42.51	1.93	5882.30	0.07
81	295.88	720.47	8.74	5636.60	0.56	43.12	1.94	5938.10	0.07
82	296.74	718.76	8.71	5659.40	0.56	43.74	1.94	5994.50	0.07
83	297.59	717.04	8.68	5682.40	0.56	44.36	1.95	6051.50	0.07
84	298.43	715.34	8.64	5705.80	0.56	44.99	1.95	6109.30	0.07
85	299.27	713.63	8.61	5729.40	0.55	45.61	1.95	6167.70	0.07
86	300.10	711.93	8.58	5753.30	0.55	46.24	1.96	6226.90	0.07
87	300.92	710.23	8.55	5777.50	0.55	46.88	1.96	6286.80	0.07
88	301.74	708.54	8.52	5802.10	0.55	47.52	1.97	6347.40	0.07
89	302.54	706.85	8.49	5826.90	0.55	48.16	1.97	6408.80	0.07
90	303.34	705.16	8.46	5852.10	0.55	48.80	1.98	6471.00	0.07
91	304.14	703.48	8.43	5877.60	0.55	49.45	1.98	6534.00	0.07
92	304.93	701.80	8.40	5903.50	0.55	50.11	1.98	6597.80	0.07
93	305.71	700.12	8.37	5929.70	0.54	50.76	1.99	6662.50	0.07
94	306.48	698.44	8.34	5956.20	0.54	51.42	1.99	6728.00	0.08

Both		Liquid				Vapor			
P	T_w	ρ_w	μ_w ($\times 10^{-05}$)	c_w	k_w	ρ_w	μ_w ($\times 10^{-05}$)	c_w	k_w
(bar)	(^oC)	(kg/m^3)	(Pa·s)	(J/kgK)	(W/mK)	(kg/m^3)	(Pa·s)	(J/kgK)	(W/mK)
95	307.25	696.77	8.31	5983.20	0.54	52.09	2.00	6794.50	0.08
96	308.01	695.09	8.28	6010.50	0.54	52.75	2.00	6861.80	0.08
97	308.77	693.42	8.26	6038.20	0.54	53.42	2.01	6930.10	0.08
98	309.52	691.76	8.23	6066.30	0.54	54.10	2.01	6999.30	0.08
99	310.26	690.09	8.20	6094.80	0.54	54.78	2.02	7069.60	0.08
100	311.00	688.42	8.17	6123.70	0.54	55.46	2.02	7140.80	0.08
101	311.73	686.76	8.14	6153.00	0.53	56.15	2.02	7213.10	0.08
102	312.46	685.10	8.12	6182.80	0.53	56.84	2.03	7286.50	0.08
103	313.18	683.43	8.09	6213.10	0.53	57.54	2.03	7360.90	0.08
104	313.89	681.77	8.06	6243.80	0.53	58.24	2.04	7436.50	0.08
105	314.60	680.11	8.04	6274.90	0.53	58.95	2.04	7513.30	0.08
106	315.31	678.45	8.01	6306.60	0.53	59.66	2.05	7591.20	0.08
107	316.01	676.79	7.98	6338.70	0.53	60.37	2.05	7670.30	0.08
108	316.70	675.13	7.96	6371.40	0.53	61.09	2.06	7750.70	0.08
109	317.39	673.47	7.93	6404.60	0.52	61.81	2.06	7832.40	0.08
110	318.08	671.81	7.90	6438.30	0.52	62.54	2.06	7915.40	0.08
111	318.76	670.15	7.88	6472.60	0.52	63.27	2.07	7999.80	0.08
112	319.43	668.49	7.85	6507.50	0.52	64.01	2.07	8085.50	0.09
113	320.11	666.83	7.83	6543.00	0.52	64.76	2.08	8172.70	0.09
114	320.77	665.17	7.80	6579.00	0.52	65.50	2.08	8261.40	0.09
115	321.43	663.51	7.78	6615.70	0.52	66.26	2.09	8351.60	0.09
116	322.09	661.85	7.75	6653.00	0.52	67.02	2.09	8443.40	0.09
117	322.74	660.18	7.73	6691.00	0.52	67.78	2.10	8536.80	0.09
118	323.39	658.52	7.70	6729.70	0.51	68.55	2.10	8631.80	0.09
119	324.04	656.85	7.68	6769.00	0.51	69.33	2.11	8728.50	0.09
120	324.68	655.18	7.65	6809.10	0.51	70.11	2.11	8827.00	0.09
121	325.31	653.51	7.63	6849.90	0.51	70.89	2.12	8927.30	0.09
122	325.94	651.84	7.60	6891.60	0.51	71.68	2.12	9029.50	0.09
123	326.57	650.16	7.58	6933.90	0.51	72.48	2.13	9133.60	0.09
124	327.19	648.49	7.55	6977.20	0.51	73.29	2.13	9239.60	0.09
125	327.81	646.81	7.53	7021.20	0.51	74.10	2.14	9347.80	0.09
126	328.43	645.13	7.50	7066.10	0.50	74.91	2.14	9458.00	0.10
127	329.04	643.44	7.48	7112.00	0.50	75.74	2.15	9570.40	0.10
128	329.65	641.75	7.46	7158.80	0.50	76.57	2.15	9685.00	0.10
129	330.25	640.06	7.43	7206.50	0.50	77.40	2.16	9802.00	0.10
130	330.85	638.37	7.41	7255.20	0.50	78.25	2.16	9921.30	0.10
131	331.45	636.67	7.39	7305.00	0.50	79.09	2.17	10043.00	0.10
132	332.04	634.97	7.36	7355.90	0.50	79.95	2.17	10168.00	0.10

Both		Liquid				Vapor			
P	T_w	ρ_w	μ_w ($\times 10^{-05}$)	c_w	k_w	ρ_w	μ_w ($\times 10^{-05}$)	c_w	k_w
(bar)	(^oC)	(kg/m^3)	(Pa·s)	(J/kgK)	(W/mK)	(kg/m^3)	(Pa·s)	(J/kgK)	(W/mK)
133	332.63	633.27	7.34	7407.80	0.50	80.81	2.18	10295.00	0.10
134	333.22	631.56	7.31	7460.90	0.50	81.69	2.18	10424.00	0.10
135	333.80	629.85	7.29	7515.30	0.49	82.56	2.19	10557.00	0.10
136	334.38	628.13	7.27	7570.80	0.49	83.45	2.19	10692.00	0.10
137	334.96	626.41	7.24	7627.70	0.49	84.34	2.20	10831.00	0.11
138	335.53	624.69	7.22	7685.90	0.49	85.24	2.20	10973.00	0.11
139	336.10	622.95	7.20	7745.50	0.49	86.15	2.21	11118.00	0.11
140	336.67	621.22	7.17	7806.60	0.49	87.07	2.21	11266.00	0.11
141	337.23	619.48	7.15	7869.20	0.49	87.99	2.22	11418.00	0.11
142	337.79	617.73	7.13	7933.40	0.49	88.93	2.22	11573.00	0.11
143	338.35	615.98	7.10	7999.30	0.49	89.87	2.23	11733.00	0.11
144	338.90	614.22	7.08	8066.80	0.48	90.82	2.24	11896.00	0.11
145	339.45	612.45	7.06	8136.20	0.48	91.78	2.24	12063.00	0.11
146	340.00	610.68	7.03	8207.50	0.48	92.75	2.25	12235.00	0.11
147	340.54	608.90	7.01	8280.70	0.48	93.73	2.25	12410.00	0.12
148	341.08	607.11	6.99	8356.00	0.48	94.72	2.26	12591.00	0.12
149	341.62	605.32	6.96	8433.50	0.48	95.72	2.27	12776.00	0.12
150	342.16	603.52	6.94	8513.20	0.48	96.73	2.27	12967.00	0.12

Appendix 3. Boiler 1 cladding AISI 304 thickness changes 2023-2024 Pos 1

Tube	2023	2024	Tube	2023	2024	Tube	2023	2024	Tube	2023	2024	Tube	2023	2024	Tube	2023	2024
1	1.64	1.62	33	1.10	1.04	65	0.71	0.74	97	0.93	0.97	129	1.14	1.09	161	1.52	1.49
2	1.43	1.39	34	1.03	1.00	66	0.84	0.89	98	0.87	0.87	130	1.13	1.07	162	1.56	1.54
3	1.44	1.43	35	0.98	0.96	67	0.70	0.75	99	1.10	1.12	131	1.17	1.09	163	1.58	1.49
4	1.61	1.54	36	0.97	0.97	68	1.51	1.47	100	0.95	0.94	132	0.97	0.94	164	1.59	1.55
5	1.27	1.23	37	0.96	0.91	69	0.77	0.72	101	1.58	1.55	133	1.10	1.05	165	1.62	1.58
6	1.38	1.23	38	0.96	0.93	70	0.74	0.68	102	0.90	0.90	134	1.03	0.96	166	1.52	1.53
7	1.38	1.29	39	0.94	0.87	71	0.76	1.46	103	0.84	0.93	135	1.13	1.09	167	1.61	1.58
8	1.35	1.29	40	0.95	0.92	72	1.51	1.47	104	1.05	1.07	136	1.02	0.98	168	1.62	1.63
9	1.30	1.26	41	0.90	0.89	73	1.74	1.66	105	1.02	1.05	137	1.14	1.09	169	1.59	1.51
10	1.30	1.26	42	0.92	0.93	74	1.51	1.50	106	1.01	0.97	138	1.02	0.99	170	1.72	1.65
11	1.41	1.34	43	0.92	0.90	75	0.95	0.94	107	1.00	1.01	139	1.26	1.21	171	1.65	1.57
12	1.24	1.30	44	0.98	0.98	76	0.85	0.83	108	1.00	0.97	140	1.25	1.18	172	1.62	1.58
13	1.40	1.36	45	0.82	0.76	77	1.56	1.61	109	0.89	0.95	141	1.53	1.46	173	1.59	1.55
14	1.39	1.37	46	1.00	0.98	78	0.91	0.92	110	0.90	0.95	142	1.60	1.60	174	1.64	1.60
15	1.40	1.43	47	1.51	1.48	79	0.83	0.85	111	0.98	0.95	143	1.61	1.55	175	1.75	1.70
16	1.50	1.45	48	1.47	1.45	80	0.81	0.84	112	0.90	0.89	144	1.50	1.46	176	1.81	1.72
17	1.54	1.50	49	1.68	1.59	81	0.96	0.98	113	0.96	0.95	145	1.59	1.52	177	1.65	1.55
18	1.53	1.47	50	1.45	1.50	82	0.72	0.71	114	0.93	0.89	146	1.61	1.51	178	1.80	1.71
19	1.49	1.49	51	0.96	0.95	83	0.74	0.74	115	0.99	0.97	147	1.56	1.49	179	1.66	1.62
20	1.60	1.54	52	0.85	0.80	84	0.87	0.90	116	1.06	1.06	148	1.51	1.43	180	1.61	1.53
21	1.46	1.46	53	0.97	0.94	85	0.77	0.81	117	1.05	1.04	149	1.54	1.52	181	1.61	1.51
22	1.49	1.50	54	0.94	0.89	86	0.92	0.88	118	1.09	1.08	150	1.61	1.60	182	1.63	1.56
23	1.60	1.62	55	0.80	0.80	87	0.86	0.86	119	1.10	1.07	151	1.65	1.62	183	1.75	1.72
24	1.37	1.38	56	0.80	0.75	88	0.92	0.92	120	1.18	1.12	152	1.50	1.45	184	1.61	1.48
25	1.57	1.51	57	0.88	0.80	89	0.83	0.83	121	1.17	1.15	153	1.52	1.50	185	1.71	1.57
26	1.41	1.36	58	0.93	0.84	90	0.82	0.83	122	1.25	1.25	154	1.68	1.60	186	1.62	1.50
27	1.47	1.42	59	0.70	0.65	91	1.72	0.71	123	1.04	1.08	155	1.56	1.47	187	1.62	1.54
28	1.31	1.20	60	0.65	0.68	92	0.85	0.84	124	1.10	1.10	156	1.53	1.46	188	1.70	1.61
29	1.13	1.16	61	0.72	0.64	93	1.07	1.06	125	1.17	1.14	157	1.60	1.56	189	1.32	1.23
30	1.15	1.10	62	0.63	0.69	94	1.10	1.07	126	1.14	1.10	158	1.53	1.43	190	1.04	1.03
31	1.08	1.09	63	0.94	0.87	95	1.00	0.92	127	1.10	1.07	159	1.71	1.68	191	1.22	1.15
32	1.14	1.15	64	0.72	0.64	96	0.95	0.95	128	1.05	1.01	160	1.58	1.48	192	1.02	1.00

Appendix 4. Boiler 1 cladding AISI 304 thickness changes 2023-2024 Pos 2

Tube	2023	2024	Tube	2023	2024	Tube	2023	2024	Tube	2023	2024	Tube	2023	2024	Tube	2023	2024
1	1.61	1.58	33	1.22	1.19	65	0.83	0.77	97			129	1.21	1.24	161	1.53	1.45
2	1.46	1.45	34	1.21	1.10	66	1.07	0.99	98			130	1.25	1.21	162	1.57	1.55
3	1.42	1.37	35	1.08	1.10	67	0.90	0.88	99	1.53	1.44	131	1.21	1.21	163	1.55	1.51
4	1.47	1.44	36	1.08	1.07	68	1.57	1.58	100	1.61	1.61	132	1.08	1.07	164	1.57	1.46
5	1.26	1.17	37	1.12	1.04	69	1.57	1.58	101	1.59	1.56	133	1.18	1.16	165	1.61	1.57
6	1.39	1.32	38	1.17	1.11	70	1.42	1.34	102	1.11	1.07	134	1.09	1.11	166	1.52	1.55
7	1.39	1.33	39	1.15	1.09	71		1.49	103	1.12	1.08	135	1.13	1.14	167	1.55	1.52
8	1.42	1.36	40	1.22	1.14	72		1.57	104	1.22	1.23	136	1.06	1.07	168		1.65
9	1.33	1.32	41	1.21	1.14	73		1.65	105	1.15	1.19	137	1.15	1.09	169		1.60
10	1.40	1.35	42	1.33	1.20	74		1.59	106	1.11	1.07	138	0.98	0.96	170		1.60
11	1.48	1.46	43	1.61	1.59	75	1.50	1.54	107	1.14	1.14	139	1.19	1.17	171		1.61
12	1.43	1.42	44	1.57	1.55	76	1.57	1.54	108	1.14	1.12	140	1.22	1.14	172	1.55	1.53
13	1.46	1.45	45	1.39	1.35	77	1.64	1.59	109	1.11	1.11	141	1.51	1.49	173	1.62	1.52
14	1.45	1.51	46		1.39	78	1.16	1.10	110	1.13	1.12	142	1.62	1.59	174	1.65	1.61
15	1.48	1.51	47		1.48	79	1.14	1.03	111	1.20	1.12	143	1.59	1.56	175	1.68	1.64
16	1.50	1.53	48		1.50	80	1.01	0.97	112	1.05	1.04	144		1.59	176	1.71	1.71
17	1.66	1.60	49		1.51	81	1.26	1.20	113	1.16	1.17	145		1.65	177	1.60	1.58
18	1.53	1.54	50	1.39	1.39	82	0.96	0.89	114	1.08	1.08	146		1.55	178	1.75	1.71
19	1.61	1.64	51	1.43	1.44	83	0.93	0.87	115	1.14	1.15	147		1.45	179	1.62	1.61
20	1.64	1.63	52	1.47	1.48	84	1.11	0.99	116	1.60	1.61	148	1.47	1.47	180	1.63	1.58
21	1.41	1.54	53	1.19	1.03	85	0.96	0.94	117	1.60	1.61	149	1.56	1.46	181	1.70	1.70
22		1.53	54	1.10	1.04	86	1.05	0.99	118	1.58	1.55	150	1.56	1.55	182	1.63	1.62
23		1.51	55	1.00	0.90	87	1.08	1.07	119		1.61	151	1.67	1.60	183	1.65	1.67
24		1.30	56	0.93	0.86	88	1.31	1.27	120		1.58	152	1.54	1.50	184	1.55	1.53
25		1.23	57	0.98	0.92	89	1.04	1.04	121		1.65	153	1.58	1.45	185	1.68	1.61
26	1.48	1.54	58	0.98	0.89	90	1.03	1.01	122		1.50	154	1.68	1.56	186	1.62	1.58
27	1.59	1.52	59	0.82	0.76	91	1.07	1.08	123	1.39	1.44	155	1.54	1.48	187	1.73	1.63
28	1.52	1.27	60	0.89	0.76	92	1.64	1.60	124	1.73	1.71	156	1.55	1.49	188	1.65	1.60
29	1.26	1.22	61	0.81	0.77	93	1.61	1.61	125	1.60	1.55	157	1.60	1.47	189	1.69	1.25
30	1.25	1.19	62	0.90	0.77	94	1.45	1.47	126	1.29	1.28	158	1.65	1.58	190	1.20	1.06
31	1.20	1.14	63	1.02	0.95	95			127	1.19	1.17	159	1.72	1.61	191	1.37	1.23
32	1.30	1.25	64	0.91	0.81	96			128	1.27	1.22	160	1.65	1.60	192	1.20	1.17

Appendix 5. Boiler 1 cladding AISI 304 thickness changes 2023-2024 Pos 3

Tube	2023	2024	Tube	2023	2024	Tube	2023	2024	Tube	2023	2024	Tube	2023	2024	Tube	2023	2024
1	1.54	1.56	33	1.35	1.29	65	1.11	1.01	97		1.45	129	1.36	1.30	161	1.53	1.52
2	1.46	1.47	34	1.32	1.26	66	1.16	1.15	98		1.40	130	1.39	1.34	162	1.61	1.62
3	1.42	1.43	35	1.26	1.22	67	1.04	1.05	99	1.62	1.62	131	1.38	1.31	163	1.56	1.51
4	1.53	1.44	36	1.28	1.21	68	1.59	1.59	100	1.61	1.62	132	1.26	1.65	164	1.57	1.56
5	1.22	1.19	37	1.28	1.25	69	1.61	1.62	101	1.58	1.62	133	1.25	1.24	165	1.61	1.58
6	1.34	1.31	38	1.32	1.26	70	1.58	1.59	102	1.20	1.21	134	1.18	1.15	166	1.54	1.55
7	1.34	1.30	39	1.27	1.28	71		1.44	103	1.21	1.20	135	1.22	1.20	167	1.52	1.54
8	1.36	1.36	40	1.31	1.30	72		1.50	104	1.32	1.31	136	1.15	1.13	168		1.43
9	1.33	1.34	41	1.28	1.28	73		1.55	105	1.28	1.28	137	1.17	1.16	169		1.45
10	1.41	1.42	42	1.30	1.34	74		1.51	106	1.18	1.18	138	1.15	1.11	170		1.50
11	1.50	1.51	43	1.58	1.57	75	1.58	1.59	107	1.28	1.27	139	1.26	1.19	171		1.51
12	1.49	1.51	44	1.59	1.54	76	1.59	1.60	108	1.27	1.27	140	1.24	1.21	172	1.57	1.57
13	1.51	1.49	45	1.56	1.48	77	1.63	1.61	109	1.22	1.22	141	1.55	1.47	173	1.59	1.59
14	1.56	1.49	46		1.42	78	1.24	1.24	110	1.30	1.28	142	1.62	1.61	174	1.65	1.60
15	1.53	1.51	47		1.44	79	1.22	1.20	111	1.25	1.22	143	1.61	1.63	175	1.66	1.62
16	1.52	1.55	48		1.41	80	1.13	1.12	112	1.19	1.20	144		1.59	176	1.65	1.66
17	1.60	1.63	49		1.51	81	1.23	1.22	113	1.28	1.25	145		1.61	177	1.62	1.58
18	1.58	1.55	50	1.59	1.62	82	1.12	1.13	114	1.23	1.24	146		1.68	178	1.66	1.65
19	1.60	1.63	51	1.55	1.43	83	1.29	1.26	115	1.26	1.25	147		1.55	179	1.62	1.62
20	1.59	1.63	52	1.51	1.51	84	1.19	1.19	116	1.60	1.65	148	1.53	1.50	180	1.64	1.62
21	1.55	1.60	53	1.15	1.08	85	1.25	1.25	117	1.62	1.63	149	1.56	1.51	181	1.74	1.71
22		1.62	54	1.23	1.13	86	1.20	1.24	118	1.57	1.63	150	1.53	1.54	182	1.64	1.65
23		1.55	55	1.09	1.05	87	1.11	1.18	119		1.51	151	1.61	1.58	183	1.63	1.60
24		1.56	56	1.09	1.02	88	1.50	1.48	120		1.47	152	1.55	1.52	184	1.58	1.52
25		1.46	57	1.09	1.06	89	1.16	1.14	121		1.57	153	1.56	1.51	185	1.66	1.63
26	1.58	1.54	58	1.16	1.09	90	1.18	1.22	122		1.52	154	1.64	1.61	186	1.64	1.51
27	1.58	1.58	59	0.98	0.93	91	1.24	1.29	123	1.61	1.57	155	1.57	1.54	187	1.70	1.67
28	1.59	1.51	60	1.08	0.95	92	1.60	1.61	124	1.68	1.67	156	1.58	1.53	188	1.60	1.60
29	1.24	1.23	61	1.01	0.97	93	1.62	1.62	125	1.62	1.64	157	1.60	1.58	189	1.29	1.21
30	1.26	1.21	62	1.06	0.97	94	1.59	1.57	126	1.43	1.38	158	1.62	1.63	190	1.13	1.10
31	1.23	1.17	63	1.19	1.14	95		1.68	127	1.31	1.27	159	1.63	1.62	191	1.28	1.18
32	1.34	1.29	64	1.02	1.00	96		1.50	128	1.41	1.38	160	1.65	1.62	192	1.23	1.21

Appendix 6. Boiler 1 cladding AISI 304 thickness changes 2023-2024 Pos 4

Tube	2023	2024	Tube	2023	2024	Tube	2023	2024	Tube	2023	2024	Tube	2023	2024	Tube	2023	2024
1	1.51	1.45	33	1.38	1.37	65	1.10	1.11	97	1.64	1.60	129	1.46	1.42	161	1.55	1.57
2	1.47	1.42	34	1.33	1.31	66	1.26	1.26	98	1.63	1.63	130	1.49	1.44	162	1.60	1.62
3	1.42	1.33	35	1.33	1.32	67	1.13	1.15	99	1.60	1.63	131	1.47	1.46	163	1.61	1.57
4	1.45	1.36	36	1.33	1.34	68	1.63	1.59	100	1.64	1.63	132	1.36	1.29	164	1.60	1.56
5	1.27	1.18	37	1.29	1.28	69	1.65	1.62	101	1.58	1.60	133	1.39	1.28	165	1.60	1.58
6	1.39	1.34	38	1.34	1.31	70	1.56	1.55	102	1.26	1.25	134	1.29	1.19	166	1.54	1.58
7	1.41	1.34	39	1.31	1.32	71	1.52	1.47	103	1.26	1.25	135	1.32	1.24	167	1.59	1.59
8	1.47	1.46	40	1.29	1.30	72	1.58	1.51	104	1.36	1.36	136	1.20	1.14	168	1.54	1.54
9	1.41	1.38	41	1.26	1.23	73	1.63	1.58	105	1.32	1.34	137	1.26	1.17	169	1.56	1.58
10	1.51	1.49	42	1.35	1.28	74	1.59	1.54	106	1.26	1.25	138	1.29	1.23	170	1.62	1.63
11	1.62	1.60	43	1.60	1.56	75	1.59	1.57	107	1.36	1.31	139	1.31	1.24	171	1.65	1.70
12	1.48	1.49	44	1.57	1.55	76	1.59	1.57	108	1.38	1.36	140	1.31	1.32	172	1.58	1.62
13	1.53	1.62	45	1.53	1.49	77	1.63	1.64	109	1.39	1.33	141	1.60	1.53	173	1.64	1.64
14	1.58	1.60	46	1.54	1.48	78	1.29	1.30	110	1.34	1.39	142	1.60	1.52	174	1.62	1.66
15	1.54	1.53	47	1.59	1.50	79	1.31	1.28	111	1.36	1.32	143	1.60	1.52	175	1.65	1.61
16	1.55	1.56	48	1.61	1.52	80	1.20	1.24	112	1.26	1.27	144	1.61	1.41	176	1.66	1.64
17	1.64	1.62	49	1.62	1.57	81	1.25	1.24	113	1.35	1.37	145	1.56	1.48	177	1.62	1.60
18	1.51	1.58	50	1.60	1.54	82	1.21	1.21	114	1.30	1.31	146	1.54	1.56	178	1.65	1.69
19	1.64	1.64	51	1.59	1.50	83	1.36	1.36	115	1.27	1.23	147	1.57	1.43	179	1.62	1.60
20	1.59	1.64	52	1.60	1.55	84	1.29	1.20	116	1.66	1.63	148	1.56	1.54	180	1.62	1.65
21	1.62	1.60	53	1.27	1.20	85	1.36	1.30	117	1.65	1.64	149	1.62	1.56	181	1.71	1.74
22	1.72	1.59	54	1.32	1.23	86	1.28	1.29	118	1.63	1.65	150	1.60	1.53	182	1.66	1.65
23	1.57	1.54	55	1.30	1.22	87	1.21	1.19	119	1.65	1.63	151	1.60	1.53	183	1.62	1.66
24	1.60	1.59	56	1.24	1.18	88	1.31	1.28	120	1.67	1.61	152	1.56	1.52	184	1.59	1.57
25	1.49	1.55	57	1.18	1.16	89	1.19	1.19	121	1.61	1.54	153	1.56	1.54	185	1.71	1.65
26	1.60	1.60	58	1.23	1.20	90	1.24	1.19	122	1.63	1.62	154	1.67	1.53	186	1.65	1.59
27	1.59	1.61	59	1.08	1.03	91	1.29	1.28	123	1.64	1.63	155	1.62	1.52	187	1.70	1.65
28	1.63	1.63	60	1.18	1.19	92	1.60	1.60	124	1.68	1.67	156	1.62	1.58	188	1.62	1.60
29	1.34	1.35	61	1.17	1.15	93	1.64	1.62	125	1.61	1.63	157	1.62	1.53	189	1.31	1.28
30	1.32	1.29	62	1.14	1.13	94	1.63	1.57	126	1.54	1.48	158	1.65	1.63	190	1.17	1.17
31	1.27	1.30	63	1.24	1.22	95	1.63	1.64	127	1.39	1.40	159	1.60	1.57	191	1.36	1.28
32	1.39	1.40	64	1.13	1.05	96	1.62	1.57	128	1.52	1.43	160	1.65	1.63	192	1.27	1.27

Appendix 7. Boiler 1 cladding AISI 304 thickness changes 2023-2024 Pos 5

Tube	2023	2024	Tube	2023	2024	Tube	2023	2024	Tube	2023	2024	Tube	2023	2024	Tube	2023	2024
1	1.37	1.40	33	1.46	1.49	65	1.19	1.18	97	1.40	1.43	129	1.43	1.43	161	1.60	1.59
2	1.42	1.43	34	1.33	1.39	66	1.39	1.39	98	1.35	1.35	130	1.43	1.42	162	1.60	1.58
3	1.39	1.39	35	1.39	1.38	67	1.27	1.26	99	1.38	1.37	131	1.42	1.43	163	1.58	1.54
4	1.35	1.24	36	1.41	1.43	68	1.57	1.51	100	1.38	1.38	132	1.32	1.35	164	1.62	1.63
5	1.32	1.26	37	1.43	1.43	69	1.55	1.52	101	1.36	1.44	133	1.36	1.37	165	1.62	1.61
6	1.32	1.32	38	1.37	1.36	70	1.57	1.59	102	1.35	1.38	134	1.38	1.25	166	1.59	1.62
7	1.43	1.37	39	1.37	1.38	71	1.61	1.58	103	1.34	1.35	135	1.29	1.26	167	1.57	1.58
8	1.47	1.45	40	1.26	1.26	72	1.58	1.58	104	1.37	1.37	136	1.27	1.27	168	1.65	1.68
9	1.41	1.42	41	1.33	1.33	73	1.54	1.59	105	1.32	1.34	137	1.30	1.34	169	1.61	1.65
10	1.52	1.52	42	1.42	1.37	74	1.60	1.57	106	1.29	1.31	138	1.28	1.30	170	1.64	1.66
11	1.52	1.52	43	1.27	1.26	75	1.60	1.58	107	1.41	1.43	139	1.37	1.35	171	1.61	1.63
12	1.40	1.41	44	1.30	1.28	76	1.63	1.62	108	1.43	1.43	140	1.45	1.43	172	1.58	1.63
13	1.49	1.50	45	1.31	1.27	77	1.74	1.74	109	1.40	1.43	141	1.61	1.63	173	1.60	1.65
14	1.51	1.55	46	1.40	1.36	78	1.44	1.40	110	1.39	1.42	142	1.63	1.55	174	1.63	1.64
15	1.50	1.47	47	1.38	1.34	79	1.42	1.44	111	1.39	1.38	143	1.62	1.61	175	1.64	1.67
16	1.39	1.43	48	1.32	1.29	80	1.38	1.40	112	1.38	1.39	144	1.63	1.61	176	1.59	1.53
17	1.57	1.55	49	1.35	1.33	81	1.39	1.38	113	1.39	1.39	145	1.60	1.63	177	1.62	1.66
18	1.53	1.52	50	1.33	1.30	82	1.34	1.34	114	1.40	1.38	146	1.61	1.58	178	1.63	1.63
19	1.64	1.65	51	1.34	1.28	83	1.50	1.46	115	1.35	1.37	147	1.65	1.64	179	1.59	1.59
20	1.63	1.66	52	1.32	1.29	84	1.37	1.33	116	1.70	1.74	148	1.63	1.62	180	1.60	1.64
21	1.62	1.63	53	1.33	1.26	85	1.46	1.45	117	1.62	1.62	149	1.61	1.63	181	1.65	1.65
22	1.64	1.67	54	1.36	1.32	86	1.45	1.47	118	1.73	1.75	150	1.61	1.63	182	1.66	1.68
23	1.62	1.66	55	1.34	1.30	87	1.32	1.35	119	1.57	1.63	151	1.64	1.61	183	1.60	1.65
24	1.65	1.63	56	1.34	1.29	88	1.44	1.47	120	1.65	1.69	152	1.62	1.61	184	1.63	1.62
25	1.62	1.62	57	1.24	1.18	89	1.33	1.33	121	1.64	1.64	153	1.59	1.57	185	1.62	1.67
26	1.65	1.62	58	1.29	1.24	90	1.27	1.27	122	1.65	1.65	154	1.59	1.55	186	1.65	1.71
27	1.65	1.62	59	1.20	1.15	91	1.36	1.38	123	1.63	1.66	155	1.60	1.60	187	1.65	1.63
28	1.74	1.79	60	1.36	1.32	92	1.26	1.23	124	1.65	1.66	156	1.61	1.60	188	1.67	1.67
29	1.40	1.40	61	1.27	1.30	93	1.35	1.32	125	1.63	1.64	157	1.62	1.61	189	1.43	1.34
30	1.39	1.40	62	1.30	1.27	94	1.38	1.36	126	1.43	1.42	158	1.60	1.59	190	1.27	1.24
31	1.38	1.38	63	1.30	1.29	95	1.29	1.29	127	1.40	1.38	159	1.61	1.58	191	1.42	1.46
32	1.47	1.48	64	1.32	1.30	96	1.34	1.38	128	1.48	1.47	160	1.64	1.61	192	1.41	1.42

Appendix 8. Boiler 1 cladding AISI 304 thickness changes 2023-2024 Pos 6

Tube	2023	2024	Tube	2023	2024	Tube	2023	2024	Tube	2023	2024	Tube	2023	2024	Tube	2023	2024
1	1.33	1.32	33	1.52	1.62	65	1.73	1.76	97			129	1.43	1.47	161	1.62	1.64
2	1.37	1.37	34	1.58	1.64	66	1.66	1.67	98	1.59	1.59	130	1.54	1.54	162	1.59	1.58
3	1.38	1.42	35	1.60	1.70	67	1.65	1.65	99	1.59	1.61	131	1.45	1.48	163	1.62	1.62
4	1.34	1.30	36	1.63	1.60	68	1.69	1.69	100	1.62	1.62	132	1.51	1.51	164	1.57	1.55
5	1.39	1.37	37	1.56	1.59	69	1.68	1.66	101	1.58	1.60	133	1.46	1.44	165	1.58	1.62
6	1.53	1.51	38	1.54	1.54	70	1.56	1.56	102	1.61	1.63	134	1.35	1.36	166	1.61	1.58
7	1.47	1.44	39	1.48	1.50	71	1.56	1.54	103	1.54	1.53	135	1.39	1.38	167	1.60	1.61
8	1.55	1.49	40	1.62	1.63	72	1.53	1.57	104	1.54	1.53	136	1.29	1.29	168	1.63	1.63
9	1.62	1.60	41	1.57	1.56	73	1.53	1.52	105	1.50	1.49	137	1.43	1.45	169	1.60	1.62
10	1.53	1.57	42	1.64	1.64	74	1.60	1.58	106	1.52	1.43	138	1.32	1.35	170	1.64	1.65
11	1.55	1.55	43	1.50	1.52	75	1.70	1.68	107	1.48	1.47	139	1.39	1.39	171	1.63	1.65
12	1.61	1.61	44	1.57	1.54	76	1.65	1.67	108	1.58	1.61	140	1.46	1.43	172	1.61	1.64
13	1.50	1.44	45	1.48	1.46	77	1.73	1.72	109	1.54	1.52	141	1.60	1.58	173	1.64	1.66
14	1.55	1.52	46	1.61	1.58	78	1.60	1.57	110	1.47	1.50	142	1.58	1.54	174	1.64	1.68
15	1.57	1.53	47	1.56	1.58	79	1.71	1.72	111	1.58	1.55	143	1.65	1.62	175	1.63	1.62
16	1.43	1.39	48	1.63	1.61	80	1.49	1.51	112	1.64	1.59	144	1.64	1.63	176	1.62	1.62
17	1.37	1.35	49	1.63	1.58	81	1.45	1.49	113	1.37	1.38	145	1.61	1.61	177	1.64	1.66
18	1.54	1.49	50	1.63	1.57	82	1.71	1.72	114	1.58	1.57	146	1.62	1.61	178	1.61	1.63
19	1.32	1.37	51	1.62	1.61	83	1.65	1.62	115	1.51	1.52	147	1.61	1.62	179	1.58	1.62
20	1.39	1.39	52	1.55	1.57	84	1.67	1.67	116	1.55	1.59	148	1.58	1.60	180	1.66	1.67
21	1.42	1.43	53	1.44	1.42	85	1.49	1.52	117	1.53	1.56	149	1.62	1.61	181	1.66	1.63
22	1.35	1.36	54	1.43	1.46	86	1.69	1.67	118	1.42	1.42	150	1.59	1.62	182	1.67	1.70
23	1.51	1.50	55	1.50	1.53	87	1.64	1.66	119	1.54	1.57	151	1.59	1.59	183	1.65	1.67
24	1.40	1.39	56	1.54	1.55	88	1.70	1.71	120	1.52	1.53	152	1.58	1.58	184	1.61	1.62
25	1.53	1.51	57	1.55	1.53	89	1.59	1.59	121	1.39	1.38	153	1.62	1.64	185	1.64	1.63
26	1.35	1.36	58	1.48	1.45	90	1.73	1.76	122	1.60	1.58	154	1.58	1.59	186	1.63	1.63
27	1.57	1.57	59	1.76	1.71	91	1.64	1.65	123	1.47	1.46	155	1.62	1.62	187	1.68	1.63
28	1.43	1.46	60	1.64	1.58	92	1.69	1.73	124	1.42	1.42	156	1.61	1.61	188	1.70	1.74
29	1.51	1.54	61	1.62	1.58	93	1.55	1.50	125	1.43	1.42	157	1.58	1.59	189	1.51	1.47
30	1.45	1.43	62	1.47	1.47	94	1.60	1.59	126	1.51	1.50	158	1.63	1.68	190	1.60	1.60
31	1.58	1.54	63	1.54	1.53	95	1.57	1.55	127	1.49	1.49	159	1.59	1.60	191	1.48	1.43
32	1.50	1.49	64	1.65	1.61	96			128	1.51	1.51	160	1.63	1.63	192	1.47	1.42

Appendix 9. Boiler 1 cladding AISI 304 thicknesses only negatives 2023-2024

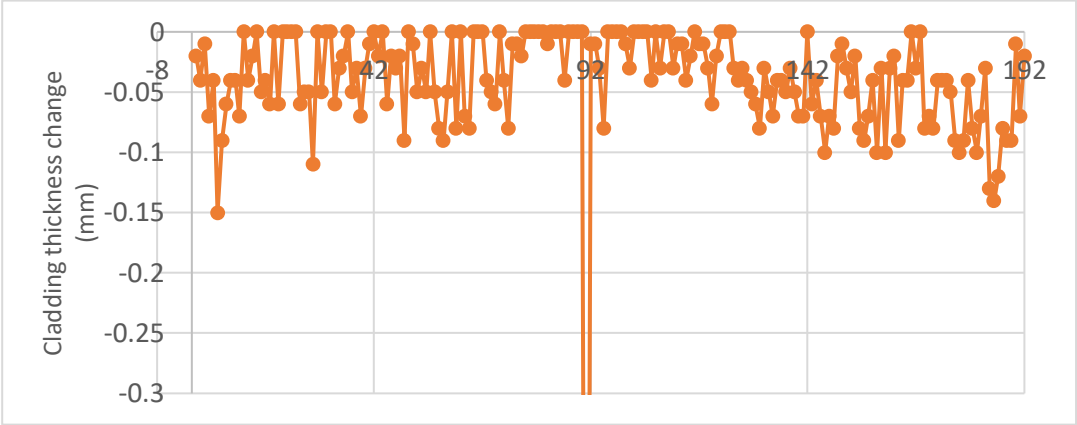

Figure 1. Pos 1.

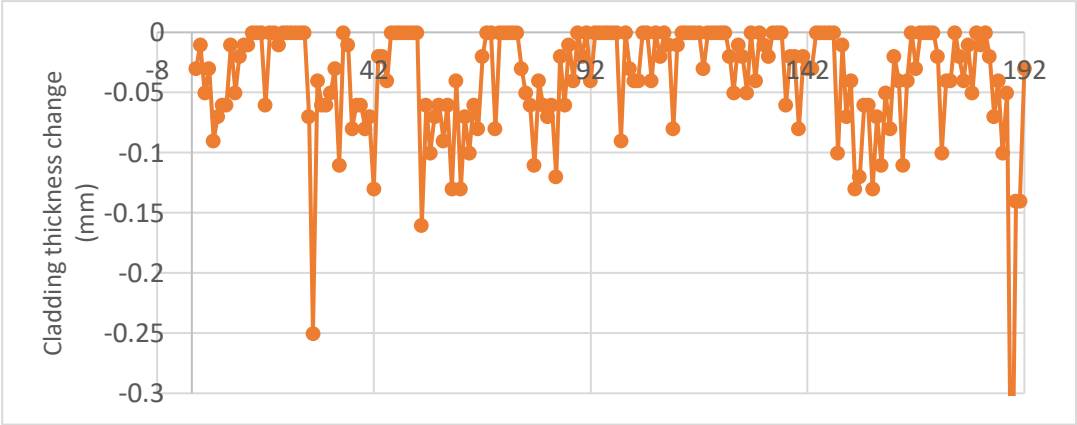

Figure 2. Pos 2.

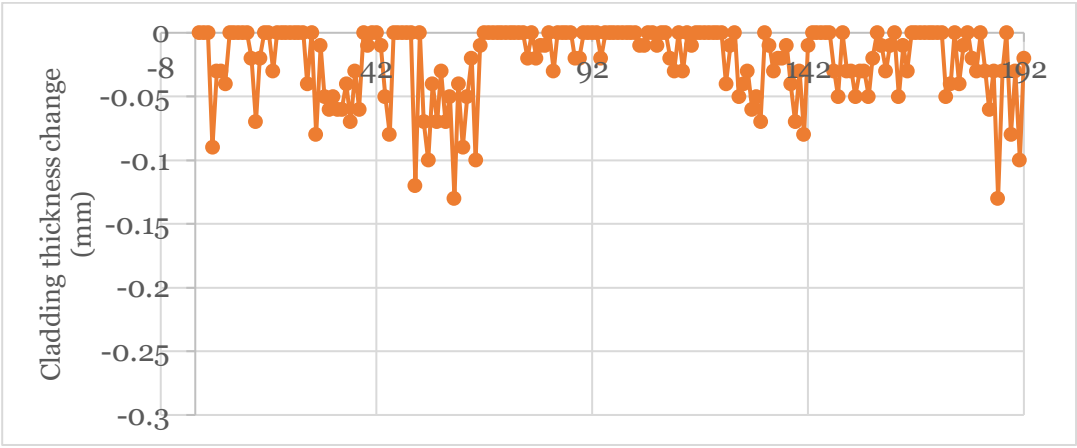

Figure 3. Pos 3.

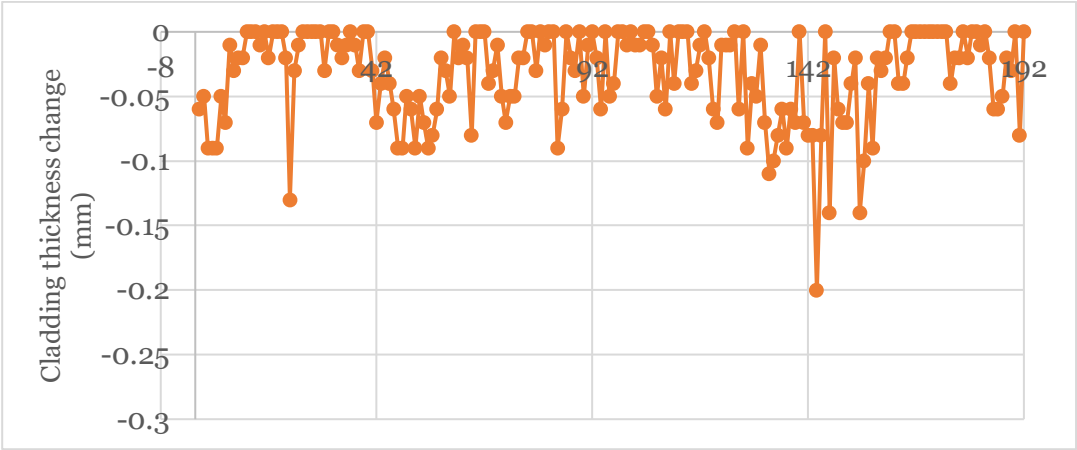

Figure 4. Pos 4.

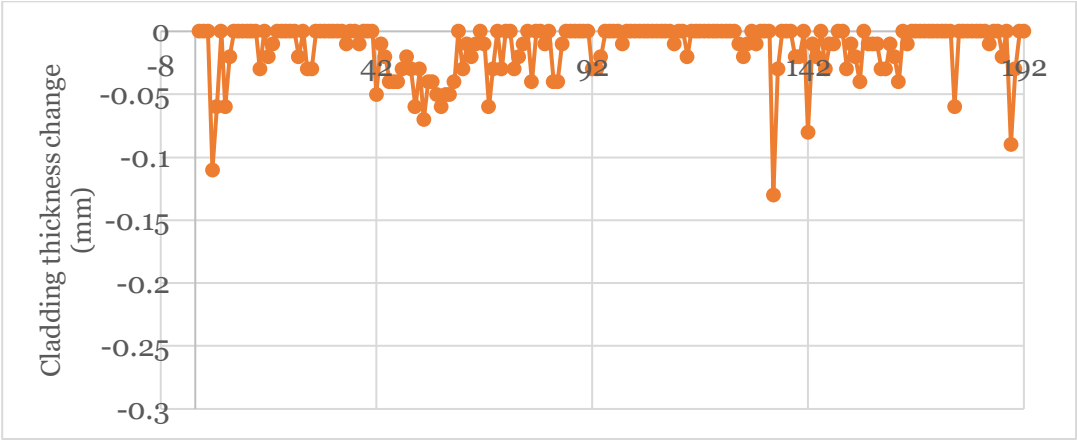

Figure 5. Pos 5.

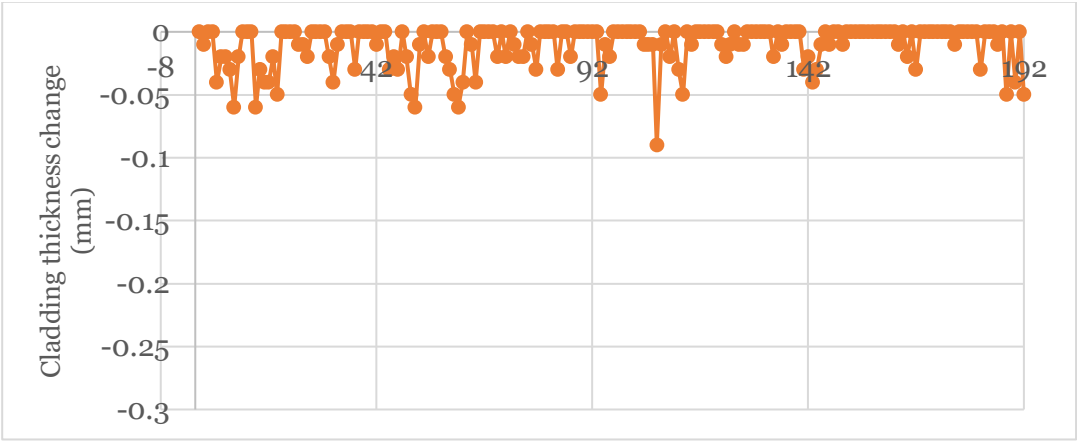

Figure 6. Pos 6.